TECHNISCHE UNIVERSITÄT MÜNCHEN

Chemie Department
Lehrstuhl für Physikalische Chemie I

The design of a ring electrode ion trap with enhanced mass range: Size-dependent oxidation of tantalum clusters

Daniel Neuwirth

Vollständiger Abdruck der von der Fakultät für Chemie der Technischen Universität München zur Erlangung des akademischen Grades eines

Doktors der Naturwissenschaften

genehmigten Dissertation.

Vorsitzender Univ.-Prof. Dr. Sebastian Günther

Prüfer der Dissertation:
1. Univ.-Prof. Dr. Ulrich Kaspar Heiz
2. Univ.-Prof. Dr. Klaus Köhler
3. Univ.-Prof. Dr. Thorsten Bernhardt (Universität Ulm)

Die Dissertation wurde 26.10.2015 bei der Technischen Universität München eingereicht und durch die Fakultät für Chemie am 30.11.2015 angenommen.

Abstract

Gas phase metal clusters are regarded as good model systems for catalysis. The study of their properties can facilitate the development of new catalysts. In the first part of the thesis an experimental setup which enables the study of the reactivity of metal clusters under multi-collision conditions has been designed, implemented and characterized. Metal clusters are produced by a laser vaporization source and size-selected by a quadrupole mass filter, subsequently stored and exposed to a reactive gas in a newly built ring electrode ion trap. Charged clusters in a broad mass range from 200 u to more than 16'000 u can be trapped for up to multiple seconds. The temperature of the trap can be varied between 20 K and 325 K. The special geometry of the trap in combination with a home-built electronics unit allows an efficient ejection of the ions after a set storage time. The very defined extraction procedure enables product characterization by a reflectron time-of-flight mass spectrometer. As all reaction products can be monitored at the same time, this approach facilitates the study of complex reaction networks with many reaction products.

In the second part of the present thesis, the reaction of molecular oxygen with cationic tantalum clusters comprising four to forty atoms is investigated with the afore described experimental setup and the kinetics of this reaction were determined. All cluster sizes reacted readily by the consecutive uptake of oxygen. Interestingly, three size regimes featuring different reaction pathways could be identified.

Larger clusters, composed of thirteen atoms or more, remain intact upon oxidation. The oxygen molecule dissociates and two isolated oxygen atoms are bound to the cluster. After the uptake of a certain number of oxygen molecules, additionally adsorbed oxygen molecules remain intact. The reaction stops after a certain number of oxygen molecules are attached to the cluster.

Smaller clusters with four to eight atoms cannot remain intact upon oxidation. Instead a TaO fragment is ejected from the cluster. The newly formed oxide species fragments as well. The degradation of the cluster proceeds until eventually an oxide is formed that does not degrade.

For clusters with nine to twelve atoms oxidative degradation as well as intact oxidation is possible. The size-dependent reactivity of the tantalum clusters can be attributed to the increased heat capacity of larger clusters due to more degrees of freedom. Hence, larger cluster can be stabilized, whereas smaller clusters relax by the ejection of a TaO fragment. The three reaction regimes are reflected by the oxygen to tantalum ratio of the final reaction products. For smaller clusters a ratio close to the stochiometric value of 2.5 is found, whereas a ratio of approximately 1 is observed for larger clusters. Smaller clusters incorporate oxygen into the cluster structure by the formation of a metal-oxide cluster, for larger clusters only the surface of the cluster is oxidized.

Contents

1 Introduction

Catalysts increase the rate of chemical reactions by lowering the activation energy [1]. Per definition the catalyst itself is not consumed during the reaction [2]. Today catalysts are exploited to facilitate numerous processes like the formation of biofuels [3], the refinement of mineral oil [4] or the reduction of toxic pollutants in exhaust gases [5]. In fact, catalysts are used in 90% of the chemical processes worldwide [6]. Furthermore, catalytic processes play an important role in atmospheric chemistry [7], enzymes catalyze a huge variety of biological processes [8]. Consequently, catalytic reactions have been studied intensively for at least two hundred years [9][10]. The term catalysis was coined in 1835 by Berzelius [11]. Despite the huge interest, trial-and-error strategies were and often still are the only possibility to design new catalysts [12]. A striking example are early efforts for the production of ammonia on a large industrial scale. The osmium catalyst employed by Haber [13] [14] had to be replaced by a more economic alternative. Two years and several tens of thousands attempts were necessary to identify a suitable catalyst based on iron oxide [15] [16]. The development of tailor-made catalysts requires understanding of the involved mechanisms on a molecular level [17]. An example is the systematic search for catalysts promoting the direct conversion of methane into methanol [18].

1.1 Gas phase model systems for catalysis

A particular promising class of heterogeneous catalysts are supported metallic nanoparticles [19]. Consequently, they have been studied extensively during the last decades e.g. [20, 21, 22, 23]. A striking observation was that the catalytic activity often strongly depends on the exact number of atoms comprised in the nanoparticle [24]. In contrast to conventional catalysts which often work at elevated temperatures, nanoparticles catalyze reactions at much lower temperatures [20]. Consequently, they are regarded as environmentally friendly alternatives [16] [25], although their lifetime is still limited [26]. Beside the nanoparticles themselves, also the support has a crucial effect on the catalytic properties [27]. Not only the material of the support itself is important, but other properties as its structure and density of surface defects play a role [16]. In fact, nanoparticles and support often have to be regarded as one catalytic system. One possibility to disentangle nanoparticles from the support is to study the reactivity of free nanoparticles. Especially when carrying a charge, free nanoparticles tend to be a lot more reactive compared to the condensed phase [18] [28]. Nevertheless, gas phase experiments combined with theoretical studies have shown to contribute significantly to the understanding of catalytic processes on a molecular level [28]. One striking observation is the odd-even oscillation of the reactivity of small free gold cluster anions towards oxygen [29], another is the catalytic formation of benzene precursors on free Fe_4^+ clusters [30]. Consequently, gas phase reactions of free metal clusters with molecules have been studied thoroughly during the last decades and continue to be an active field of research. A huge variety of experimental techniques from rather simple collision gas cells [31] up to more complex designs like ion cyclotron mass spectrometers [32] have been employed. In the following a selection of various experimental approaches to study gas phase reactions in a controlled manner is presented. Emphasis is set on the reactions of metal clusters with neutral molecules.

1.2 Experimental techniques to study gas phase reactions

Gas phase reactions can be studied in two different regimes. Under single-collision conditions on average only one collision between the reactants takes place. The available energy is given by the sum of the internal energies of the reactants and the kinetic energy. Reactions with a higher activation energy are suppressed. Under multi-collision additional many collisions with a buffer gas take place. The buffer gas acts as a heat bath and constantly thermalizes reactants as well as reaction intermediates. Hence, multi-collision techniques are closer to the condensed phase than single-collision experiments. The application of ion-trapping techniques enables control of the reaction time. Consequently, this approach allows to elucidate the kinetics of ion-molecule reactions.

1.2.1 Flow tube reactors

One of the first experimental approaches for the study of gas phase reactions were flow tube reactors[33]. In 1929 Smallwood and co-workers used this technique for the investigation of the recombination rate of hydrogen atoms [34]. Figure 1.1 illustrates a typical experimental setup for the study of gas phase kinetics with a flow tube reactor. The subsequent discussion loosely follows the review by Howard [33]. Beside the two reactants, a reactive gas and typically an atom or radical, an inert carrier gas constantly streams into the flow tube. The absolute pressure in the flow tube is in the range of a few mbar. The role of the carrier gas is actually twofold. As the dominant species in the gas mixture it defines for example the temperature of the reactants. For this purpose, the reactor is surrounded by a variable temperature jacket. Hence, the reaction temperature can be controlled and systematically varied, usually between 200 K and 600 K. Specialized setups even allow the study of reactions at 77 K [35] or more than 1000 K [36]. The buffer gas, furthermore, acts as a heat bath as it constantly thermalizes the reaction products. The reactions take place in the so-called reaction zone z, where both reactants are mixed. By shifting the reactant gas inlet, the length of the reaction zone can be varied and consequently rate constants determined.

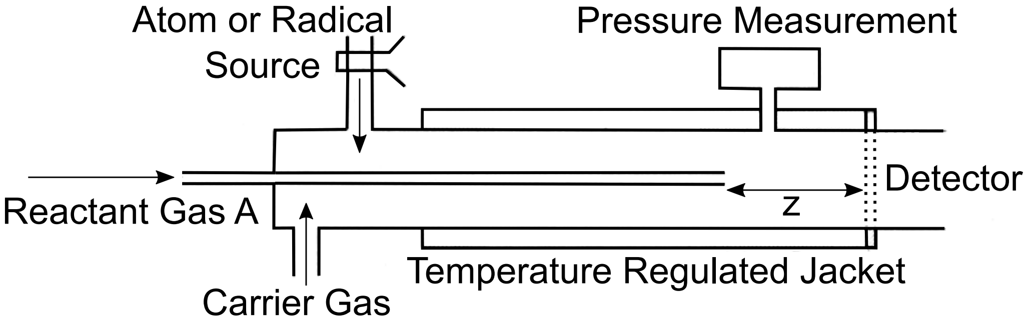

Figure 1.1: *Schematic of a typical flow tube reactor setup to study kinetic of gas phase reactions. Adapted with permission from [33]. Copyright 1979 American Chemical Society.*

One of the first attempts to study the reactivity of free metal clusters was the addition of a flow tube reactor to a laser vaporization cluster source [37] by Geusic et al. [38]. The design and working principle of a state-of-the-art laser vaporization cluster source will be discussed in the experimental section. For this purpose, a 10 cm long flow tube reactor was directly mounted on the cluster source. Typically, the flow tube reactor was filled with a mixture of a reactive gas and a buffer gas (e.g.

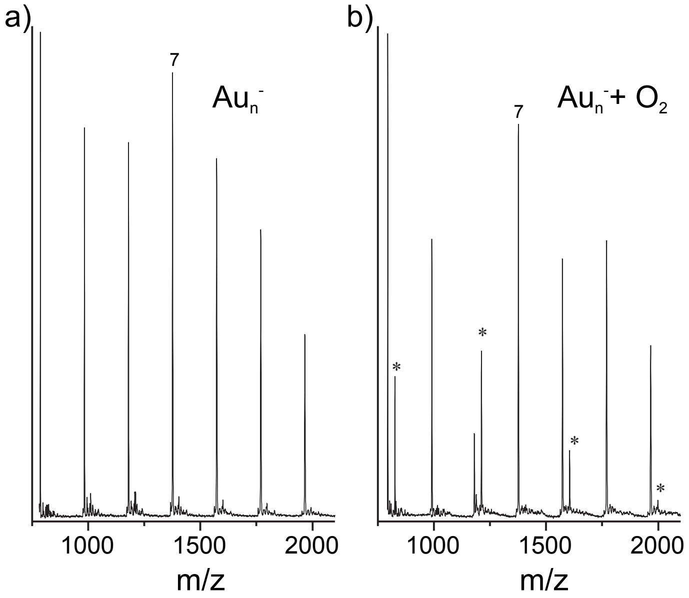

Figure 1.2: *Mass spectra for the reaction of small anionic gold clusters composed of 10 atoms or fewer with oxygen in a fast flow tube reactor. a) Pure helium is introduced into the flow tube reactor, b) 20% oxygen is mixed into the helium buffer gas. Peaks marked with an asterisk correspond to* $Au_NO_2^-$*-species. Adapted with permission from [29]. Copyright 2000 Elsevier.*

helium). As the length of the reaction zone cannot be changed, the concentration of the reactive gas is varied instead [23].

In 2000 Salisbury et al. utilized such a setup to study the reactivity of small anionic gold clusters towards oxygen [29]. Figure 1.2 a) depicts a mass spectrum when pure helium is injected into the flow tube reactor. Beside the pure gold clusters only peaks which corresponds to the reaction with the background gas appear. As soon as oxygen is mixed into the helium the intensity distribution changes drastically. Figure 1.2 b) illustrates a mass spectrum for a mixture of 20% oxygen and 80% helium. While clusters with an odd number of gold atoms are almost unaffected, clusters with an even number are depleted by the reaction with oxygen. The formed reaction product is exclusively $Au_NO_2^-$. The significant odd-even oscillation of the reactivity towards oxygen has been already observed in 1991 by Cox et al. [39]. This phenomenon can be immediately linked to the electron affinity of anionic gold cluster [29] [40]. However, in contrast to nickel clusters no additional adsorption of further oxygen molecules is observed [41]. Later also co-adsorption effects of oxygen and carbon dioxide on anionic gold clusters could be revealed with a similar setup [42].

1.2.2 Collision gas cells

Combinations of flow tube reactors and cluster sources suffer from a significant drawback. Due to the comparably high pressure within the tube, flow tube reactors have to be directly mounted to the cluster source. Otherwise the supersonic cluster beam ejected from the cluster source would be deflected due to scattering. It is often not possible to select a specific cluster size. Interference due to fragmentation of a particular cluster size upon reaction cannot be excluded. Furthermore, nascent charged species cannot be distinguished from neutral species [43]. A possibility to avoid these drawbacks is the utilization of collision cells. In contrast to flow tube reactors, collision cells are significantly shorter [31] and no buffer gas is required. Collision cells are, therefore, filled with the pure reactive gas. The pressure of the reactive gas within the cell is optimized for single-collision-conditions [23]. Each cluster will on average undergo only one collision with the reactive gas. This method enables determination of sticking coefficients [44]. Due to the much lower pressure cluster source and reaction region can be spatially separated. Consequently, unwanted charged species can be deflected or a specific cluster size selected [45]. The lack of buffer gas also prevents thermalization of reactants and reaction products as well. They have to be regarded as isolated systems. Especially, small clusters with a relatively small heat capacity cannot absorb the excess heat of a reaction and thus fragment [23]. The lack of thermalization, furthermore, has a crucial effect on the formed reaction products.

In 2006 He et al. studied the reaction of benzene with neutral niobium clusters in a collision cell. The neutral reaction products have been ionized by 193 nm excimer laser radiation with a low fluence of 50 $\mu J/cm^2$. Figure 1.3 depicts a mass spectrum for a benzene pressure of approximately $0.8 \cdot 10^{-3}$ mbar in the collision cell. Main reaction products for clusters with more than four niobium atoms are completely dehydrogenated species like Nb_nC_x. For smaller clusters partially dehydrogenated species as well as adsorption of intact benzene have been detected. Consecutively adsorbed benzene molecules are completely dehydrogenated as well.

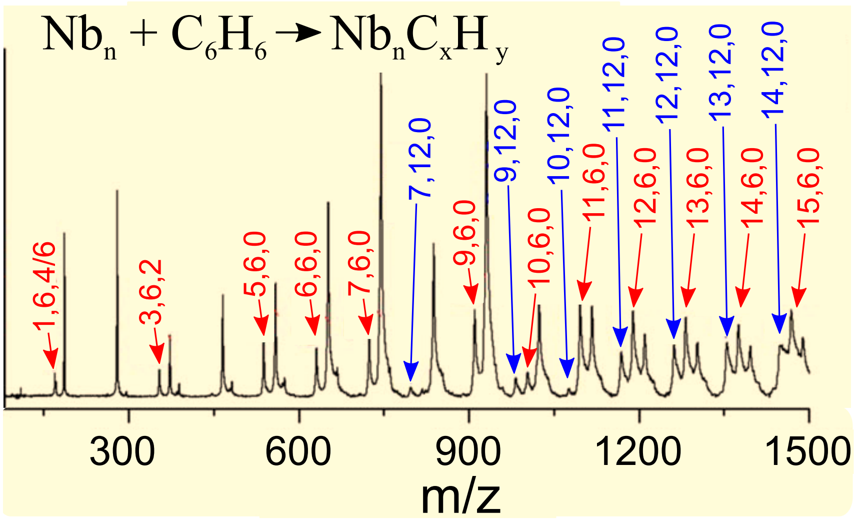

Figure 1.3: *Mass Spectra for the reaction of neutral niobium clusters with benzene. Neutral reaction products are ionized by an 193 nm excimer laser with a fluence of 50 µJ/cm^2 and detected by a time-of-flight mass spectrometer. Peaks labeled in red are formed by a single collision with benzene, whereas peaks color-coded in blue are the result of at least two collisions. Adapted with permission from [43]. Copyright AIP PUBLISHING LLC 2006.*

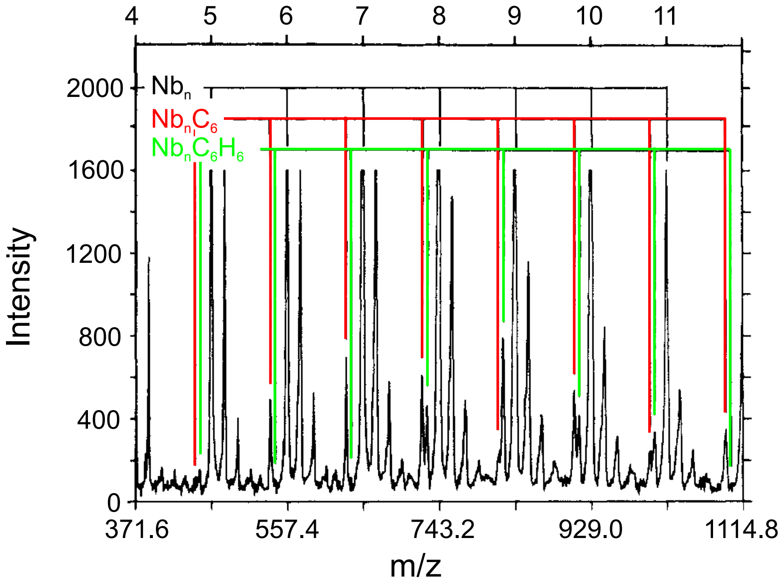

Figure 1.4: *Mass Spectra for the reaction of neutral niobium clusters with benzene. Neutral reaction products are ionized by an 193 nm excimer laser with an energy below 50 µJ/pulse and detected by a time-of-flight mass spectrometer. Adapted with permission from [46]. Copyright 1987 American Chemical Society.*

The same reaction had been studied almost two decades earlier by utilizing a fast flow reactor [46][47][48]. Neutral reaction products were ionized by a 193 nm excimer laser. The energy per pulse was below 50 µJ. A mass spectrum for an absolute pressure of approximately 150 mbar and a benzene concentration of 0.1% to 0.2% is shown in Figure 1.4. Beside the bare unreacted niobium clusters, also Nb_nC_6 and, in contrast to the experiment conducted in the collision cell, $Nb_nC_6H_6$ species are detected. Additional benzene molecules attached to the cluster have been found to remain intact, as well. Adsorption of a benzene molecule, even when it is completely dehydrogenated, seems to passivate the niobium clusters [43]. For the niobium dimer, trimer and tetramer also partial dehydrogenation was observed. The same effect has also been found for cationic niobium clusters. These striking differences in the reactivity of niobium clusters towards benzene can be explained by the presence or the absence of a heat bath [43]. For both experiments niobium clusters form an activated complex $Nb_nC_6H_6^*$ upon reaction with benzene. The excess heat is then released into the cluster. Under single-collision conditions, which prevail in the collision cell setup, the total energy of the cluster remains constant. In order to relax, benzene is dehydrogenated and hydrogen atoms are ejected from the cluster. In a flow tube reactor many collisions with the buffer gas take place. Quick thermalization and stabilization of the formed complex enables a second reaction pathway. Benzene molecules can remain intact upon reaction with the cluster. The simultaneous study of the same reaction system under single- and multi-collision conditions respectively can provide new insights into the reaction mechanism of free metal clusters.

1.2.3 Guided ion beam experiments

In guided ion beam experiments reactions are performed within an ion-guide. Often octupole devices [49] are utilized for this purpose. Typically, the trespassing ion beam is surrounded by a symmetrical arrangement of electrodes. By supplying an RF-potential to the electrodes of the ion-guide, ions are confined in radial direction [50], preventing loss of both, charged reactants as well as formed reaction products [51]. The drawback of this method is its limitation to ion-molecule reactions, whereas flow tube reactors and collision gas cells also enables the study of the reactivity of for example neutral metal clusters. The main advantage of this method is the precise control of the kinetic energy of the charged reactants over four orders of magnitudes, from below 0.1 eV up to roughly 1 keV [52]. Experimentally,

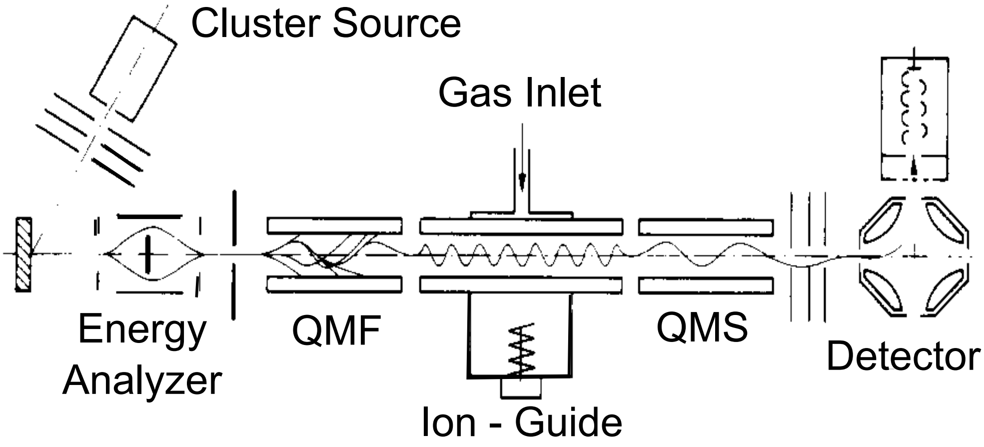

Figure 1.5: *Typical experimental setup to study the reactivity of metal clusters at low kinetic energies with a guided beam experiment. Reactions take place in the Ion-Guide. Adapted with permission from [54]. Copyright 1987 American Chemical Society.*

the kinetic energy of the particles is varied by applying a DC-potential to the ion-guide [53]. Figure 1.5 illustrates a common guided ion beam setup. Charged metal clusters are produced by a sputter cluster source. Only clusters with a certain kinetic energy can trespass the energy analyzer. A quadrupole mass filter (QMS) allows mass-selection of a specific cluster size. Reactions take place within the ion-guide. Product analysis is performed by a second quadrupole mass spectrometer. Wöste and co-workers utilized this setup to study for example the reactivity of cationic nickel clusters towards carbon monoxide [54].

Figure 1.6 depicts a mass spectrum for a low pressure of CO within the reaction zone at the ion-guide for mass-selected Ni_4^+ clusters. The main reaction products are $\mathrm{Ni}_4(\mathrm{CO})_\mathrm{m}^+$ species. Later, the pressure of CO in the drift tube is increased up to $3\cdot 10^{-3}$ mbar. The highest amount of CO molecules adsorbed onto the nickel clusters was found to be 10. This phenomenon can be related to the presence of sixty valence electrons, that provide enhanced stability for tetrahedral clusters [54]. Armentrout and co-workers used a similar setup to measure the cross section of various, mostly endothermic reactions, by systematic variation of the kinetic energy of the charged metal clusters e.g. [49, 53, 55]. This method enables determination of, for example, bond energies not only for pure metal clusters but also for metal oxide species by deliberate fragmentation of the metal clusters. Furthermore, reaction pathways can be identified, electronic structure of the clusters can be revealed and thermochemical data be obtained [52].

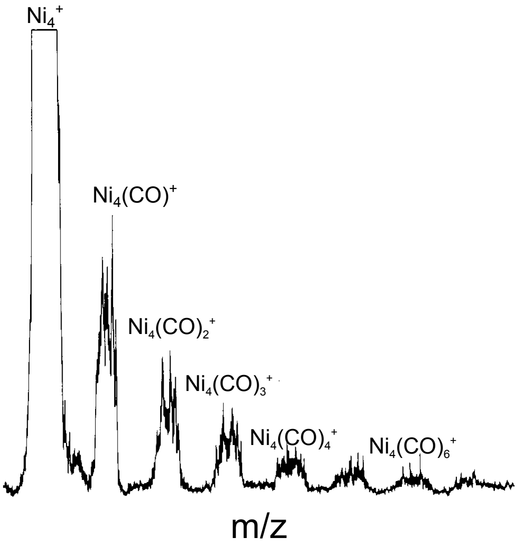

Figure 1.6: *Mass Spectrum for the reaction of* Ni_4^+ *with molecular CO. Main reaction products are* $Ni_4(CO)_m^+$*-species. Adapted with permission from [54]. Copyright 1987 American Chemical Society.*

1.2.4 Fourier transform ion cyclotron resonance

While being powerful tools to study the reactivity of charged metal clusters, none of the presented techniques enables a precise control of the reaction time. Kinetic data is usually obtained by varying the pressure of the reactive gas. Controlling the reaction time requires secure storage of clusters for at least some seconds. In the following, two different concepts, Fourier Transform Ion Cyclotron Resonance Mass Spectrometry (FT-ICR MS) and multipole ion traps will be discussed.

Figure 1.7 illustrates the experimental setup Bondybey and co-workers used to study the reactivity of hydrocarbons with cationic niobium clusters [56]. Clusters are produced in a laser vaporization cluster source. Formed clusters are then transferred into the ion cyclotron resonance (ICR) cell. Source and ICR-cell are separated by four differential pumping stages. This setup allows the pressure in the ICR-cell to be held at $1 \cdot 10^{10}$ mbar while simultaneously operating the cluster source. Ionic metal clusters entering the ICR-cell are accelerated by an RF-pulse. Due to the presence of a magnetic field H (4.7 T), the ions are forced into a circular orbit. The frequency of this movement, the so called cyclotron frequency

$$\omega_c = \frac{zeH}{2\pi m} \tag{1.1}$$

depends upon the mass of the particle. Note, that also the charge ze of the particle

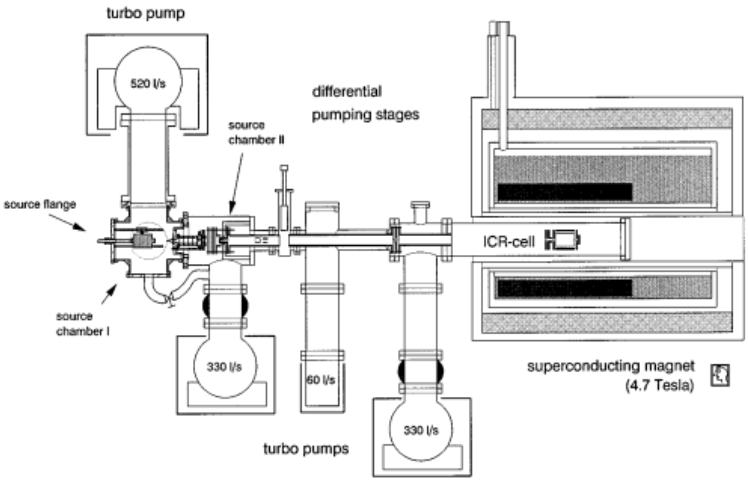

Figure 1.7: *Typical setup to study the reactivity of metal cluster with a Fourier Transform Ion Cyclotron Resonance Mass Spectrometer. Adapted from [56] with permission. Copyright 1995 Elsevier*

influences the frequency. In fact, in all mass spectrometric techniques the mass-to-charge-ratio is measured and not just the actual mass of the particle. Assuming particles carry only one elementary charge it is often, and also for the course of present work, abbreviated to 'mass'. In this respect, by measuring ω_c, the mass of a particle can be determined. Moreover, the application of the FT-ICR MS technique even allows the measurement of the mass of all ions in the ICR-cell simultaneously [57]. A resolution of more than 100'000 has been achieved [58]. It is also possible to restrict the ion movement to a relatively small radius for a long time. Consequently, a ICR-cell can be used as an ion trap as well as a mass spectrometer. As a reactive gas can be additionally introduced into the ICR-cell it is additionally possible to monitor reactions between the ion and the reactive gas in a time resolved manner. The pressure of the reactive gas must be kept low enough in order to not influence the motion of the ion. Consequently FT-ICR studies are limited to single-collision conditions.

Due to long ion storage times of several tens of seconds and an excellent mass resolution, the combination of FT-ICR mass spectrometry with laser vaporization cluster sources is an established technique that has been employed for almost three decades [59]. One of the first studies investigated the dissociation of molecular hydrogen on niobium clusters [60]. Schnabel et al. found one of the first examples

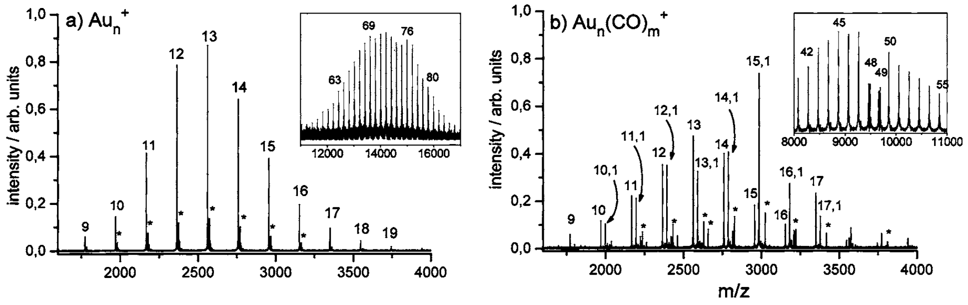

Figure 1.8: *a) Mass Spectrum when no reactive gas is injected into the ICR-cell. Minor peaks marked with an asterisk arise due to impurities present in the ICR-cell. b) Mass spectrum for a carbon monoxide pressure of* $2.3 \cdot 10^{-7}$ *mbar carbon monoxide in the ICR-cell. The storage time is set to 8 s. The inset shows the remarkable reactivity of* $Au_{48,49}^+$ *compared to similar cluster sizes. Adapted with permission from [62]. Copyright 2005 American Chemical Society.*

for a catalytic cycle in the gas phase [30]. Wesendrup and Schwarz observed that tantalum ions can mediate the coupling of carbon dioxide to methane [61]. Later Bondybey and co-workers studied the adsorption of CO on various cationic and anionic metal clusters. In 2005 Neumaier et al. investigated the reaction of carbon monoxide with cationic gold clusters and observed a striking size dependence [62].

Figure 1.8 b) depicts a mass spectrum for $Au_{9\text{-}17}^+$ for a reaction time of 8 s when carbon monoxide is present in the ICR-cell. The partial pressure of CO was $2.3 \cdot 10^{-7}$ mbar. Main reaction products are $Au_n(CO)_m^+$-species. For this particular reaction time species with m=1 are dominant, at longer reaction times peaks correlated to m=2, 3 and 4 become more prominent. Kinetic simulations showed a consecutive adsorption of carbon monoxide molecules. For some cluster sizes like Au_{48}^+ a steady state between m=0 and m=1 is observed. The cationic gold atom, dimer and trimer are found to be inert towards carbon monoxide. Au_4^+ fragmented upon reaction with carbon monoxide. While cationic gold clusters with fewer than 25 atoms are reactive towards carbon monoxide, larger clusters are found to be inert. Strikingly $Au_{48,49}^+$ show some reactivity, while similar cluster sizes do not react with carbon monoxide at all. The measured kinetic data in combination with density functional theory (DFT) allowed to determine the binding strength between cationic gold clusters and carbon monoxide, revealing a quick decrease of the binding strength with increasing cluster size.

1.2.5 Multipole ion traps

Like collision gas cells, FT-ICR MS studies are limited to the single-collision regime. Reactants and intermediate species have to be regarded as isolated systems. The sum of their internal and kinetic energy upon collision define the maximal available energy [16]. As a consequence only reactions with activation energies below the total available energy can proceed. Multipole ion traps allow the storage of ions at much higher pressures of several Pa. Usually a small fraction of a reactive gas is mixed into a buffer gas. Under such conditions many collisions between reactants and the buffer gas take place [63]. Reactants and intermediates are therefore constantly thermalized. Thus, the energy distribution is given by the Boltzmann distribution. Reactants 'in the high energy tail' of the distribution may overcome activation barriers which are prohibited under single-collision conditions. The multi-collision regime is much closer to the condensed phase compared to single-collision conditions. Hence, studies in multipole ion traps are a step towards bridging the pressure gap between surface reactions at ultra high vacuum conditions and technical catalysis at much higher pressures of several bars [16].

Multipole ion traps allow the precise control of reaction time, reaction temperature and concentration of the reactive gas [23]. Beside the investigation of possible reaction pathways, it is also possible to elucidate the kinetics of these reactions. Steady thermalization, furthermore, enables to determine activation energies. Multipole ion traps have been realized in various geometries with the main difference being the quantity and arrangement of electrodes used to confine the motion of ions. Examples for trap geometries are the octupole [50], the 22 pole [50] or the ring electrode trap [64]. A brief discussion on the theoretical considerations and working principles of those traps will be given later on.

Figure 1.9 depicts a scheme of the experimental setup Socaciu et al. used to study the reaction of cationic silver dimers with molecular oxygen [65]. Hot metal clusters are produced by a sputter cluster source [23] and subsequently cooled down to room temperature by collisions with helium within a quadrupole ion-guide (Q_0). A quadrupole mass filter (Q_1) allows the selection of a specific cluster size. Size-selected clusters are then transferred into the octupole ion trap which is filled with a gas mixture. The gas mixture typically consists of a buffer gas and a small fraction of a reactive gas. The trap is operated at a total pressure of 1 Pa. The temperature of the trap can be varied between 20 K and 320 K. Thus, temperature-dependent

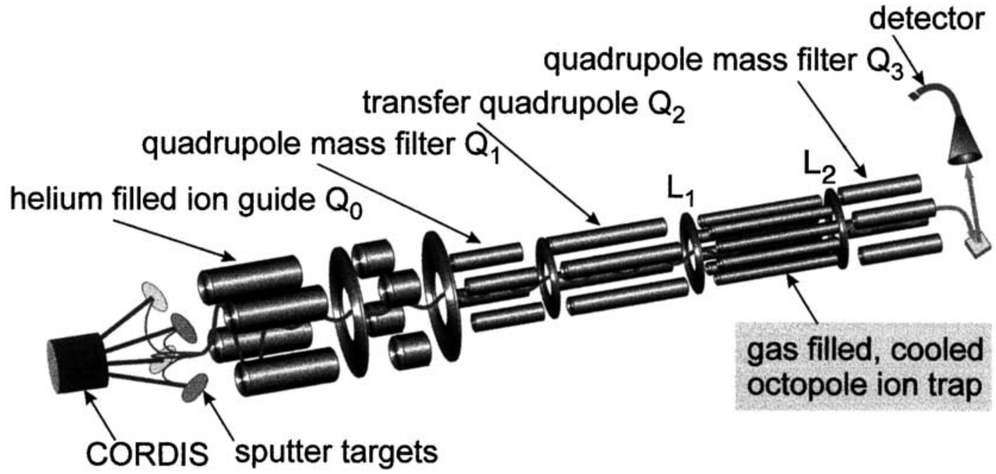

Figure 1.9: *a) Typical experimental setup to study the reactivity of charged metal clusters with a multipole ion trap. Synthesized metal clusters are mass-selected by a quadrupole mass filter, then transferred to the octupole ion trap. After a defined reaction time all charged particles in the trap are ejected into a second quadrupole mass spectrometer. Adapted with permission from [65]. Copyright 2005 American Chemical Society.*

reaction pathways can be revealed. Product analysis is performed by a second quadrupole mass spectrometer (Q_2).

Figure 1.10 depicts mass spectra recorded for reaction temperatures of 50 K, 95 K and 130 K respectively. At 50 K only two reaction products $Ag_2O_2^+$ and $Ag_2O_4^+$ are formed. At a higher reaction temperature of 95 K again two reaction products are detected Ag_2O^+ and $Ag_2O_2^+$. The presence of Ag_2O^+ is a clear indication that oxygen dissociates on the cluster at such temperatures. At an even higher temperature of 130 K also $Ag_2O_3^+$ is formed. Figure 1.10 b) illustrates the concentration of the various reaction products as function of the reaction time for temperatures of 95 K, 110 K and 130 K. By fitting the time dependent concentrations the subsequent reaction scheme could be revealed:

$$Ag_2^+O_2 \underset{k_2}{\overset{k_1}{\rightleftharpoons}} Ag_2O_2^+ \tag{1.2}$$

$$Ag_2O_2^+ \xrightarrow{k_3} Ag_2O^+ \tag{1.3}$$

$$Ag_2O^+O_2 \underset{k_5}{\overset{k_4}{\rightleftharpoons}} Ag_2O_3^+. \tag{1.4}$$

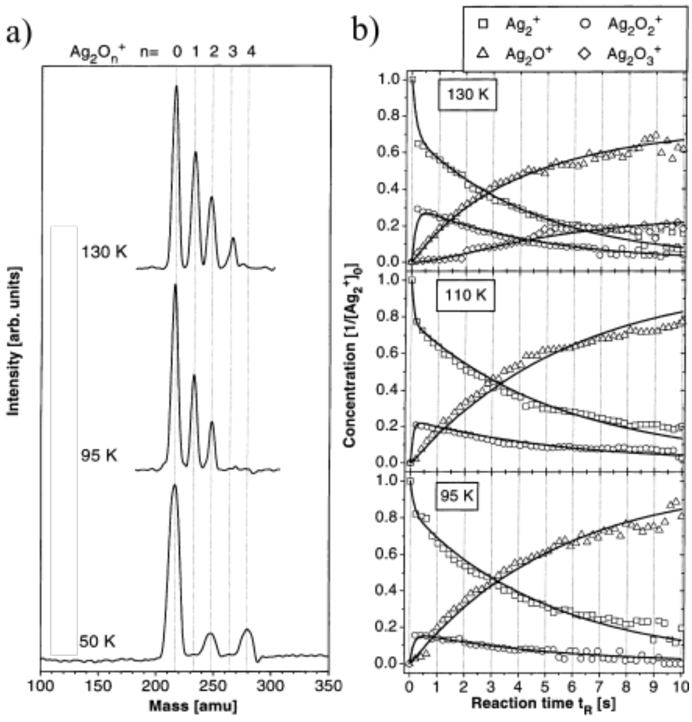

Figure 1.10: *a) Mass spectrum for the reaction of cationic silver dimers with molecular oxygen at temperatures of 50 K, 110 K and 130 K. b) Concentration of detected reaction products. The solid lines represent the result of a kinetic fit. Reprinted with permission from [65]. Copyright 2005 American Chemical Society.*

The solid lines in Figure 1.10 b) represent the result of the kinetic fit. Variation of the reaction temperature enables determination of the activation energies for the reaction of Ag_2^+ to $Ag_2O_2^+$ and Ag_2O^+, respectively. With a similar setup methane activation on cationic gold dimers [66], co-adsorption effects between oxygen and methane on small gold and palladium clusters [67] have been studied. A further striking result was the catalytic formation of formaldehyde and ethylene out of oxygen and methane on the gold dimer. The reaction temperature determines the ratio between the two formed products [68]. These experimental findings clearly demonstrate how control of reaction time and temperature can help to elucidate reaction mechanisms in the gas phase.

1.3 Motivation

The aim of present thesis is the development of an experimental setup that enables the investigation of the reactivity of metal clusters of a broad size range. The reactions shall be studied under well defined multi-collision conditions. Product characterization has to be fast enough to elucidate complex reaction networks. In the multi-collision regime reactants and formed reaction products are constantly thermalized. Compared to single-collision studies, different reaction pathways are possible. The defined reaction temperature enables to overcome initial activation energies, which is impossible at single-collision conditions. Three techniques exist: flow tube reactors, guided beam experiments and multipole ion traps. Uniquely ion traps allow precise variation of the reaction time. Up to now mostly small cluster with typically four atoms or fewer have been studied with such an approach [63]. For supported size-selected clusters, the catalytic properties can depend on the exact number of atoms. For example, gold clusters composed of seven atoms or fewer are inert towards carbon monoxide but Au_8 catalyzes the formation of CO_2. This observation indicates that larger metal clusters may also show unique catalytic properties in the gas phase.

Product characterization for ion-molecule reactions is often done with scanning devices like quadrupole mass spectrometers [63]. The drawback of this method is that only one species can be detected at a time. Especially, for complex reaction networks this results in long measurement times. Product analysis techniques which enable simultaneous detection of all reaction produces are highly favorable. A possible approach is the combination of a multipole ion trap with a time-of-flight mass spectrometer. Equipped with an additional reflector stage, a high sensitivity as well as a high resolution can be achieved with such a setup. Two problems arise, firstly a controlled and efficient ion extraction from the trap into the mass spectrometer is necessary. Therefore, an ion trap with a special geometry, a so-called ring electrode, is utilized. Such an approach has been recently applied for spectroscopic applications [64]. Secondly, the high pressure required to thermalize ions within the trap significantly hampers the resolution of the mass spectrometer. A time-of-flight mass spectrometer specialized for such conditions has to be developed.

The described setup is used to study the reaction of tantalum clusters composed of 4 to 40 atoms with molecular oxygen. Tantalum oxides are utilized, for example, as an anode material in electrochemistry [69]. In the gas phase, tantalum oxides facilitate the activation of methane [70]. C-C insertation has been observed upon the reaction of cation tantalum oxide clusters with benzene [71]. Thus, tantalum oxides are promising candidates for catalytic applications.

While in the first part of this work the new experimental setup is described and characterized in detail (chapter 2 and 3), the subsequent chapters deal with the oxidation of cationic tantalum clusters.

For the latter it is found that all clusters sizes show a quick reaction with oxygen. Reaction pathways depend on the size of the cluster. For clusters with 8 atoms or fewer (chapter 4.3), fragmentation of the metal cluster upon reaction with oxygen occurs. The formed tantalum oxides undergo further fragmentation. Certain species, however, may remain intact upon oxidation. Final, highly oxidized, reaction products have a tantalum to oxygen ratio close to the stochiometric value. This observation indicates that oxygen is incorporated into the cluster structure.

Clusters composed of 13 atoms or more remain intact upon oxidation (chapter 4.4). Tantalum clusters are oxidized by multiple, consecutive reactions with molecular oxygen. For the final species the ratio between tantalum and oxygen atoms is much lower compared to the size regime discussed before. This indicates that oxygen is only bound to the surface of the clusters.

Clusters in the intermediate regime feature both pathways resulting in a complex reaction network (chapter 4.5). The size-dependent reaction pathways can be attributed to the heat capacity of the cluster. Upon oxidation, heat is released into the cluster. The higher heat capacity of larger clusters, due to more degrees of freedom, enables an effective redistribution of the excess heat. Consequently, these species can be stabilized whereas smaller clusters fragment.

2 Experimental setup and methods

In this chapter an overview of the experimental setup is first presented. Major components which have been developed, tuned and implemented during the course of this work are discussed in more detail. Figure 2.1 depicts a scheme of the experimental setup. Metal clusters are produced by a laser vaporization cluster source. This type of cluster source was developed during the early eighties by Smalley and co-workers [37]. Since then, the design of the source has been improved steadily (e.g. [72]). The source used during this work is based on the laser vaporization source described by Heiz et al. [73]. The implemented modifications are described in [74]. A detailed working principle of this type of cluster source can be found for example in [75]. In short, the second harmonic of a pulsed Nd:YAG laser (DPSS Spitlight, Innolas, 100 Hz, 120 mJ/pulse @ 532 nm) is incident upon a rotating metal disc and ejects neutral as well as charged metal atoms [76] into the waiting room. The waiting room is prefilled with a buffer gas, usually helium (Westfalen, 6.0). The buffer gas is pulsed into the waiting room by a home build piezo valve. The valve is triggered some hundreds µs before the laser pulse. Via collisions with the buffer gas, the hot metal atoms thermalize and can agglomerate and eventually form clusters, which comprise from one to more than hundred atoms [77] . Due to the pressure difference between gas inlet of the buffer gas (usually 7 bar) and the nozzle of the source (less than 0.1 mbar), the clusters undergo supersonic expansion. The clusters are cooled to at least 100 K [78] [79]. Cluster temperatures down to 20 K can be achieved by active cooling and special design of the nozzle [75]. The supersonic expansion of the clusters results in a narrow kinetic energy distribution of the formed clusters [73]. The combination of supersonic expansion with the before mentioned laser ablation, which enables evaporation of materials with a high melting point, makes laser vaporization an ideal tool for spectroscopic studies. The high peak outputs compared to continuous sources [75] reduces the time to fill ion traps

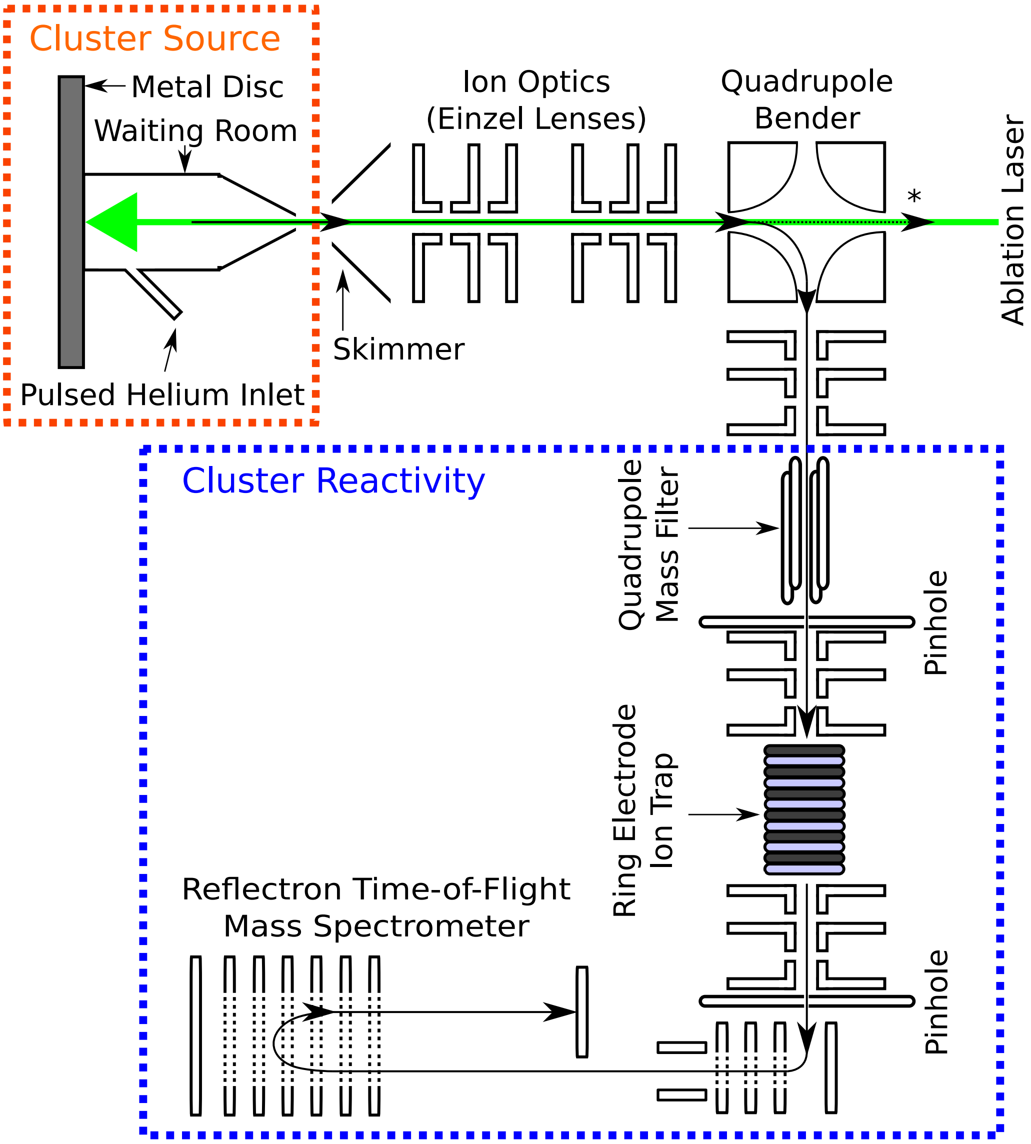

Figure 2.1: *Scheme of the experimental setup. Metal clusters are formed in a laser vaporization cluster source, size-selected by a quadrupole mass filter and stored within a ring electrode trap. Inside the trap they are exposed to a reactive gas which is mixed into a buffer gas. The formed reaction products are characterized by a reflectron time-of-flight mass spectrometer. (* In a second part of the experiment, metal clusters can be investigated spectroscopically.)*

to just a few ms. Hence, laser vaporization sources are also well suited for kinetic studies. A detailed comparison of different cluster sources can be found in [79].

The supersonic cluster (helium) beam is skimmed (skimmer: 5 mm diameter) and is then guided by several Einzel lenses into a quadrupole bender. While uncharged particles, like neutral clusters and the major part of the buffer gas pass without being influenced, charged clusters are bent into a quadrupole mass filter (Extrel 16'000 u). Hence, one specific cluster size can be mass-selected and subsequently stored within a ring electrode ion trap, which has been designed and built during the course of the present work. The trap is filled with a mixture of a buffer gas (helium 6.0, Westfalen) and one or more reactive gases. Two pinholes confine the buffer gas within the ion trap chamber. After a chosen storage time, charged reaction products are ejected into a home built reflectron time-of-flight mass spectrometer and analyzed. Ion detection is performed by a multi channel plate detector (54 mm diameter active areas, Chevron configuration, Scientific Instruments). The measured spectra are visualized by a four channel oscilloscope (Waverunner 44Xi, LeCroy). Besides the reaction time (10 ms - 10 s), also the reaction temperature (35 K - 320 K) and to some degree the pressure (1 Pa - 5 Pa) can be varied, thus the kinetics of the reaction are elucidated in detail. An additionally installed gas reservoir allows for a quick variation of the partial pressure of the reactive gas, providing further insight into the studied reaction.

2.1 Quadrupole mass filter

Laser vaporization cluster sources typically produce a broad distribution of various cluster sizes. The selection of one particular cluster size enables the study of its reaction properties without interference from other cluster sizes. Mass selection is performed by a quadrupole mass filter (QMF). It is operated at a frequency of 440 kHz and an amplitude of up to 6 kV. The diameter of the rods is 3/8 inch. Ions up to 16'000 u can be mass-selected. Operation in ion-guide mode allows ions of wide mass range to traverse the mass filter. A detailed discussion about the so-called RF-only mode can be found in [80].

Figure 2.2 depicts the mounting of the quadrupole. The actual quadrupole rods are surrounded by a stainless steel housing. The housing itself is fixed in position by a clam ring which is bolted to a CF-160 flange. At both ends an Einzel lens is

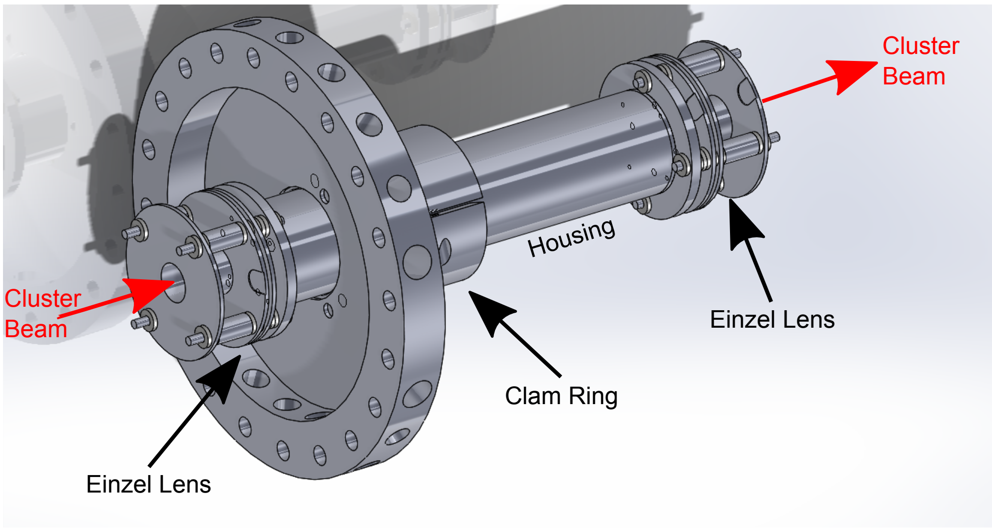

Figure 2.2: *3D CAD drawing of the quadrupole mounting onto a CF-160 flange.*

mounted onto the quadrupole housing. To enhance the transmission characteristics of the quadrupole it is additionally equipped wit pre- and post-filters [81]. The quadrupole chamber is evacuated by a 270 l/s turbo pump (Balzer TPU 270).

Quadrupole mass filters, developed by Paul and co-workers [82] [83] more than sixty years ago, exploit a combination of time-dependent (RF) and time-independent (DC) fields to discriminate between masses. While only a short description of the working principle is given here, a more in depth discussion of the theoretical background is provided by [84]. The subsequent section loosely follows the discussion given in [85].

Figure 2.3 a) depicts a sketch of the physical structure of a quadrupole mass filter. While hyperbolic electrodes are the optimal shape, often cylindrical rods are used as they are easier to manufacture [86]. At each of the four electrodes an electric potential is applied, opposite electrodes are kept at same potential Φ:

$$\Phi_A = +V cos(\omega t) + U, \tag{2.1}$$

$$\Phi_B = -V cos(\omega t) - U. \tag{2.2}$$

where V is the amplitude of the RF-potential, ω the frequency, t the time and U the superposed DC-potential. The potential in between the rods (at position (x, y)) is then given by:

$$\Phi(x, y) = U + V cos(\omega t)\frac{x^2 - y^2}{2r_0^2} \tag{2.3}$$

where $2r_0$ is the distance between two opposite rods. The force $\vec{F}$ experienced by

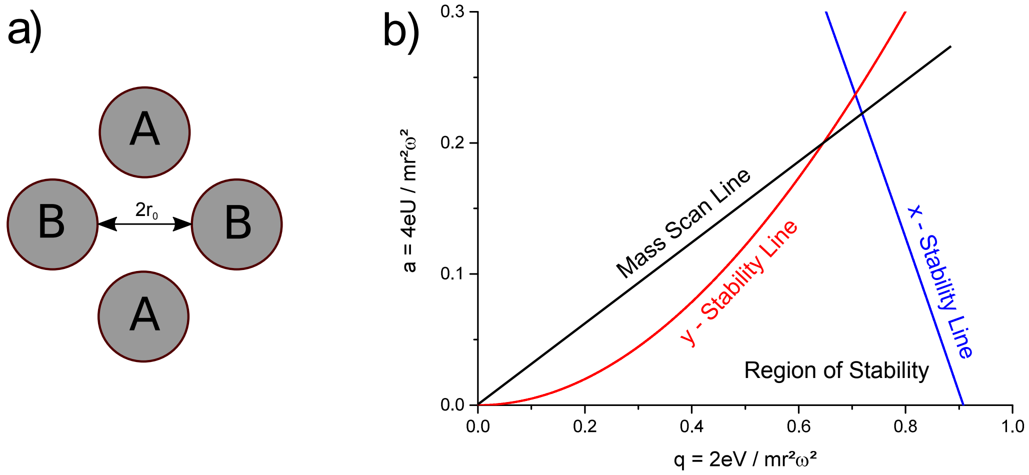

Figure 2.3: *a) Sketch of the electrode arrangement of a quadrupole mass filter with cylindrical rods. Opposite Electrodes (A,B) share the same potential. b) Stability diagram for the quadrupole mass filter. Only ions with masses within the region of stability can trespass the quadrupole. Data taken from [85].*

an ion in the mass filter can be written as:

$$\vec{F}_x = q\vec{E}_x = q\frac{\partial\Phi}{\partial x} = -[U + V cos(\omega t)]\frac{qx}{r_0^2} \tag{2.4}$$

$$\vec{F}_y = q\vec{E}_y = q\frac{\partial\Phi}{\partial y} = +[U + V cos(\omega t)]\frac{qy}{r_0^2}, \tag{2.5}$$

where q is the charge of the particle and m its mass. It should be noted that the particles are not accelerated in the axial direction. Together with Newton's second law

$$\vec{F} = m\vec{a} \tag{2.6}$$

and

$$a = \frac{4eU}{mr^2\omega^2} \tag{2.7}$$

$$q = \frac{2qV}{mr^2\omega^2} \tag{2.8}$$

Equations 2.4 and 2.5 can be transformed to a Mathieu's type of differential equation. For stable solutions the oscillations of the particle stay finite while traversing the quadrupole mass filter, whereas for unstable solutions the oscillations grow without bound, resulting in collisions between particles and the rods or the housing of the quadrupole mass filter. The first stability region for a quadrupole mass filter is depicted in Figure 2.3 as a function of a and q. Note, that many other stable regions exist [87]. Typical commercial quadrupole mass filters, however, only exploit the first one. While U and V can, in principle, be chosen completely freely, they are usually kept at a certain ratio, illustrated in Figure 2.3 b) as the 'Mass Scan Line'. As only ions within the stability region can trespass the mass filter, the increased U and V allows only ions with a higher mass to pass the mass filter. For the present experiment this principle is exploited to mass select a certain cluster size and store it within the ring electrode ion trap.

2.2 Ring electrode ion trap

A key part of the present work has been the construction, implementation and characterization of a ring electrode ion trap. Ions of a broad mass range must be safely stored for several seconds. As the ion trap is coupled with a time-of-flight mass spectrometer also a very controlled ejection of the stored ions is necessary. For this purpose, a special electronics unit has been developed which supplies the necessary RF- and DC-potentials. Consequently, the physical setup of the ring electrode ion trap as well as the home-built electronics unit will be covered during the next sections.

2.2.1 Charged particles in RF-fields

Firstly, the motion of charged particles in an oscillating electric field will be discussed briefly. A more detailed description can be found in [50]. As it is not possible to create a potential minimum in three dimensions with purely electrostatic potentials [88], more complex approaches have to be applied. One possibility is the superposition of an electrostatic field with a static magnetic field [89]. Another possibility is the exploitation of radio-frequency (RF) fields instead of static fields [82]. The movement of a particle with charge (q) in an oscillating electric field is given by the equation of motion:

$$m\ddot{\vec{r}} = qE(t) \tag{2.9}$$

While for quadrupole geometries it is possible to separate the motion in the x-direction from the motion in the y-direction, this is no longer the case for more complex electrode arrangements. Examples are the octupole or the ring electrode ion trap. In such cases, it is possible to apply the so-called adiabatic approximation.

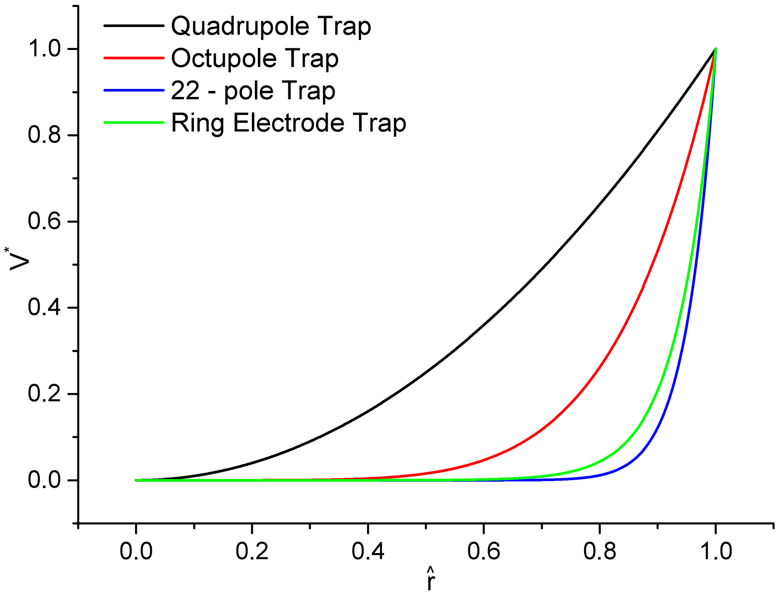

Figure 2.4: *Effective potentials for the quadrupole, octupole, 22-pole and ring electrode ion trap as a function of the reduced distance $\hat{r}$. Data taken from [50].*

The motion of a charged particle within the electric field is described by a slow drift superposed by a fast oscillation [90]. While the oscillation can be neglected if the frequency of the RF-field is high enough, the drift motion is described by the effective potential V^*. For multipole arrangements, like the octupole trap, the effective potential is proportional to:

$$V^* \propto r_0^{n-2}. \tag{2.10}$$

where $\hat{r} = r/r_0$ is the reduced distance to the electrodes and n is the number of electrodes. In the case of the ring electrode ion trap, the effective potential is proportional to:

$$V^* \propto \frac{I_1^2(\hat{r})cos^2(\hat{z}) + I_0^2(\hat{r})sin^2(\hat{z})}{I_0^2(\frac{r_0}{z_0})} \propto e^{f(\hat{r})} \quad [50]\ [91]. \tag{2.11}$$

where $\hat{z}_0$ is the distance between two electrodes and I_0 and I_1 are modified Bessel functions. Figure 2.4 illustrates the effective potentials for quadrupole, octupole, 22-pole and ring electrode traps. The latter two feature a steep increase of the effective potential whereas the effective potential of quadrupole and octupole trap is much shallower. In fact, 22-pole and ring electrode ion trap possess a wide 'field-free' area in the center of the trap minimizing the interaction between the RF-field and stored particles. Hence, these trap geometries are especially suited for the study of ion-molecule reactions due to defined energies of the stored particles.

2.2.2 Design

In the case of linear quadrupole or multipole traps the confining field is evoked by a set of cylindrical rods surrounding the ion storage volume. In contrast to that, the ring electrode ion trap utilizes a stack of annular rings to limit the movement of ions. Compared to other multipole ion traps, the unique geometry of the ring electrode ion trap has two major advantages. Firstly, the stack of metal ring electrodes and insulating sapphire rings creates a gas tight cylinder [64]. The retention time of the gas within the trap increases, resulting in a better thermalization. Secondly, this special geometry enables an efficient ion extraction into the mass spectrometer.

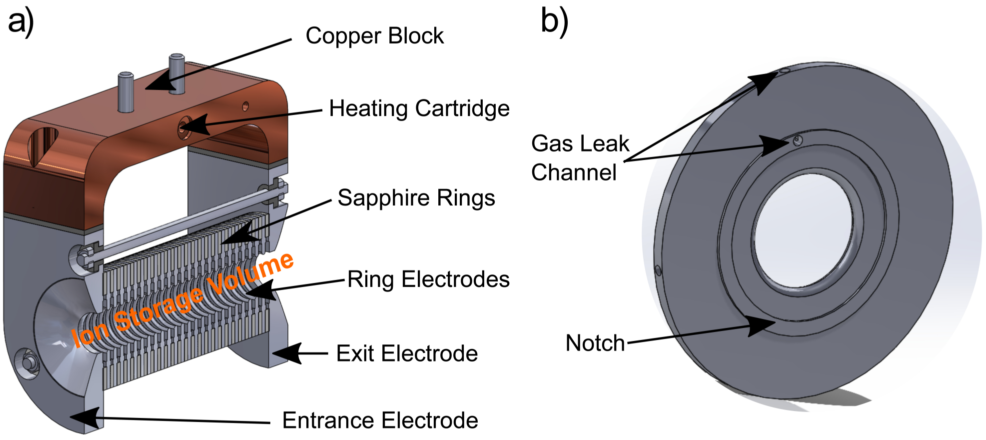

Figure 2.5: *a) 3D-CAD drawing section of the newly built ring electrode ion trap. The entrance and exit electrode confine the ion movement in axial direction, whereas the radial confinement is provided by 24 annular electrodes. The ring electrodes are electrically insulated by sapphire rings, making up a cylindrical ion storage volume. b) 3D CAD drawing of a ring electrode with a gas leak channel.*

Figure 2.5 a) illustrates the implemented ring electrode ion trap. The concept of this type of ion trap was developed by Gerlich and co-workers [50] [92]. The design of the present trap is based on the work performed by the group of Asmis [64], who have improved the before mentioned design by Gerlich. A CAD drawing of a molybdenum ring electrode is provided by Figure 2.5 b). The electrodes are 1.4 mm thick and have an outer diameter of 32 mm and an inner diameter of 11 mm. Molybdenum is chosen due to the minimal variation in the work function for different faces [93] resulting in low patch potentials. Ring electrodes are electrically insulated from each other by annular sapphire disks, which provide a good thermal conductivity across the trap, especially at lower temperatures [94]. The molybdenum and sapphire rings have the same outer diameter as well as the same thickness. The sapphire rings are kept in position by 0.4 mm high notches on the ring electrodes. At either end of the trap, two larger electrodes (outer diameter 54 mm), referred to as the entrance and exit electrodes are placed. While the ring electrodes provide ion confinement in the radial direction, these two electrodes confine ion motion in the axial direction. The potentials applied to the electrodes for ion confinement are discussed in the next Chapter 2.2.3.

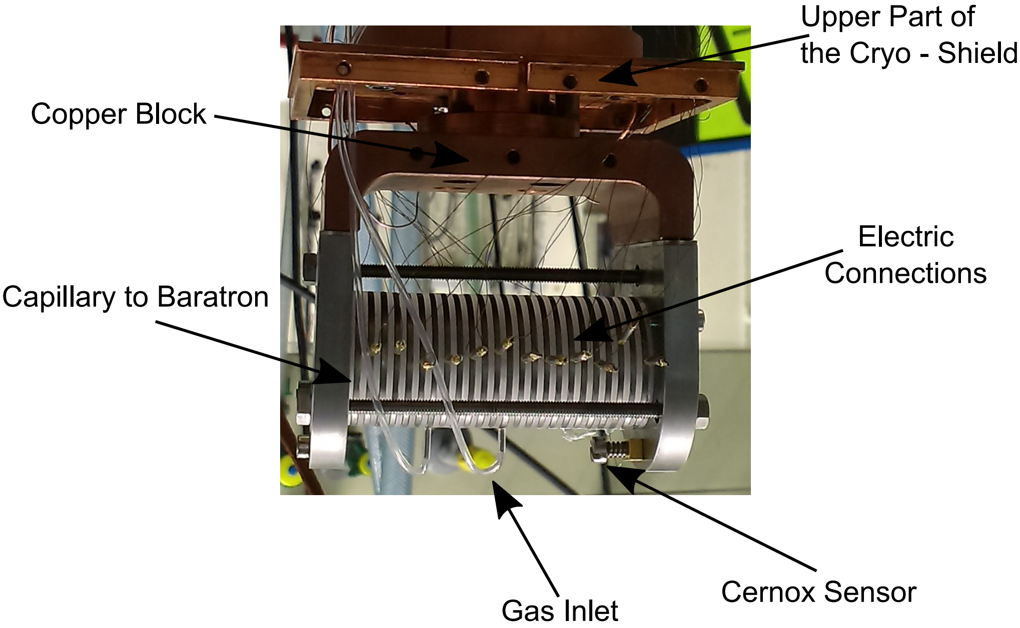

Figure 2.6: *Picture of the ring electrode ion trap , illustrating temperature measurement, gas-inlet, pressure measurement as well as electric connections*

As shown in Figure 2.6, each electrode is individually connected by a 0.14 mm thick manganine wire (Allectra) to a SUB-D feedthrough. These wires are chosen to minimize the heat transfer to the trap assembly at the expanse of comparatively high electric resistance. Entrance and exit electrodes are mounted to a oxygen-free copper block, which itself is bolted to the head of closed cycle helium cryostat (RW2, Leybold). This setup allows cooling of the complete trap down to at least 15 K. To reach such low temperatures it is necessary to shield the trap assembly from the black body radiation of the vacuum chamber, which stays at room temperature. Hence, to prevent heating of the ring electrode ion trap by black body radiation, it is almost completely surrounded by a copper box. The box itself is mounted to the second stage of the cryostat. The second stage has a significantly higher cooling power at a fixed temperatures of 70 K. The temperature of the trap is measured by two CERNOX sensors (Lakeshore).

The positions of both sensors are depicted in Figure 2.6. One is attached to the copper block, while the second is placed at the very bottom of the entrance electrode. A heating cartridge (100 W, Lakeshore) is pressed into the copper block, so that the temperature of the trap can be varied between 15 K and 325 K. The upper limit of the temperature is given by the cryostat which can only be operated below 325 K. The introduction of thermal decoupling at high temperatures between cryostat and trap, by e.g. a sapphire plate or a evacuable gas cell, heating to even higher temperatures would be possible. As a side effect no bake-out of the vacuum chamber where the ring electrode ion trap setup is positioned is possible. Hence, the base pressure within the chamber is roughly $1 \cdot 10^{-8}$ mbar, with water being the major impurity. The chamber is evacuated by a 500 l/s turbo pump (Pfeifer TPU 510) and the pressure is measured by a combination of a pirani and hot cathode gauge (Compact Gauge, Pfeifer).

Buffer gas, as well as, the reactive gases have to be introduced into the trap. For this purpose, a Teflon capillary with an inner diameter of 0.9 mm directly connects the ion storage volume of the trap with a gas reservoir (roughly 33 l) via the gas leak channel shown in Figure 2.5 a). The gas reservoir is positioned outside the vacuum chamber. The flow of the gas mixture into the trap can be adjusted by either a flow controller (MKS, 500 sccm) or a full metal leak valve (VAT). The gas inlet is positioned at the center of the trap. This simple injection method comes at the expense of a inconstant pressure along the axis of the traps [95]. The described setup, however, allows the preparation of gas mixtures containing a buffer gas, usually helium and one or more reactive gases. The role of the injected buffer gas is twofold. Firstly, ions entering the ion storage volume lose a part of their initial kinetic energy due to collisions with the buffer gas and cannot overcome the confining potential created by the electrodes anymore. Secondly, the stored ions get thermalized (again via collisions with the buffer gas) within a few ms for gas pressures in the range of 1 Pa [96]. This method enables an easy variation of the concentration of the reactive gas in the buffer gas. Test measurements showed the feasibility of using reactive gas concentrations down to 10 ppm. At lower concentrations, side reactions with impurities became dominant.

Due to the injected gas, the pressure inside the trap deviates significantly from the pressure within the surrounding chamber. To measure the pressure within the trap, as illustrated in Figure 2.6, a capacitive gauge (Baratron, MKS), is directly connected to the ion storage volume by a thin capillary (0.9 mm inner diameter) via the gas leak channel shown in Figure 2.5 b). The connection to the baratron is located in the center between the gas inlet and the exit electrode. The measured pressure, hence, represents an averaged value of the underlying pressure distribution. The error of the absolute pressure measurement is estimated to be 50% [62]. Furthermore, the measured pressure has to be corrected for thermal transpiration [97]. However, as the flow remains constant, pressure fluctuations with time are estimated to be much smaller (5%).

2.2.3 Electronics

The ring electrode ion trap has to fulfill two major requirements:

a) Secure storage of ions over a large mass range (typically 200 u - 20’000 u) for at least some seconds.

b) Controlled extraction of ions into a reflectron time-of-flight mass spectrometer.

Storage of charged clusters within a ring electrode ion trap requires suitable potentials at the different types of electrodes. At the ring electrodes an RF-potential has to be applied. As shown in Figure 2.7, the phase of the potential has to shift by 180 degrees for adjacent electrodes. In the case of square wave potentials this directly translates to opposite signs of the applied potential. This procedure creates an electric field that confines the ions in the radial direction. The frequency of the RF-potentials has to match the mass of the ions that shall be stored [50]. Traditionally sinusoidal potentials are utilized. As the trap is part of the LC-circuit of the power supply it is technically demanding to build power supplies with variable frequencies [98]. Instead, the amplitude of the RF-potential is increased to equalize the imperfect frequency. Metal clusters may comprise between one and hundred atoms.

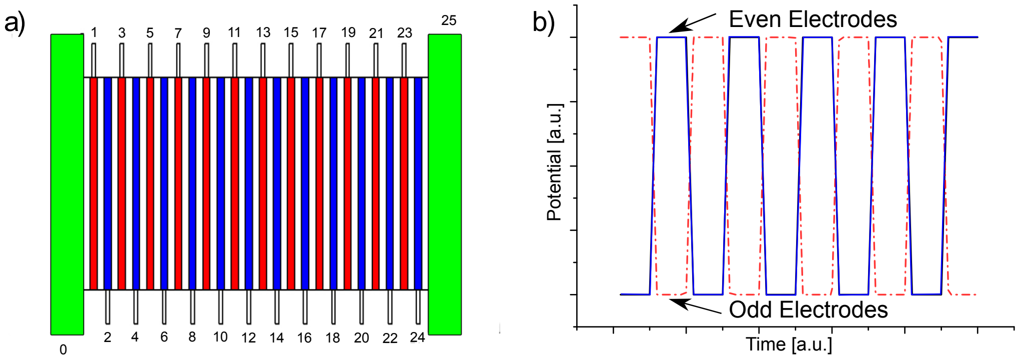

Figure 2.7: *a) Sketch of the ring electrode ion trap with electrode labels. b) Square Wave RF-potentials applied to the ring electrodes during ion storage. Note the phase shift of 180 degrees for adjacent electrodes. Adapted with permission from [105]. Copyright 2015 Elsevier.*

In the case of tantalum this translates to a mass range between roughly 200 u and 20’000 u. To store such a wide mass range, the required amplitudes can easily exceed several kV [50]. A better alternative is to exploit square wave potentials instead, as in this case no LC-circuit is involved. Instead the potential is directly forced onto the electrode. The exploitation of square waves for quadrupole mass filters or ion traps dates back to at least the seventies of the last decade when Richards and co-workers described such a concept for quadrupole mass filters [99]. Recently, renewed interest in this concept has shown up. Ding [100] and Brabeck [101], beside others, studied the digital ion trap, as it is often referred to, theoretically. Bandelow et al. showed the feasibility of this concept experimentally [102]. Major advantages of this methods are the comparably simple design of the power supplies and the variable frequency. Variation of the duty cycle, enables an easy ion injection into the trap [103] [104]. While this concept is well established for quadrupole geometries, it has been applied to a multipole trap for the first time during the course of the present work [105]. The challenges at hand, include the larger amount of electrodes and the higher amplitudes needed to store ions within multipole traps compared to quadrupole devices. To overcome these problems and to exploit the advantageous geometrical properties of the ring electrode ion trap, as the feasibility of a controlled ion extraction combined with the steep potential ideally suited for kinetic studies, an electronics control unit has been developed during the course of this project.

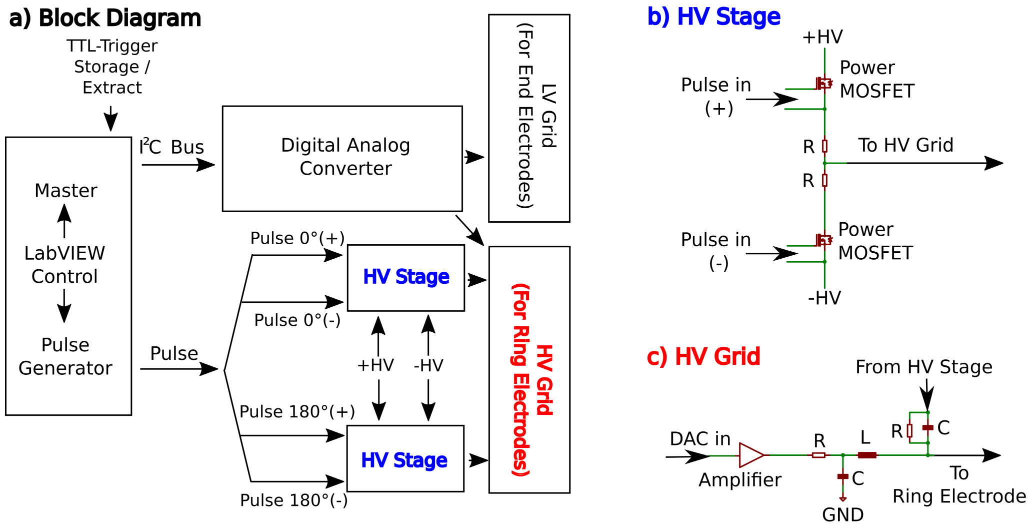

Figure 2.8: *a) Block Diagram of the power supply for the ring electrode ion trap. b) Circuit Diagram of the HV Stage which generates the RF-potentials. c) The HV-Grid allows superposition of the RF-potential with a switchable DC-Offset. Adapted with permission from [105]. Copyright 2015 Elsevier.*

Figure 2.8 a) depicts a block diagram of the newly developed power supply for the ring electrode ion trap. Firstly, a pulse is generated by a LabView (National Instruments) controlled pulse generator. In order to provide the above mentioned 180 degree phase shift for adjacent electrodes, the pulse is divided into two separate pulses. The actual RF-potential is generated by switching periodically between a positive voltage and a negative voltage supplied by two commercial power supplies (TDK-Lambda Genesys, 780 W, 600 V, 1.3 A). The frequency of switching is given by the afore mentioned pulse. As illustrated in Figure 2.8 b) the switching is performed by a half-bridge-circuit, the key component of which is a power-MOSFET. This setup enables generation of square wave functions with peak-to-peak amplitudes of 600 V and frequencies ranging from 100 kHz to 900 kHz. The amplitude as well as frequency are limited by the MOSFET. Consequently, by exchanging this component, the power supply may be tuned for other frequencies. It should be noted that the RF-potential at each ring electrode is supplied by its own HV-Stage, thus the number of electrodes can be varied easily by adding more stages. The electronics configuration described above confines the ion motion in the radial direction, however, the ions can still move freely in the axial direction. To prohibit ion loss, a repelling DC-potential is applied to the entrance and the exit electrodes.

While different types of multipole ion traps are used to study ion-molecule reactions, product characterization is almost exclusively performed by scanning devices like quadrupole mass spectrometers. Such devices have the drawback that only one mass at a time can be detected. Therefore, the intensity of the ion beam injected into the trap has to be highly stable. The implementation of techniques to detect all reaction products at once would be highly favorable. Furthermore, in the case of multiple reaction products or complex reaction networks, the measurement time is strongly reduced. One possibility would be to exploit time-of-flight mass analyzers for product characterization. The combination of quadrupole ion traps with linear time-of-flight mass spectrometers has been studied recently e.g. [106] [107]. The comparatively high pressures required to efficiently thermalize the stored ions prohibit the utilization of so called ion-trap/time-of-flight hybrids [108] [109], as the high gas load significantly hampers the resolution of the mass analyzer. A better solution is to spatially separate the product characterization from the ion-molecule reaction region.

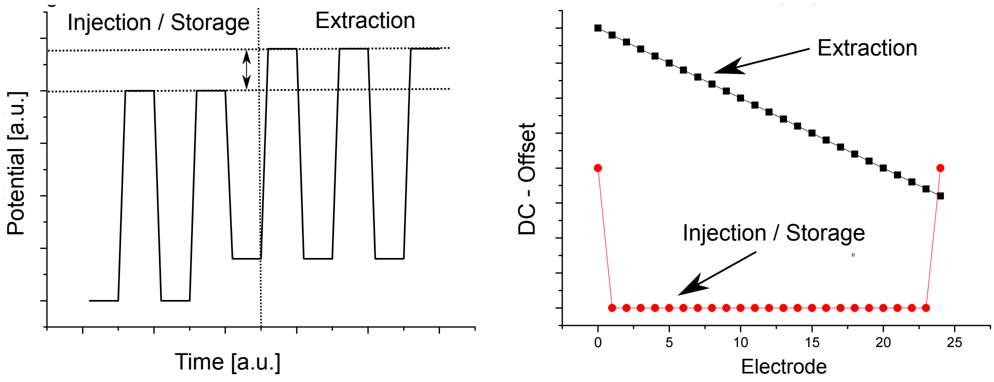

Figure 2.9: *a) and b) DC-offsets superposed to the square wave RF-potentials for injection/storage and extraction mode of the ring electrode ion trap. Adapted with permission from [105]. Copyright 2015 Elsevier.*

In [110] the combination a reflectron time-of-flight mass spectrometer with a ring electrode ion trap is discussed. Operation of the time-of-flight mass spectrometer, however, is severely hampered by uncontrolled ion extraction. In particular, it is not sufficient to apply an extracting potential to both end electrodes. The created fields, especially in the case of the ring electrode trap, do not penetrate deeply into the trap, resulting in slow and uncontrolled ion extraction. The authors further state, that the geometry of the ring electrode ion trap allows the creation of very defined extraction fields. As illustrated by Figure 2.9 a) such fields can be created by superposing a DC-Offset to the RF-potential at the ring electrodes when the ions are to be extracted. For this purpose, specialized power supplies are needed. One possibility for such an experimental setup has been recently described by Heine et al. [111]. While sinusoidal RF-potentials are exploited to store the ions, two adjacent ring electrodes share the same DC-offset. In contrast to that, the newly developed power supply allows an individual offset for each electrode, superposed onto the square wave potentials mentioned above.

As illustrated in Figure 2.8 c), the output of a digital-to-analog converter (DAC) is amplified and then superposed to the RF-potential. The individual DC-potentials can furthermore be used to minimize ion heating due to patch effects [112]. Typical DC-offsets during ion injection/storage and extraction for the electrodes of the ring electrode ion trap are depicted in Figure 2.9 b). To store ions usually no DC-offset is applied to the RF-potentials at the ring electrodes. The entrance and exit electrode are kept at a repelling potential to prevent ion loss in the axial direction. To extract ions from the trap, typically a pseudo-linear electric field is created along the axis of the trap by choosing a 'linear shape' of the DC-offsets.

2.3 Reflectron time-of-flight mass spectrometer

Within time-of-flight mass analyzers, charged particles are accelerated by electric fields onto a particle detector. As all particles experience the same potentials, they have the same energy after acceleration. However, due to different masses, particles have different velocities. Consequently, they are separated in time when they arrive at the detector. Typically multi channel plates are used for particle detection. By measuring the flight times, the mass of the particles can be calculated. The subsequent short scheme of the theoretical background is based on the more in depth discussion found in [113].

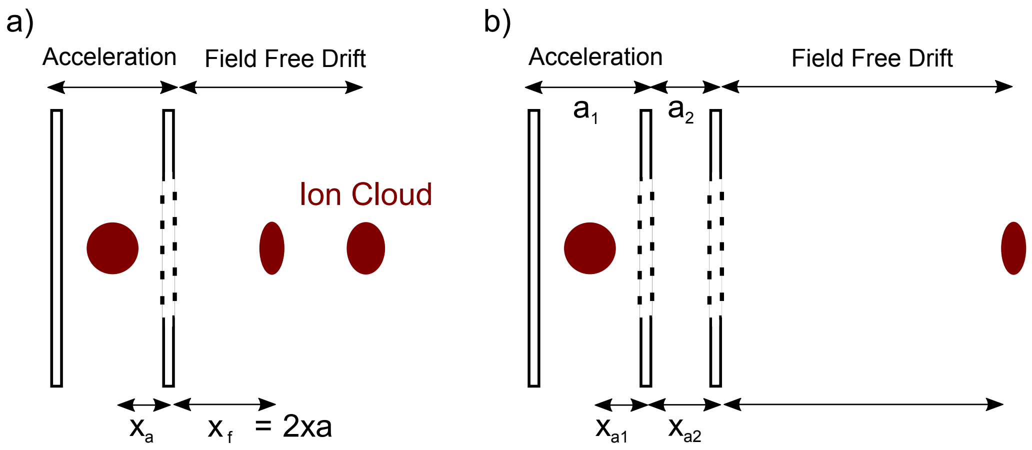

Figure 2.10: *a) Spatial ion distribution as function of the flight time for a one-stage time-of-flight mass spectrometer. b) Spatial distribution in the case of two-stage setup. Adapted with permission from [113]. Copyright 1992 Elsevier.*

Figure 2.10 a) depicts the simplest arrangement for a time-of-flight mass spectrometer. Ions are accelerated by an electric field, created by the potential difference between the two electrodes shown. After leaving the acceleration region, the particle enters the field free drift region and eventually hits the detector. In this case the total flight time t is given by:

$$t = t_A + t_D, \tag{2.12}$$

t_A is the time, the particle spends within the acceleration region, whereas t_D is the time spend within in drift region. t_A is given by the acceleration distance x_A, the mass m, the charge q of the particle as well as by the potential difference between the two electrodes U.

$$t_A = 2x_A\sqrt{\frac{m}{2qU}} \tag{2.13}$$

Furthermore, t_D can be written as

$$t_D = x_D\sqrt{\frac{m}{2qU}}. \tag{2.14}$$

The total flight time t

$$t = (2x_A + x_D)\sqrt{\frac{m}{2qU}} \propto \sqrt{m} \tag{2.15}$$

is proportional to $\sqrt{m}$.

The resolution of time-of-flight mass analyzers is limited by uncertainties in the measured flight time. These are caused by two major contributions:

a) A finite initial spatial distribution and

b) a finite initial velocity distribution.

Both contributions can be minimized in well designed time-of-flight mass spectrometers. Contribution a) is due to the initial finite ion volume. The initial distance to the detector as well as the final kinetic energy of the particles varies. Particles closer to the detector have a lower final energy and, therefore, a lower velocity. However, the flight path of these ions is shorter as well. At one certain flight distance x_{SF}, the position of the so-called space focus, these two effects cancel each other out. Hence, particles with the same mass arrive at x_{SF} at the same time, regardless of their initial starting position. As shown in Figure 2.10 a) x_{SF} equals two times x_a. Typically x_a is in the order of a few cm. Thus, the total flight time is much too short to achieve a good mass resolution. Wiley and McLaren [114] demonstrated that the introduction of an additional acceleration electrode shifts the spacefocus further away from the acceleration electrodes. A scheme of this approach is provided by Figure 2.10 b). Therefore, the flight time increases significantly. By exploiting the so called second order space focus an even higher compression of the initial ion cloud can be achieved [115]. An intrinsic problem of this method is that long flight distances come at the expense of weak fields within the first acceleration region x_{a1}. Consequently, the initial velocity distribution b) has a major impact on the resolution [113].

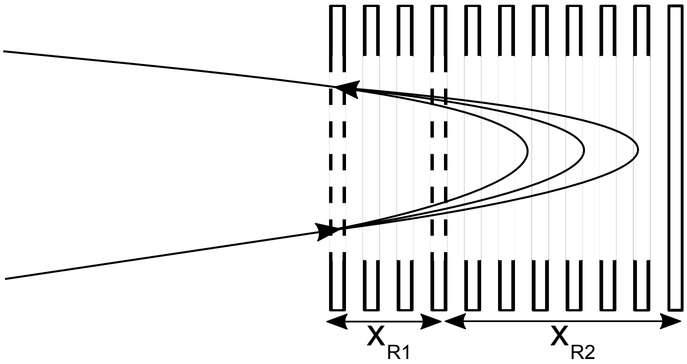

Figure 2.11: *Scheme of two-stage reflectron. Ions with higher kinetic energy penetrate further into the reflection field x_{R2}. The acceleration/deceleration region x_{R1} is used to set the second order spacefocus of the reflectron onto the detector. Adapted with permission from [113]. Copyright 1992 Elsevier.*

A different approach was proposed by Mamyrin in 1973 [116]. The difference in the kinetic energy of the ions, caused by contribution a) and b) is corrected by a so-called ion mirror or reflectron. Figure 2.11 depicts a sketch of a two-stage reflectron. Charged particles entering the reflectron are decelerated by the electric field in x_{R1} and reflected by the field in x_{R2}. Ions with a higher kinetic energy penetrate deeper into the 'reflection' field x_{R2}. Compared to ions with a lower kinetic energy, the flight path of ions with a higher kinetic energy is increased. Thus, it is possible to mirror the space focus of a Wiley-McLaren type time-of-flight mass spectrometer onto the detector. This method enables an increase of the flight time without affecting the arrival time distribution. While single-stage reflectrons only allow for first order focusing, two-stage reflectrons with a deceleration/acceleration region x_{R1}, can exploit the second order space focus [117].

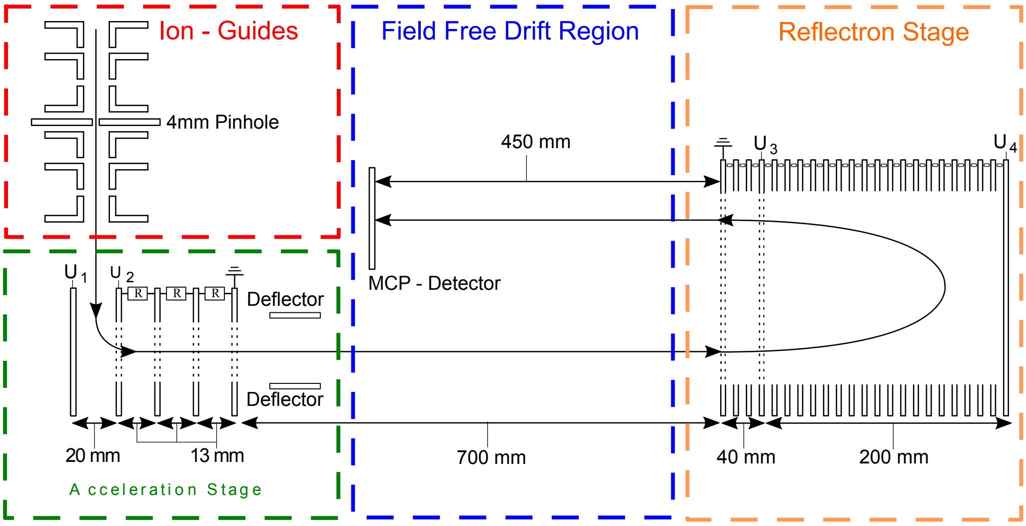

Figure 2.12: *Scheme of the reflectron time-of-flight mass spectrometer, with its four major parts: ion-guides, Wiley-McLaren acceleration stage, field free drift region and the reflectron stage.*

Figure 2.12 illustrates the reflectron time-of-flight mass spectrometer utilized for product characterization during the course of the present work. Ions stored within the ring electrode ion trap are ejected from the trap towards the acceleration stage of the mass spectrometer. As stated in Chapter 2.2.2, for an efficient cooling of the stored ions a comparably high pressure of a few Pa is necessary within the trap. The pressure within the ion trap chamber is measured to be more than 10^{-4} mbar and is more than 10^{-5} mbar at the reflectron stage. Such a high pressure would significantly hamper the operation of the quadrupole mass filter as well as the time-of-flight mass spectrometer. To confine the buffer gas in the ion trap chamber two pinholes between the ring electrode ion trap and reflectron time-of-flight mass spectrometer as well as

QMF-chamber, respectively, are installed. Each has a length of 20 mm. The inner diameter is 7 mm for the pinhole to the QMF-chamber, whereas the pinhole to the reflectron-chamber has a significantly smaller diameter of 4 mm. With the addition of these two pinholes a pressure of $5 \cdot 10^{-7}$ mbar within the reflectron chamber has been achieved during operation of the ring electrode trap. The reflectron chamber is evacuated by two turbo pumps (TPU 510, Pfeiffer 500 l/s, TMU 270 and Balzer 270 l/s).

Moreover, to achieve a good mass resolution a well shaped primary ion beam entering the accelerations stage is required. Due to the narrow diameter of the pinhole only ions with relatively straight trajectories can enter the acceleration stage. The beam shape can be further improved by the two Einzel lenses installed between the ring electrode ion trap and mass spectrometer. The acceleration stage is constructed analogously to a Wiley-McLaren time-of-flight mass spectrometer with two linear electric fields. The first field is created by the potential difference between U_1 and U_2 (20 mm separation), the second field by the potential difference between U_2 and ground (39 mm separation). To ensure straight field lines over such a long distance, two auxiliary electrodes are installed between U_2 and ground. The electrodes are electrically connected by an series of resistors of 100 kΩ.

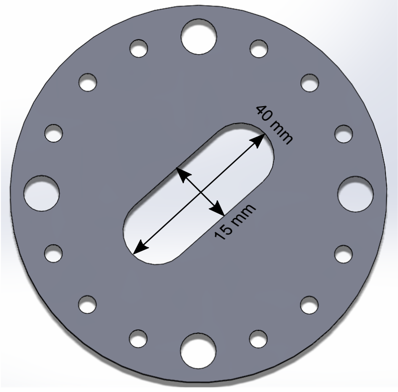

Figure 2.13: *3D-CAD model of an electrode within the acceleration stage. Asymmetric slits are utilized to ensure a high transmission while keeping the field lines straight.*

A 3D-CAD drawing of one of the acceleration electrodes is illustrated by Figure 2.13. The outer diameter is 80 mm and the slit for ion extraction is 40 mm long and 15 mm broad. The long side of the slit is aligned parallel to the primary direction of ion motion due to the extraction from the ion trap. This geometry ensures maximum transmission while the field lines are kept as straight as possible. High transmission copper meshes (90%, Precision Eforming) are spanned across the slits further improve the shape of the field. Deflectors positioned at the end of the acceleration stage can be set at a variable potential to correct for the initial velocity perpendicular to the acceleration direction. As nascent ions are investigated, the acceleration stage has to be operated in pulsed mode. To supply potentials U_1 and U_2 a combination of two fast switching high voltage pulsing units (6 kV, Behlke) and two high voltage power supplies (6.5 kV, FuG) is utilized.

After leaving the acceleration stage, the ions enter the first field free drift region, which is approximately 700 mm long. To reflect the ions, a two stage reflectron is used. The first field, due to the potential difference between ground and U_3, has a length of about 40 mm, whereas the second one is 200 mm long. The different field regions are separated from each other by meshes. As the ion beam has to pass each mesh twice, even when high transmission meshes are employed significant ion loss occurs. A method to prevent such ion loss is to implement a reflectron without any meshes at the expanse of more complicated electrode arrangements [118]. For the present work annular electrodes with an inner diameter of 120 mm are implemented. The distance between two electrodes is roughly 10 mm and stays constant for the whole reflectron stage. In contrast to the acceleration stage no pulsing of the potentials is required. The time-independent potentials U_3 and U_4 are supplied by two high voltage power supplies (6.5 kV, FuG). After leaving the reflectron stage, the ions traverse the field free drift region a second time. After a flight distance of approximately 450 mm they eventually hit the detector. A resolution of more than 3'000 (FWHM) could be achieved with the described reflectron time-of-flight mass spectrometer during operation of the ring electrode ion trap.

2.4 Control of the experiment

A crucial part of the experiment is the synchronization of the ablation laser with the cluster source, the ring electrode ion trap and the time-of-flight mass spectrometer. Three coupled digital delay generators (DG645, Stanford Research Systems) are used to supply the trigger pulses which control the individual parts of the experiment. Figure 2.14 illustrates the operational scheme of a measurement cycle. Table 2.1 provides typical values for the various timings. Time zero, t_0, of each measurement cycle is defined by the ablation laser trigger pulse, t_L. As stated previously at the time the laser hits the metal target disc, the waiting room has to be already prefilled

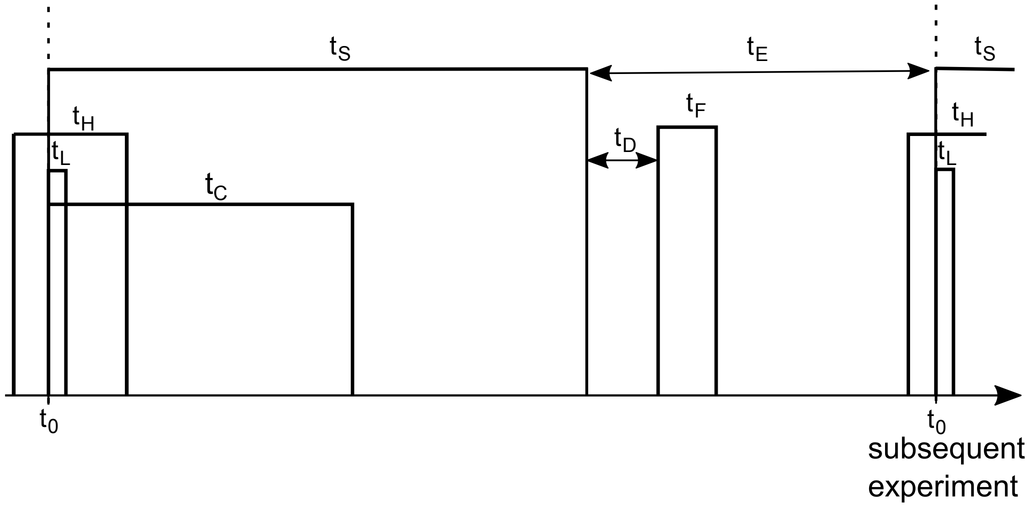

Figure 2.14: *Operating schedule of the various trigger pulses used to control and synchronize the ablation laser, cluster source, ring electrode ion trap and reflectron time-of-flight mass spectrometer.* t_H*: trigger pulse for piezo valve,* t_L*: trigger pulse for ablation laser,* t_C*: pulsing of the bender electrodes,* t_S*: storage mode,* t_E*: extraction mode and* t_D*: delay between extraction and pulsing of the accleration electrodes of the mass spectrometer. Note that the storage time can be longer than the time between two experiments.*

Table 2.1: *Typical values of the trigger pulses as well es their time dependencies. Values are adjusted in order to maximize the intensity of the measured time-of-flight spectra.*

Piezo Valve Trigger Pulse	t_H	300 μs
Laser Trigger Pulse	t_L	10 ns
Ion Collection Time	t_C	5 ms
Ion Storage Time	t_S	5 ms – 10 s
Ion Extraction Time	t_E	2 ms
Time-of-Flight Delay	t_D	400 μs
Acceleration Plates On	t_F	20 μs

with helium. The piezo valve controlling the helium pulse is triggered roughly 200 µs earlier. Typically, the piezo valve stays open for several hundreds of µs, depending on the metal and desired cluster size. Clusters arrive at the ring electrode ion trap approximately 1 to 3 ms after the laser pulse. The electrodes of the quadrupole bender are kept at a tunable potential for at least 5 ms (t_C), to ensure that all clusters are bend around and can reach the ion trap. After that time span, the electrodes of the bender are switched off to prevent any clusters from entering the trap. This procedure is necessary as the repetition rate of laser is fixed at 100 Hz. Thus metal clusters are produced every 10 ms. Storage times typically are much longer than 10 ms. A static potential at the bender would result in the accumulation of clusters in the trap produced by multiple pulses of the ablation laser. To achieve a well-defined storage/reaction time, the newly formed clusters may not enter the trap. This approach, however, also enables accumulation of clusters within the trap from several laser pulses by increasing t_C.

After the set storage/reaction time, t_S, the ion trap electronics switch from storage to extraction mode, ejecting the stored clusters from the trap into the reflectron time-of-flight mass spectrometer. The trap is kept in extraction mode until the next laser pulse, to ensure that all of the ions have left the storage volume. Metal clusters typically need several hundreds of µs to travel from the ring electrode ion trap to the acceleration stage of the reflectron time-of-flight mass spectrometer. Consequently, the acceleration electrodes are switched on for t_F with a certain delay t_D. At the same time also the oscilloscope, used to visualize the measured mass spectra, is triggered. The following measurement cycle starts with the next pulse of the ablation laser. Stored mass spectra typically represent the average of 100 measurement cycles. Concentrations of the various reaction products and educts are calculated from the normalized intensities of the measured mass spectra. Through systematic variation of the reaction time, kinetic data can be obtained.

2.5 Data processing and fit of kinetic data

Due to the large amount of recorded data it is necessary to automatize the required data processing. Therefore, a program package has been developed during the course of the project. As a programming language Python 3.4 was chosen (www.python.org, Python Software Foundation). Major steps of the data treatment process are illustrated in Figure 2.15.

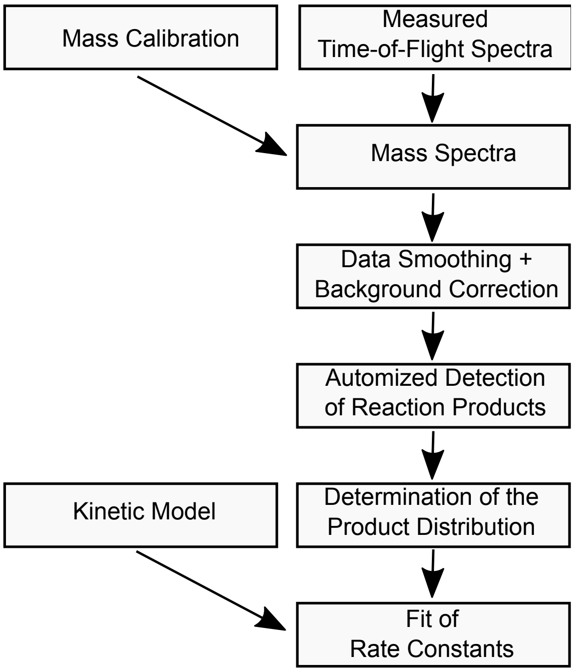

Figure 2.15: *Major steps of the written python program package for an automatized processing of the measurement data.*

As described afore, product characterization is performed by time-of-flight mass spectrometry. In a first step, the recorded 'time-scaled' spectra have to be converted to mass spectra. For this purpose, the quadrupole mass filter is set to ion-guide mode, transmitting a wide size range of clusters. As the masses of the bare metal clusters are known, the correlation between the mass and the flight-time of a particle is obtained. The settings of the ion-guides between the ring electrode ion trap and reflectron time-of-flight mass spectrometer may have an effect on the flight time. Thus, the described mass calibration has to be performed for each measurement series, separately. The obtained mass spectra are routinely background corrected and smoothed by a Savitzky-Golay-Filter [119] to facilitate the subsequent peak detection algorithm. Afterwards the program package relates the detected peaks to possible reaction products. The distribution of the detected reactants and products is determined by normalizing the measured intensities of the correlated peaks. For each reaction time a separate mass spectrum is recorded. By applying this procedure to all mass spectra, the evolution in time of the concentration of all reaction product is known. This builds the foundation for later kinetic evaluation.

During operation, the ring electrode ion trap is filled with charged metal clusters M_n^+ and, in the simplest case, a reactive gas R. Assuming a simple association reaction

$$M_n^+ + R \xrightarrow{k_{as}} M_nR^+ \tag{2.16}$$

the concentration of the reaction product $[M_nR^+]$ depends on the reaction rate k_{as} as well as on the concentration of $[M_n^+]$ and $[R]$. Therefore the reaction is of second-order [120]. As the concentration of the reactive gas can be regarded as constant, the association reaction is of pseudo-first order. The decay of $[M_n^+]$ is given by:

$$-\frac{d[M_n^+]}{dt} = k_{as}[M_n^+] \tag{2.17}$$

and

$$\frac{[M_n^+]}{[M_n^+]_0} = e^{-k_{as}t}. \tag{2.18}$$

For more complicated reaction schemes like several consecutive association step or parallel reactions, analytic solutions are hard to acquire [1]. In a first step the reaction system is transformed to a set of elementary reactions, resulting in a system of coupled differential equations. The differential equations are solved numerically by an algorithm based on LSODE [121]. In a second step the reaction rates k of the elementary steps have to be fitted to the measured concentrations of the involved species. This task is performed by a fit routine utilizing the Levenberg-Marquardt-Algorithm [122].

3 Characterization of the experimental setup

The goal of this thesis is to establish and characterize an experimental setup to study reactions of gas-phase metal clusters with various reactive gases. The focal point of these studies is chemical kinetics. Using the experimental setup described in the previous chapter, there are four main requirements to the determination of kinetic data for the reaction of ionic metal clusters with various reactive gases:

1. Storage of metal clusters in a broad mass range (typically 200 u - 20'000 u) for some milliseconds up to several seconds.
2. Variation of the reaction temperature over a broad temperature range.
3. Efficient ejection of the stored ions into the reflectron time-of-flight mass spectrometer to guarantee a sensitive product characterization.
4. A high resolution of the reflectron time-of-flight mass spectrometer in combination with the ring electrode ion trap to discriminate between the reaction products.

All of these demands are fulfilled, as will be shown by the results in this chapter. To characterize the performance of the experimental setup, cationic tantalum clusters (Ta_n^+, n=1..90) are produced and transferred into the ring electrode ion trap. Unless for accumulation studies, the trap was filled with clusters produced by a single pulse of the ablation laser. The pressure of the buffer gas within the trap is usually around 3 Pa. For clusters of more than 50 tantalum atoms, higher pressures of up to 5 Pa are needed in order to decelerate the clusters. Otherwise these clusters, which possess a higher kinetic energy, can overcome the repelling potentials of entrance and exit electrode and leave the trapping volume again.

3.1 Properties of measured mass spectra

A typical mass spectrum after a storage time of 9 ms is provided by Figure 3.1. The quadrupole mass filter was set to ion-guide mode, thus a broad distribution of cluster sizes is stored within the trap. Oxide species (Ta_nO^+) formed within the cluster source are not mass discriminated and are additionally observed in the measured mass spectrum. A maximum intensity for Ta_{19}^+ was achieved by optimizing the cluster source, ion-guides, frequency and amplitude of the RF-voltage to confine the ions within the ring electrode ion trap as well as the delay between ion extraction and pulsing the acceleration stage of the time-of-flight mass spectrometer. By changing any of these settings, the maximum of the distribution can be set to a different cluster size. It should be noted that the influence of these settings outweigh the natural distribution of cationic tantalum clusters due to the higher stability of certain cluster sizes [123], i.e., the detection of magic clusters is not straight forward. The mass resolution of the reflectron time-of-flight mass spectrometer is typically about 2'000 (FWHM).

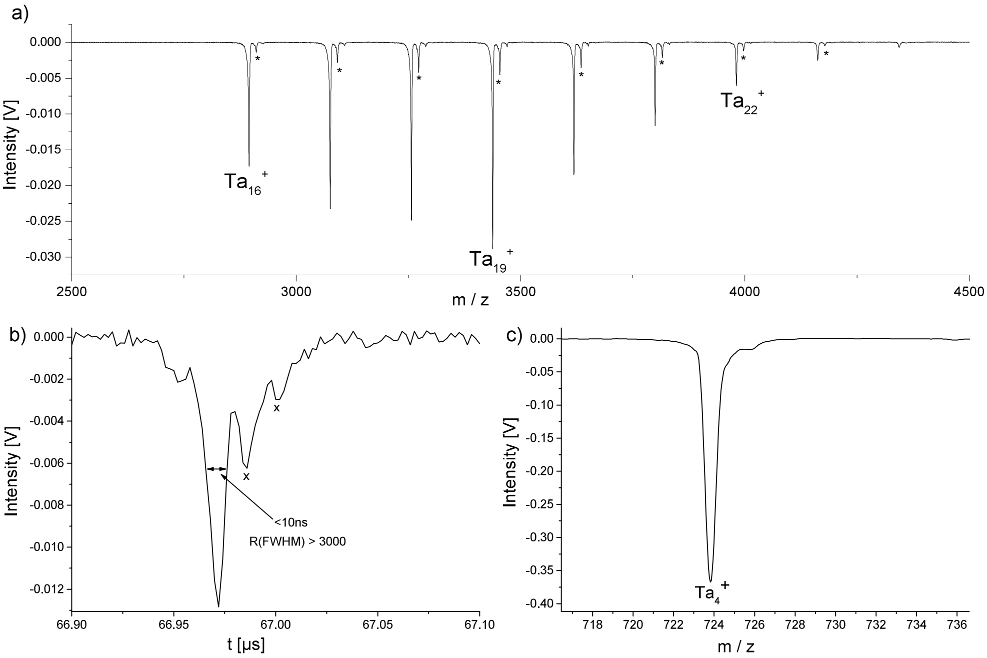

Figure 3.1: *a) Typical (unselected) mass spectrum for Ta_{16}^+ to Ta_{22}^+ after a storage time of 9 ms. Minor peaks indicated by an asterisk are oxide species formed within the cluster source. The experiment can be either optimized for maximum b) resolution or c) signal intensity. Peaks marked with a cross are due to electronic ringing.*

As illustrated in Figure 3.1 b) higher resolutions of at least 3’000 (FWHM) can be achieved. The peaks marked by a cross are due to electronic ringing between detector and the oscilloscope. In order to achieve a maximum resolution, the settings of the ion-guides between ring electrode ion trap and reflectron time-of-flight mass spectrometer have to be carefully optimized towards this goal. This comes at the expense of the overall transmission and causes a decrease in the measured signal intensity. Another prerequisite for a maximized resolution is a minimal gas load within the reflectron time-of-flight mass spectrometer. This may be achieved by a reduction of the buffer gas pressure within the trap, which in turn causes smaller storage efficiencies. Hence, the signal intensity decreases further, especially for larger clusters. When the quadrupole mass filter is set to ion-guide mode, peak intensities of typically 30-80 mV are measured. As shown in Figure 3.1 c) for size-selected clusters, intensities of several hundreds of mV are achieved . The increase in intensity may be attributed to two effects. Firstly, size-selection enables a more efficient optimization of clusters source, ion-guides and ring electrode ion trap for one specific size. Secondly, when no size-selection is applied the trap is filled above the space charge limit by a single pulse of the ablation laser, resulting in rapid ion loss. While size-selection decreases the overall number of clusters in the trap, more clusters of the selected size can be stored in the trap. The storage time of both measurements is 9 ms. These observations demonstrate that it is possible to tune the experimental setup either towards higher sensitivity or towards higher resolution of the reflectron time-of-flight mass spectrometer.

3.2 Enrichment of ions within the ring electrode ion trap

While typically clusters produced by a single pulse of the ablation laser are injected into the ring electrode trap, it is also possible to accumulate clusters formed by several laser pulses. This is of particular interest if only a few particles of the species of interest can be transferred to the ion trap. An example for this are metal cluster-adsorbate complexes formed by a crossed beam experiment, as shown in [124] for the present setup. The following measurement emulates such a situation to show the feasibility of accumulating ions within the ring electrode ion trap. In order to reduce the amount of Ta_5^+ clusters that are transferred to the trap, the ion-guides in front of the ion trap are detuned. As shown in Figure 3.2, clusters formed by a

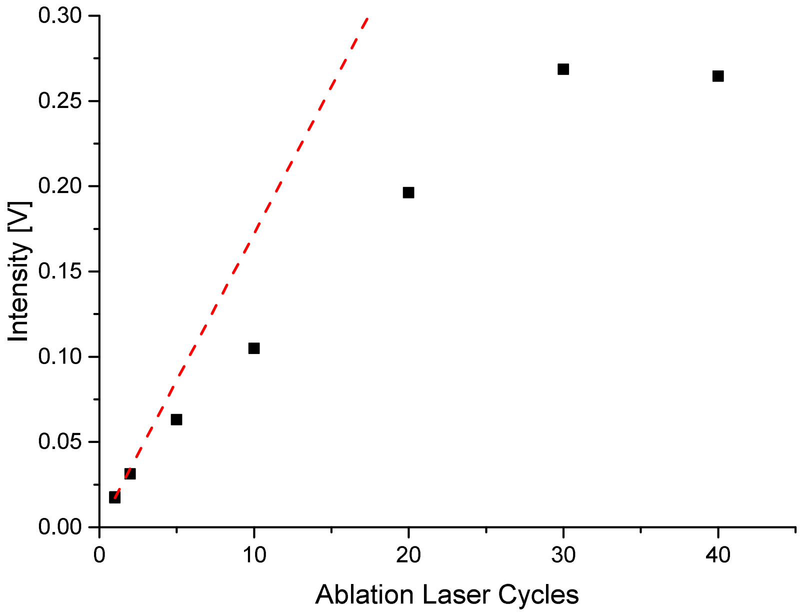

Figure 3.2: *Accumulated absolute intensity of* Ta_5^+ *as a function of the ablation laser cycles used to produce tantalum clusters.*

single laser pulse translate to a signal intensity of almost 18 mV. Neglecting ion loss due to imperfect storage, as well as any interference between ions already within the trap and newly arriving ions, doubling the intensity is expected when accumulating clusters over two ablation laser pulses. The expected linear dependence is shown as a red dashed line. The intensity measured after two cycles is 31 mV, which is slightly below this value. The effects of imperfect storage and interference between ions can no longer be neglected for higher ion densities caused by longer accumulation times. Hence, the measured intensity deviates further and further from the linear dependence. For accumulation times longer than 400 ms (40 cycles of the ablation laser) no further accumulation can be observed due to the space charge limit. In normal operation when all of the ion-guides are set to maximum transmission, similar intensities are achieved by collecting ions from a single pulse of the ablation laser. This observation indicates that the ion density in the trap is close to the space charge limit, even when size-selection is applied. Accumulation from a second laser pulse does not result in a significant increase of the measured intensity.

3.3 Storage characteristics and kinetic evaluation

The storage characteristics of the ring electrode ion trap can be quantified by two criteria:

- How long can ions be stored within the ion trap?
- What is the maximum possible mass range of ions stored within the trap?

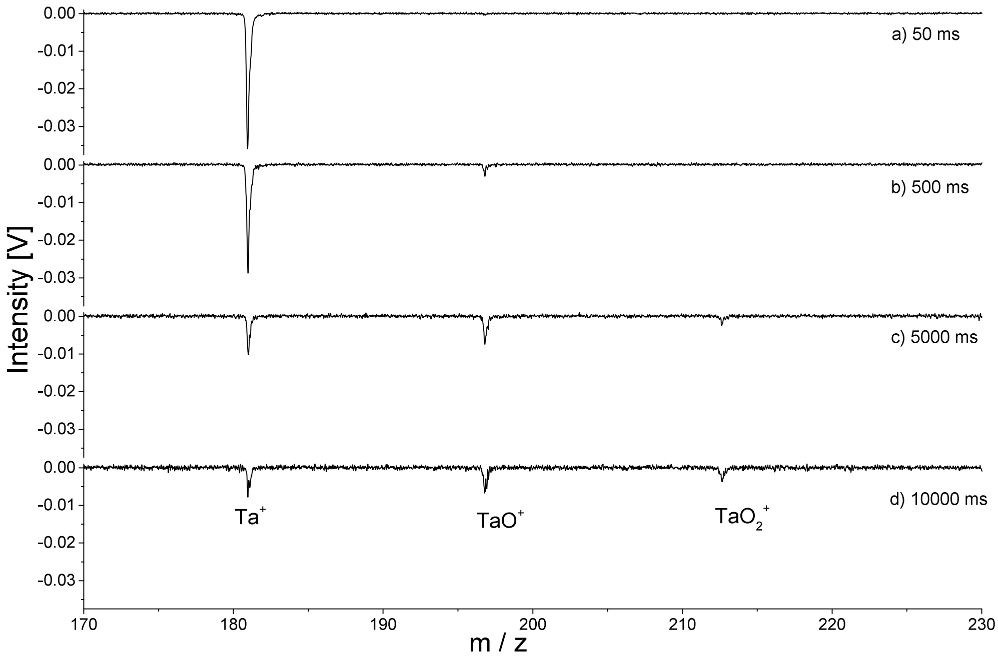

Figure 3.3: *Mass Spectra of* Ta^+, TaO^+ *and* TaO_2^+ *for a storage time of a) 50 ms, b) 500 ms, c) 5000 ms and d) 10000 ms at 250 K.* TaO^+ *and* TaO_2^+ *are formed by a reaction of* Ta^+ *with water impurities.*

To demonstrate the storage capabilities at the low end of the mass range, Ta^+ ions are stored within the ion trap at a temperature of 250 K. Figure 3.3 a) depicts a mass spectrum measured after a storage time of 50 ms. The intensity of the peak that corresponds to Ta^+ is more than 30 mV and no other species can be detected. Increasing the storage time by a factor of 10 to 500 ms (b) results in the appearance of a second peak in the spectrum. This peak can be assigned to TaO^+, which is likely formed by reaction with water impurities adsorbed onto the ring electrode trap. Previously, it was found that gas phase neutral tantalum atoms are able to break the O-H bond of water molecules [125]. The sum of the intensities of these two peaks still exceeds 30 mV.

As illustrated in Figure 3.3 c), for storage times longer than 5000 ms an additional species, TaO_2^+, is detected. For a storage time of 10000 ms (d), still peaks corresponding to these three species are present in the measured mass spectrum. Their combined intensity is almost 20 mV. This experiment demonstrates the capability to store atomic tantalum ions (180.95 u) within the trap for at least 10 s. The primary species Ta^+ is depleted by two effects: by imperfect confinement of the ions and by reactions with impurities. As gas phase tantalum clusters readily react with water [126], oxygen [127] and nitrogen [128], the reaction with impurities is the major loss channel.

In a second experiment the overall storage efficiency as well as the first kinetic evaluation will be shown simultaneously. For this experiment the trap is cooled down to 35 K. Ta_5^+ clusters are produced and guided into the ring electrode ion trap. Two mass spectra are provided by Figure 3.4. The first one, illustrated as solid black line, is recorded after a storage time of 0.1 s. Ta_5^+ is the dominant species within the ion trap, with minor components corresponding to $Ta_5N_2^+$ and Ta_5O^+. The relative abundance of Ta_5O^+ decreases with increasing reaction time. Hence, this species is not formed within the ion trap. It is probably generated during

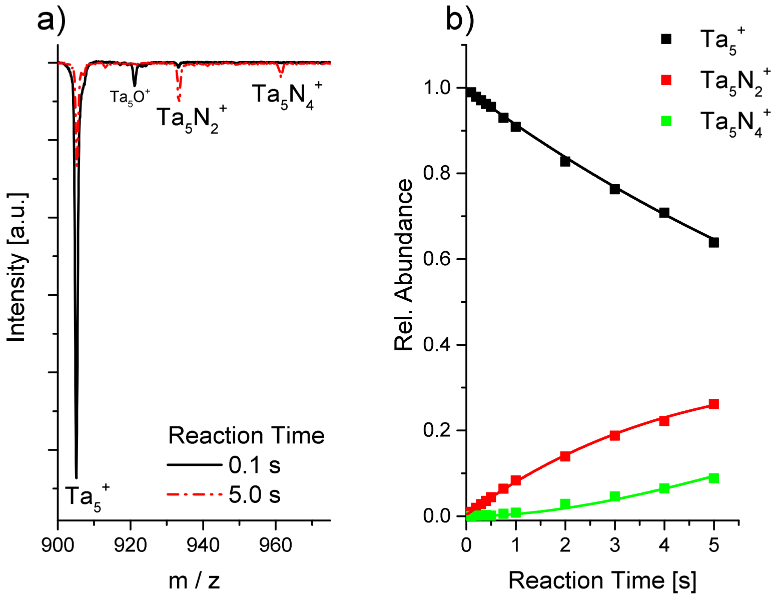

Figure 3.4: *Mass spectra of Ta_5^+ for storage times of 0.1 s (solid black line) and 5.0 s, respectively (dashed red line). b) Calculated relative abundances of Ta_5^+ and the formed reaction products $Ta_5N_2^+$ and $Ta_5N_4^+$. The solid lines represent the result of the kinetic fit. Adapted with permission from [105]. Copyright 2015 Elsevier.*

the cluster formation process within the cluster source and is, therefore, neglected in further discussions.

For a reaction time of 5.0 s (red dashed line) $Ta_5N_2^+$ has become more abundant. Additionally $Ta_5N_4^+$ can be detected. Nevertheless, Ta_5^+ is still the most abundant species. The reaction of nitrogen with cationic tantalum cluster may be described by a straightforward attachment of nitrogen molecules:

$$Ta_5^+ \xrightarrow{k_1} Ta_5N_2^+ \xrightarrow{k_2} Ta_5N_4^+ \ldots \xrightarrow{k_6} Ta_5N_{12}^+ \ldots . \tag{3.1}$$

Assuming this model, the relative abundance of the involved reaction species can be fitted with respect to the measured abundances. As illustrated in Figure 3.4 b) an excellent agreement between the fit (solid lines) and measured data (symbols) is achieved. The calculated rate constants are summarized in Table 3.1.

Table 3.1: *Calculated pseudo-first order rate constants for the reaction of* Ta_5^+ *and* Ta_{50}^+ *with nitrogen.*

	Ta_5^+	Ta_{50}^+		Ta_5^+	Ta_{50}^+
k_1 [1/s]	0.087	1.226	k_1 [cm^3/s]	$1.2 \cdot 10^{-11}$	$1.7 \cdot 10^{-10}$
k_2 [1/s]	0.120	0.915	k_2 [cm^3/s]	$1.7 \cdot 10^{-11}$	$1.3 \cdot 10^{-10}$
k_3 [1/s]	-	0.652	k_3 [cm^3/s]	-	$9.2 \cdot 10^{-11}$
k_4 [1/s]	-	0.591	k_4 [cm^3/s]	-	$8.4 \cdot 10^{-11}$
k_5 [1/s]	-	0.615	k_5 [cm^3/s]	-	$8.7 \cdot 10^{-11}$
k_6 [1/s]	-	0.389	k_6 [cm^3/s]	-	$3.9 \cdot 10^{-11}$

The partial pressure of nitrogen can be measured with a residual gas analyzer (SRS) within the ion trap chamber, but unfortunately not directly inside of the ring electrode ion trap. Consequently, the actual partial pressure of nitrogen within the trap is unknown. The measured partial pressure at the ion trap chamber is 10^{-9} mbar, it is therefore reasonable to assume a pressure of 10^{-7} mbar inside of the storage volume. A more in detail discussion on kinetics in the gas phase is given in the next chapter. Considering a constant partial pressure of nitrogen, in the next step pseudo-first order rate constants can be calculated. As shown in Table 3.1 they are

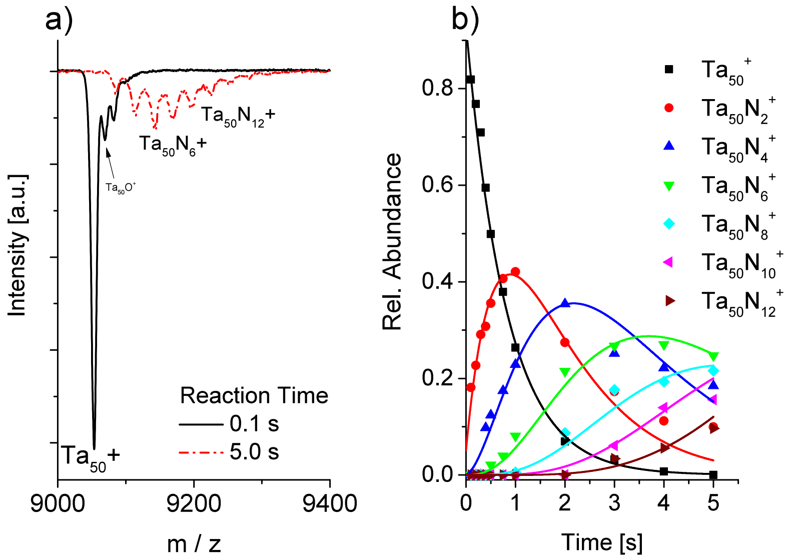

Figure 3.5: *a) Mass spectra of* Ta_{50}^+ *for storage times of 0.1 s (solid black line) and 5.0 s respectively (dashed red line). b) Calculated relative abundances of* Ta_{50}^+ *and the reaction products from* $Ta_{50}N_2^+$ *to* $Ta_{50}N_{12}^+$*. The solid lines represent the result of the kinetic fit.*

in the order of 10^{-11}cm^3/s for Ta_5^+.

The same experiment was repeated for Ta_{50}^+ clusters with similar results. Again a consecutive attachment of nitrogen molecules can be observed (see Figure 3.5 a). Although compared to Ta_5^+, Ta_{50}^+ is much more reactive. After a reaction time of 1 s, $Ta_{50}N_2^+$ already is the most abundant species within the spectrum. As shown in Figure 3.5 b), beside $Ta_{50}N_2^+$ and $Ta_{50}N_4^+$ additional species such as $Ta_{50}N_{12}^+$ are formed. Again a good agreement between measurement and fit is achieved. Table 3.1 shows reaction rates that are roughly one order of magnitude higher compared to Ta_5^+. By determining the rate constants in a consecutive reaction with multiple reactants, these first results demonstrate the capability to evaluate the kinetics of reactions in the gas phase.

The previous results are used to estimate the loss of ions due to imperfect confinement of the ions while being stored in the trap. This estimation requires all reactants and reaction products to be taken into account. Therefore, the intensities of all species corresponding to the same cluster size are summed up. Figure 3.6 illustrates the total normalized intensities for Ta_5^+ and Ta_{50}^+. In general, more than 75% of the injected clusters are still within the trap after 1 s, more than 40% remain after 5 s, and more than 20% are detected after 10 s.

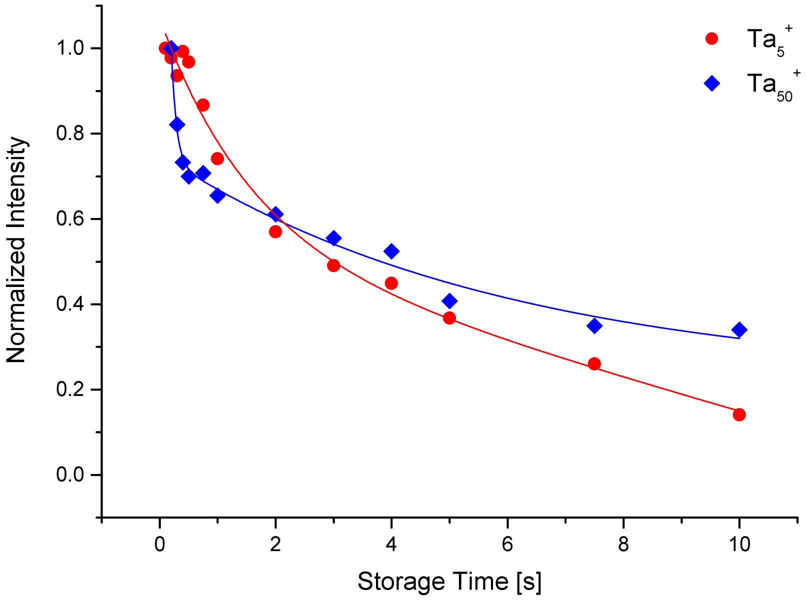

Figure 3.6: *Normalized total intensity of* Ta_5^+ *and* Ta_{50}^+ *as a function of the storage time. Adapted with permission from [105]. Copyright 2015 Elsevier.*

The loss of intensity can be fitted by an exponential decay with two time constants. The first time constant is in the range of some tens of ms; the second one is in the order of some seconds. This finding indicates the presence of two different loss mechanisms. The quick initial loss is likely connected to ion loss before the clusters are completely thermalized, which results in somewhat undefined storage conditions. Since the thermalization is slower for larger clusters [96], this effect is more pronounced for Ta_{50}^+ than for Ta_5^+. As stated afore, when cluster synthesized by two or more laser pulses no significant increase in the detected signal intensity is observed. This indicates that the trap is filled above the space charge limit by a single pulse of the laser. Such an 'over saturation' would result in rapid loss of ions until the ion density is well below this limit. The second time constant is probably due to an imperfect confinement of the clusters. However, as demonstrated, it is easily possible to store ions within the trap for more than 10 s and still obtain mass spectra with good signal to noise ratio. In fact, much longer storage times of 5 minutes have been achieved with the current setup.

To estimate the upper mass limit of the experimental setup, the experiment is optimized to form and guide large clusters. The quadrupole mass filter is set to ion-guide mode in order to overcome its mass limit of 16'000 u. Cluster source, ion-guides and ring electrode trap are optimized for large clusters. The temperature of the trap is kept at 35 K. Figure 3.7 depicts the mass spectrum measured after a storage time of 9 ms (black line). The smallest observed cluster is Ta_{52}^+ and the biggest one is Ta_{90}^+ with a mass of approximately 16’200 u. The maximum of the size distribution is found at Ta_{75}^+. After a storage time of 500 ms significant intensities are still detected. The overall shift of the peaks towards higher masses again relates to a reaction of the clusters with the background gas. In summary, these experiments show that ions with masses between 200 u and 16’000 u can be stored in the ion trap for at least 10 s. As Ta_{90}^+ was the largest that could be synthesized in sufficient quantities with the described cluster source and guided to the ring electrode trap, it was not possible to determine the actual upper mass limit for ion storage. Nevertheless, ions of a broad mass range can be safely stored within the trap.

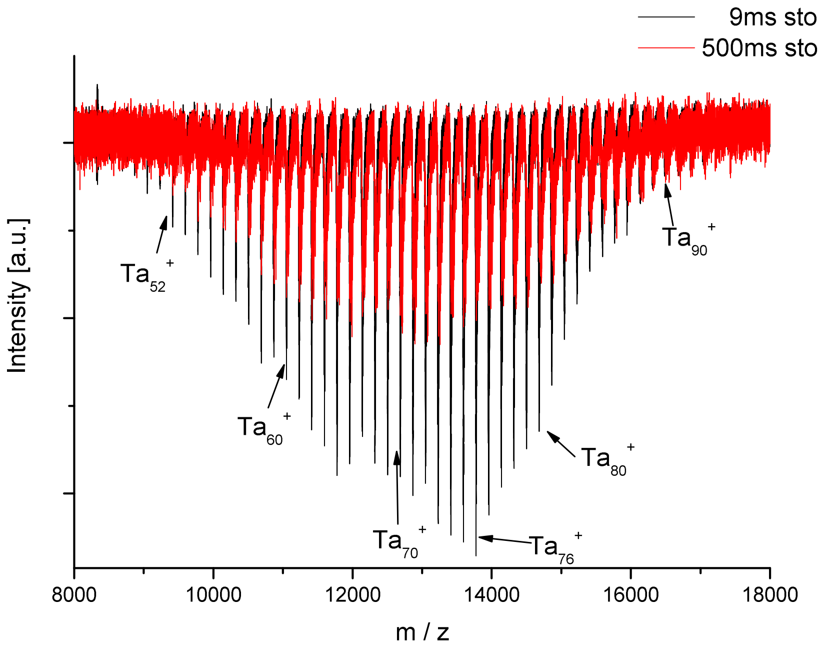

Figure 3.7: *Large tantalum clusters comprising up to 90 atoms are synthesized and stored within the ring electrode trap for 9 ms (black) and 500 ms (red). Again a reaction of the clusters with impurities is observed. Adapted with permission from [105]. Copyright 2015 Elsevier.*

In order to achieve long storage times, the amplitude and frequency of the RF-potentials applied to the ring electrodes have to match the mass of the particles that are stored. Empirical peak-to-peak amplitudes and frequencies as a function of the mass of the stored particles are illustrated by Figure 3.8. In general, two trends

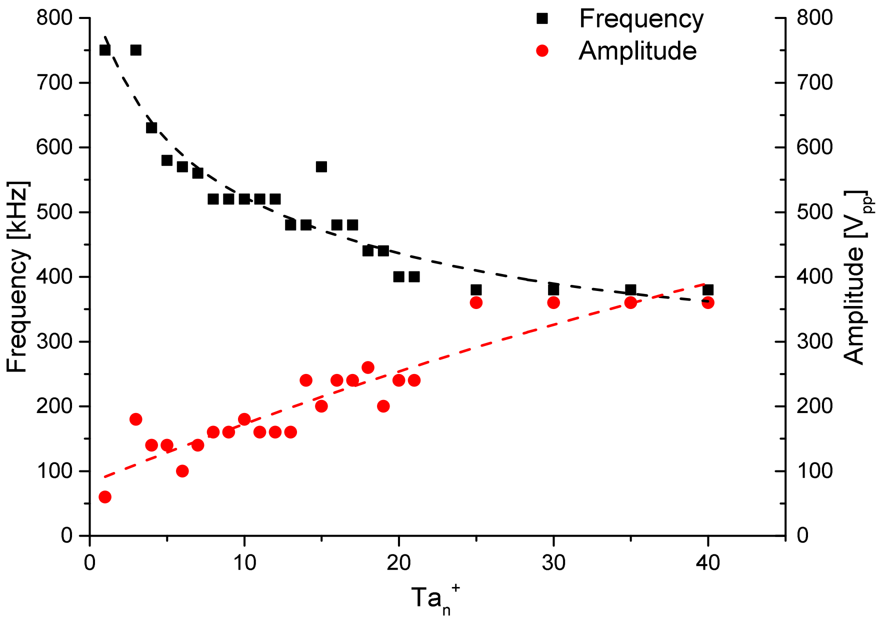

Figure 3.8: *Empirical frequencies and peak-to-peak amplitudes of the RF-potentials applied to the ring electrodes in order to confine ions as function of their mass. The dashed lines function as a guide to the eye.*

can be observed. The amplitude increases for higher masses, whereas the frequency decreases as particles with a higher mass are slower. The decrease in frequency is in good agreement with trends calculated for multipole ion traps [50].

3.4 Extraction characteristics

A pre-requisite for the combination of a ring electrode ion trap with a reflectron time-of-flight mass spectrometer is a controlled and efficient ion extraction method. Previous attempts were hampered by undefined extraction fields [110]. The combination of ring electrode ion trap with the described electronics unit allows to create defined pseudo-linear fields. Additionally, this enables the realization of more sophisticated fields.

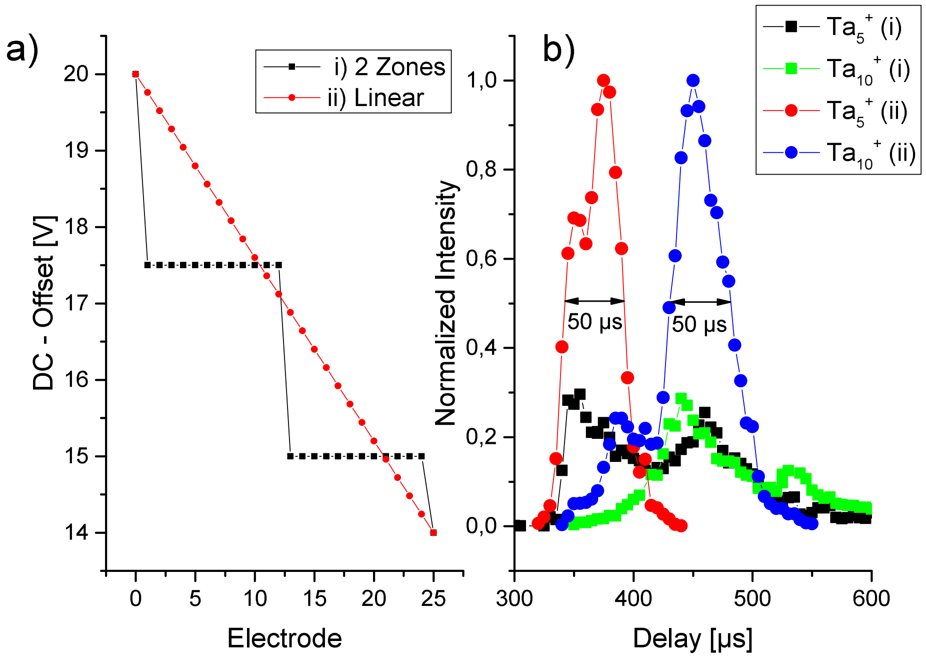

Figure 3.9: *a) Two exemplary sets of DC-offsets to create an extraction field. In the case of i) the trap is divided into two zones with different DC-offsets, for ii) a pseudo-linear field is created. b) Corresponding signal intensity of two cluster sizes as a function of the delay between extraction and pulsing of the time-of-flight mass spectrometer. Adapted with permission from [105]. Copyright 2015 Elsevier.*

Two extraction fields are compared to demonstrate the ion extraction properties. The DC-offsets used to create these fields are shown in Figure 3.9 a). For the first extraction field i) the ring electrode ion trap is divided into two zones. The entrance electrode is set to 20 V, the DC-Offset for electrodes 1-12 is at 17.5 V, for electrodes 13-24 at 15 V and the exit electrode is set to 14 V. In a second experiment a pseudo linear extraction field ii) is created by linearly decreasing DC-Offsets from the entrance electrode (20 V) to the exit electrode (14 V). These two extraction fields are then utilized to eject Ta_5^+ and Ta_{10}^+ from the ion trap, after having been stored for 0.1 s. To characterize the time profile of the ejected cluster beam, the delay between ion extraction and the pulsing of the acceleration plates of the reflectron time-of-flight mass spectrometer is systematically varied.

The resulting normalized intensity is depicted in Figure 3.9 b) as a function of the delay. Tantalum metal clusters typically need some hundreds of seconds to arrive at the acceleration stage. Lighter clusters arrive earlier as they are accelerated to higher velocities. For extraction field i) the ion beam is spread for at least 200 µs in time for both cluster sizes. In the case of the pseudo-linear field the time distribution is much tighter; for Ta_5^+ the beam is roughly 70 µs long. The full width half maximum for both cluster sizes is 50 µs. The intensity for extraction field ii) is increased by a factor of three compared to extraction field i). Thus, when a high sensitivity of the experiment is required, pseudo-linear fields can be exploited to create high peak intensities. On the other hand, when product of a large mass distribution shall be analyzed at the same time, it is advantageous to exploit different field shapes with larger 'time overlaps'(e.g., consisting of two zones or more sophisticated fields). The flexibility of the newly developed electronics unit of the ring electrode ion trap allows optimization in both cases.

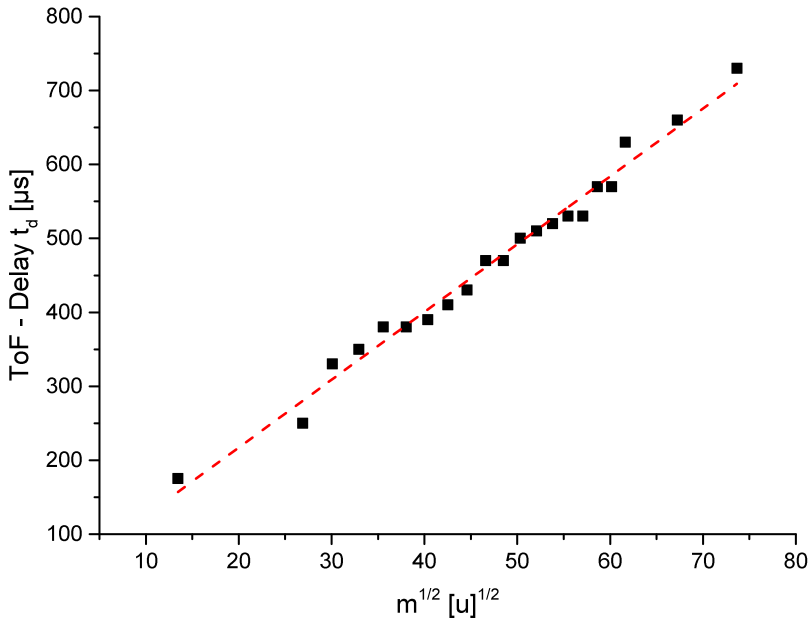

Figure 3.10: *Empirical delays between the ion extraction from the trap and the pulsing of the acceleration plates as function of the square root of the mass of the stored ions.*

Figure 3.10 depicts typical delays t_D between ion extraction from the ring electrode ion trap and the pulsing of the acceleration plates of the reflectron time-of-flight mass spectrometer for the pseudo-linear field illustrated in Figure 3.9 b). The delays have been determined experimentally by mass selecting and storing a certain cluster size within the trap. The delay was then optimized for maximized intensity. The delay scales linearly with the square root of the mass of the stored (dashed red line).

This is analogous to the relation found for the flight times in time-of-flight mass spectrometry. Furthermore, this correlation allows the prediction of the optimal delay, t_D, when a certain mass is stored. By combining the known 'peak form' shown in Figure 3.9 b) and the correlation between mass and delay as shown in Figure 3.10, measured intensities can be corrected for 'non-ideal' delays. This is particularly important when ions of a wide mass range shall be detected. Instead, for the course of this work, mass spectra have been measured at several delays when necessary.

In summary, ions of a wide mass range (200 u to more than 16'000 u) can be stored for more than 10 s, which is possible due to a high storage efficiency. The setup furthermore allows to follow the reaction of tantalum clusters with nitrogen impurities at 35 K and the related reaction rates (in the order of $1 \cdot 10^{-10}$ to $1 \cdot 10^{-11} cm^3/s$) have been determined. The extraction characteristics of the ring electrode ion trap can either be optimized towards a high sensitivity for one particular mass or towards a large mass range. Additionally, the product characterization via time-of-flight mass spectrometry can either be tuned for a high resolution or a high sensitivity. These characteristics are the foundation to conduct the studies shown in the following chapters.

4 Oxidation of cationic tantalum clusters

The reaction of molecular oxygen with cationic tantalum clusters with 4 to 40 atoms is studied with the described experimental setup. In order to perform these experiments, 100 ppm of oxygen (6.0, Westfalen) is mixed into the helium buffer gas (6.0, Westfalen). The pressure of this gas mixture within the trap is set to 3 Pa. After a short introduction, the results of these experiments will be discussed in detail for some selected cluster sizes.

4.1 Introduction

Today tantalum is used for a wide range of various applications from electronics [129] to medical tools [130] due to its high resistivity towards corrosion. Of particular interest are tantalum oxides, utilized for example as optical coatings [131], protective coating for sensors [132] or electrode materials in electrochemistry [69]. Looking at the microscopic scale and beyond tantalum and its oxides are interesting due to their reactivity. Basame et al. showed that only certain sites of Ta-Ta_2O_5 electrodes are active for certain redox reactions [133]. Mesoporous tantalum oxide was found to decompose water [134]. In fact, tantalum oxides catalyze a broad range of chemical reactions. An important example is the oxidation of hydrocarbons including methane [70]. Gas phase tantalum oxides mediate the coupling of methane and carbon dioxide [61]. Beside atomic tantalum, also the reactivities of small tantalum cluster oxides have been studied extensively. Metal clusters feature unique, often not scaleable properties [24]. Particularly in gas phase, they are good model systems for catalysis [52]. Neutral tantalum oxide clusters have been found to react readily with NO and NH_3 [135]. Cationic clusters react with 1-butene, 1,3-butadiene and benzene by the a cracking of a C-C bond [71]. For ethane and ethylene, association and molecular oxygen loss have been observed [136]. In contrast to that, relatively few studies on the bare clusters exist. He and co-workers found that neutral tantalum clusters dehydrogenate unsaturated hydrocarbons [43]. Cationic tantalum clusters dehydrogenate small alcohols or cause the dissociation of their C-O bond [124]. These clusters are also able to activate nitrogen [128]. While only few of the mentioned reactivity studies provide kinetic data, to the best knowledge of the author, up to now no study about larger tantalum clusters with more than 10 atoms exists. Using the experimental setup described beforehand enables variation of reaction temperature, time and pressure. Thus, the kinetics of the reaction can be studied. Within the next sections the reaction of cationic tantalum clusters with oxygen is discussed and a detailed reaction mechanism based on the obtained kinetic data is proposed.

The kinetic analysis, furthermore, reveals phenomena that relate to the structure of the cluster. The structure of small cationic tantalum clusters are characterized by an early transition from a 2D to a 3D configuration as the tetramer already has a three dimensional structure [137]. While some work has been done on the structure of smaller tantalum clusters [126] and even tantalum cluster oxides [138], [139], up to now only one theoretical study reports the structures of larger tantalum clusters cations up to Ta_{16}^{+} [140]. A further study makes some predictions on the structure of such clusters by the occurrence of magic clusters sizes, obtained by time-of-flight mass spectrometry [123]. Hence, the present observations even may help to shed some light on the cluster structure [141]. Before a kinetic evaluation can be performed an understanding of ion-molecule reaction principles in the gas phase is necessary. The following chapter will give a brief summary of the underlying theoretical description.

4.2 Kinetics and limitations in the multi-collision regime

The reaction of small free metal clusters with oxygen has been extensively studied [65, 63, 142]. In the simplest case an association reaction is observed:

$$M_n^+ + O_2 \xrightarrow{k_{app}} M_nO_2^+. \tag{4.1}$$

Note that the same formalism can also be applied to anions. For almost any system the apparent rate constant k_{app} increases with decreasing temperature. This would translate to a formally negative activation energy, which is indicative for a more complex reaction mechanism. The observation of a negative activation energy can be explained by a Lindemann reaction mechanism [120] [143]. Upon collision between a metal cluster $\mathrm{M_n^+}$ and an oxygen molecule $\mathrm{O_2}$ an activated complex $\mathrm{MO_2^{+^*}}$ is formed.

$$M_n^+ + O_2 \underset{k_b}{\overset{k_a}{\rightleftharpoons}} M_nO_2^{+*} \tag{4.2}$$

The formation of the activated complex, described by k_a can be regarded as a barrierless ion-molecule association processes, which does not strongly depend on the temperature [144] [145]. It depends almost solely on the collision frequency between metal cluster and oxygen molecule, as described by the Langevin theory [146] [120].

$$M_nO_2^{+*} \xrightarrow{k_s} M_nO_2^+ \tag{4.3}$$

The activated complex can either dissociate to $\mathrm{M_n^+}$ and $\mathrm{O_2}$ expressed by k_b, or it can be stabilized to $\mathrm{MO_2^+}$. Reaction studies within multipole ion traps are performed in the so-called multi-collision regime. At a pressure of 1 Pa each metal cluster collides with a buffer gas atom each 3 µs [63]. Hence, the activated complex can be stabilized by collisions. The stabilization process is also almost independent from the temperature. The concentration of the buffer gas $[He]$, however, may influence the rate constant of the stabilization reaction. Consequently, the reaction is of third order. Other possibilities are radiative relaxation or internal redistribution of the association energy [62]. The only rate constant that significantly depends on the temperature is the back reaction, described by k_b. As this rate constants k_b increases with increasing temperature, the apparent rate constant k_{app} for the overall reaction decreases. The rate equations for $[M_n^+]$ and $[M_n^{+*}]$ can be written as:

$$\frac{d[M_n^+]}{dt} = -k_a[M_n^+][O_2] + k_b[M_nO_2^{+*}] \tag{4.4}$$

$$\frac{d[M_n^{+*}]}{dt} = +k_a[M_n^+][O_2] - k_b[M_nO_2^{+*}] - k_s[M_n^{+*}][He]. \tag{4.5}$$

Assuming short lived activated complexes it is possible to apply a steady state approximation for the activated complex [147] [148]. Equation 4.4 can be written as:

$$\frac{d[M_nO_2^+]}{dt} = -\frac{k_a[M_n^+][O_2]k_s[He]}{k_b + k_s[He]} = k^{(3)}[M_n^+][O_2][He], \tag{4.6}$$

with

$$k^{(3)} = \frac{k_a k_s}{k_b/[He] + k_s}. \tag{4.7}$$

As the buffer gas and reactive gas are constantly injected into the ion trap, both concentrations remain constant throughout the reaction. Hence, the rate equation is of pseudo-first order and can be simplified to:

$$\frac{d[M_n^+]}{dt} = k^{(1)}[M_n^+] \quad k^{(1)} = k^{(3)}[O_2][He] \tag{4.8}$$

If the dissociation of the activated complex is favored compared to the stabilization k_s, Equation 4.8 can be further simplified to:

$$k^{(1)} = \frac{k_a k_s}{k_b}. \tag{4.9}$$

To determine absolute rate constants, it is necessary to know the pressures the of reactive gas and buffer gas within the ion trap. The pressure in the trap is not constant in space, but varies along the axis of the trap [95]. The pressure gradient, however, remains constants for all measurements at a certain pressure. The pressure measured by a single gauge represents an averaged value. The measurement of this averaged pressure in the trap is not straightforward and differs significantly from the pressure in the surrounding chamber. Consequently, pressure measurements typically have large absolute error margins. Kappes and co-workers estimated that their pressure measurement has an absolute error of 50% [62] and the same error margin is assumed for present work. Hence, the calculated rate constants have large absolute error margins, as well. The deviation of the pressure for different measurements is much smaller. Thus, rate constants obtained from different measurements can be determined with high accuracy while their absolute value is subject to a large error. In fact, rate constants determined from different measurements showed a deviation of less than 10%.

The role of the buffer gas is ambiguous. Due to the diluted gas phase, stabilization via buffer gas collisions may play an important role. Consequently, partial pressures of the buffer gas may be included into the kinetic model as it is done in Equation 4.6. However, other relaxation processes like fragmentation of the reactant may be important. For reactants with a big heat capacity, the back reaction may be reasonably slow and therefore k_b very small. In fact, almost all reactions discussed in following proceed comparably fast. This observation indicates that the back reaction is strongly suppressed. In such a scenario $k^{(1)}$ may be approximated by association rate constant k_a. Thus, the helium concentration does not influence the reaction significantly. As the scope of this work is to describe the reaction with the simplest model possible only the concentration of the reactive gas is included. For further studies, the concentration of the reactant gas may be kept constant whereas the concentration of the buffer gas is systematically varied. This procedure allows to disentangle the influence of the concentration of reactive gas and buffer gas.

4.3 Reactions of larger tantalum clusters - Indications for two reaction mechanisms

In a first part, the reaction of larger tantalum clusters with more than 13 atoms is discussed on the example of Ta_{20}^+. The reaction of Ta_{20}^+ with oxygen is studied at 300 K and 50 K and pseudo-first order rate constants are determined. Variation of the reaction temperature enables determination of activation energies. In a second part, the obtained results are discussed and a model for the observed reaction is proposed.

4.3.1 Reaction at 300K

Figure 4.1 a) depicts a mass spectrum after a reaction time of 10 ms for a reaction temperature at 300 K. Ta_{20}^+ is still the most abundant species, although a significant part of the clusters has reacted with oxygen. Major reaction products are $Ta_{20}O_2^+$ and $Ta_{20}O_4^+$. Peaks with an odd number of oxygen atoms are marked with a cross. These species originate from a side reaction with water adsorbed at the electrodes of the trap [126] and because of their low intensity they are neglected for the subsequent discussion.

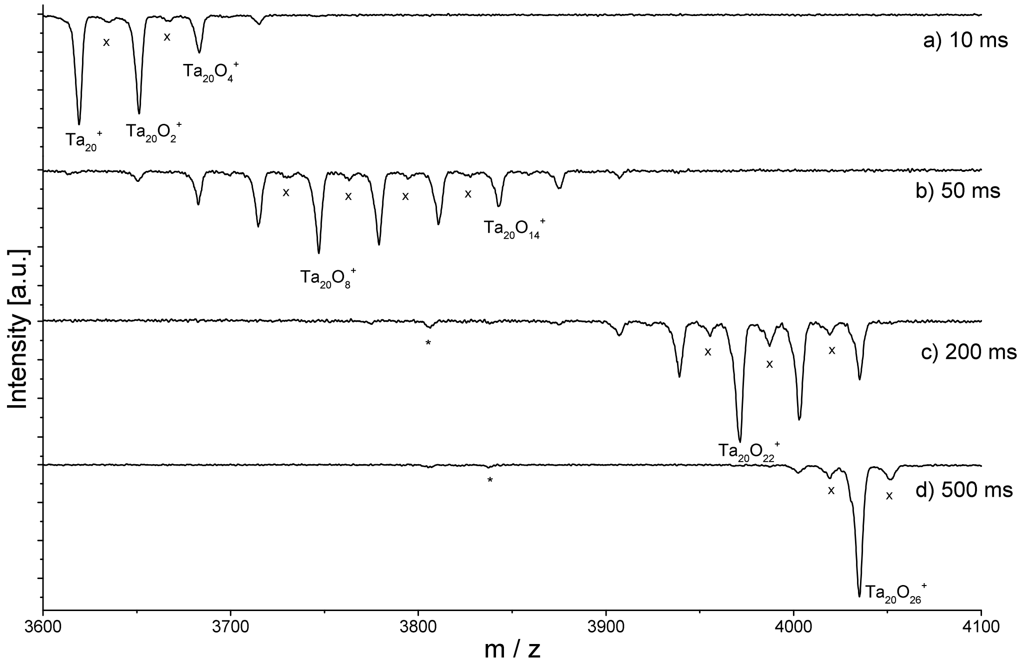

Figure 4.1: *Mass spectra for the reaction of Ta_{20}^+ with molecular oxygen recorded at reaction times of a) 10 ms, b) 50 ms, c) 200 ms and d)500 ms at 300 K. Peaks marked with a cross are caused by a side reaction with water background and * marked peaks appear due to a side reaction that results in the fragmentation of the tanatlum cluster. The main reaction channel is the subsequent attachment of oxygen molecules to the tantalum (oxide) cluster, until the final product $Ta_{20}O_{26}^+$ is formed.*

As illustrated in Figure 4.1 b), the signal of Ta_{20}^+ has almost completely vanished after 50 ms. This finding already demonstrates the high reactivity of cationic tantalum clusters towards oxygen. A broad distribution of reaction products, ranging from $Ta_{20}O_2^+$ to at least $Ta_{20}O_{16}^+$ can be found in the spectrum. The most abundant species after this reaction time is $Ta_{20}O_8^+$. After 200 ms, Figure 4.1 c), the distribution is much narrower with $Ta_{20}O_{22}^+$ being the most prominent reaction product. The reaction of Ta_{20}^{+} with oxygen stops at $Ta_{20}O_{26}^{+}$. Consequently, $Ta_{20}O_{26}^{+}$ is the only species for reaction times longer than 500 ms, Figure 4.1 d).

Rate constants are obtained from the measured time-dependent concentration of the reaction products by assuming a straightforward consecutive addition of oxygen molecules to the tantalum cluster:

$$Ta_{20}^{+} \xrightarrow{k_1} Ta_{20}O_2^{+} \xrightarrow{k_2} Ta_{20}O_4^{+} \xrightarrow{k_3} \ldots \xrightarrow{k_{13}} Ta_{20}O_{26}^{+}. \qquad (4.10)$$

Oxygen and buffer gas are constantly injected into the trap, thus the oxygen concentration remains constant during the reaction and calculated rate constants are of pseudo-first order. Figure 4.2 illustrates intensities measured for Ta_{20}^{+} as well as

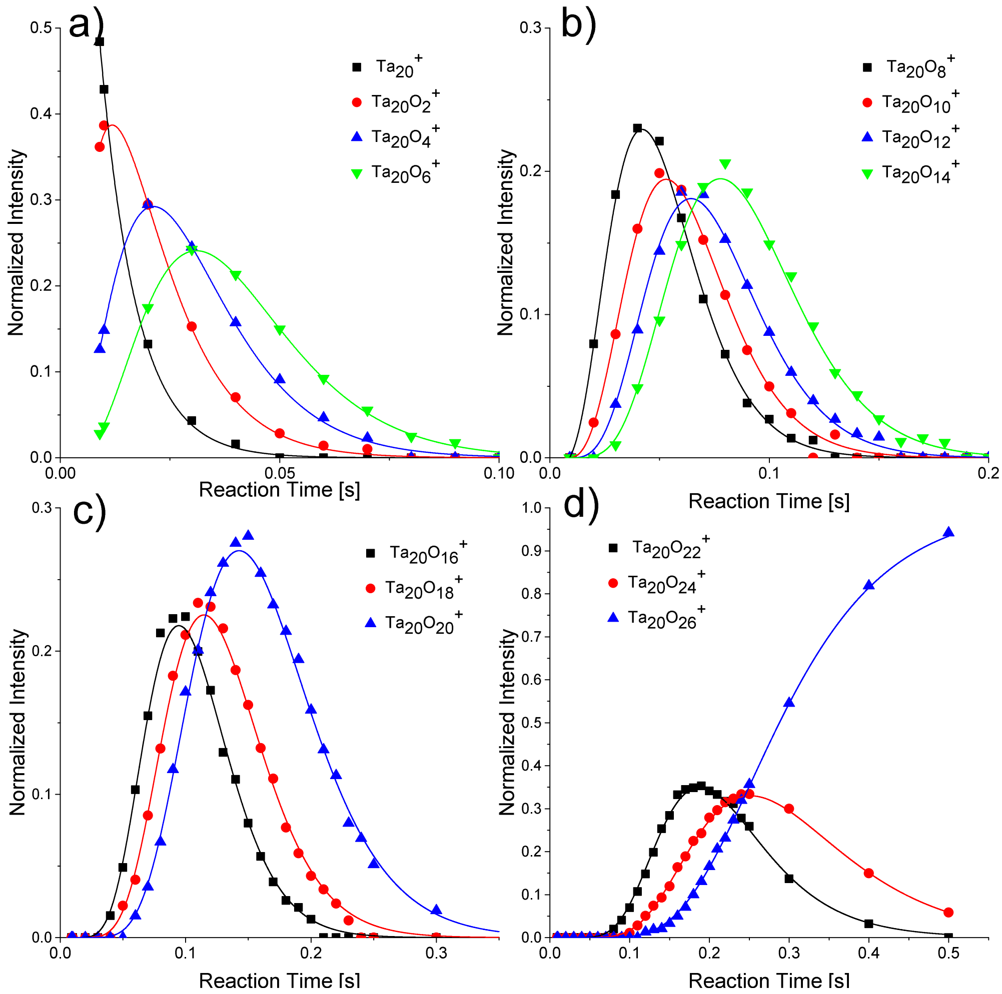

Figure 4.2: *a) - d) Normalized intensities of the reactants as a function of the reaction time. The results of the kinetic fit are depicted as solid lines.*

for all reaction products as a function of the reaction time. Ta_{20}^{+} is seen to vanish rapidly, and it cannot be detected anymore after a few tens of milliseconds. Intermediate species like $Ta_{20}O_2^+$ or $Ta_{20}O_4^+$ can only be detected for roughly 100 ms. Higher oxides, however, are present in spectra for longer time spans. For example $Ta_{20}O_{22}^+$ can be detected over a period of at least 400 ms. The black solid lines represent the result of the kinetic fit. For all of the involved species a very good agreement between fit and experimental data is achieved.

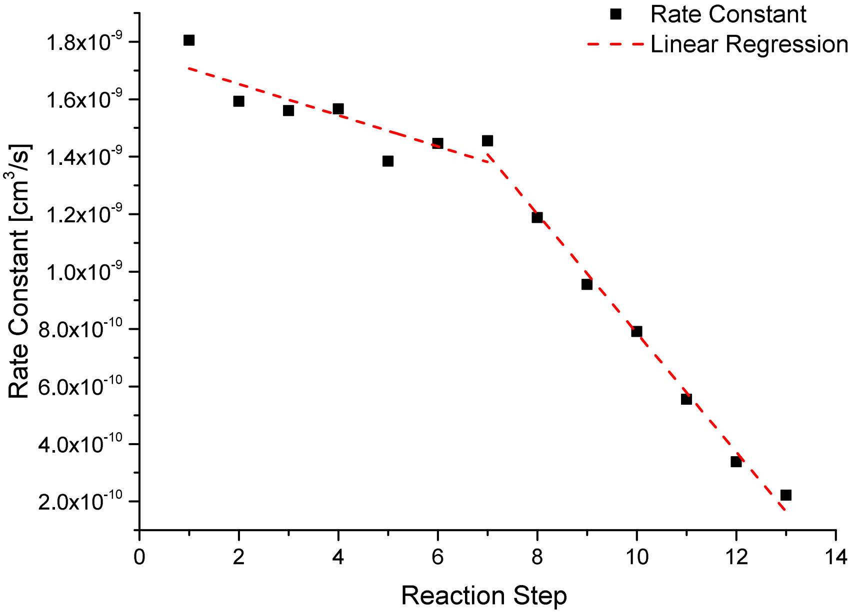

Figure 4.3: *Pseudo-first order rate constants for all of reactions steps at 300 K. The dashed red lines represent a linear regression for reaction steps 1-7 and 7-13 respectively.*

The corresponding pseudo-first order rate constants of all reaction steps are calculated and depicted in Figure 4.3. The first reaction step ($Ta_{20}^+ \xrightarrow{k1} Ta_{20}O_2^+$) is found to be the fastest with a reaction rate of approximately $2 \cdot 10^{-9}$ cm^3/s. This value is close to the collision frequency reported in [62] for small gold clusters. When taking into account the pressure of the buffer gas a rate constant of $2 \cdot 10^{-24}$ cm^3/s is determined. This rate constant is more than three orders of magnitude larger compared to the rate constant found for reaction of small gold clusters with oxygen by Bernhardt and co-workers [63]. As the oxidation of Ta_{20}^+ progresses rapidly at a quite low oxygen concentration this result appears reasonable.

In general, the reaction rate decreases with each reaction step. In a simple approximation, Ta_{20}^+ has 13 adsorption sites for oxygen molecules. Each attached oxygen molecule would block one site. A 'successful' attachment gets increasingly unlikely. In such a scenario the reaction rate would decrease linearly. However, such a behavior is not found. Instead two regimes are observed, the first one for reaction steps 1-7 (k_1-k_7), the second one from 7-13 (k_7-k_{13}). For both regimes the reaction rate decreases linearly, but with different slopes. These findings strongly indicate that two different reaction mechanisms are present for the reaction of molecular oxygen with Ta_{20}^+. The potential mechanisms will be discussed later in detail.

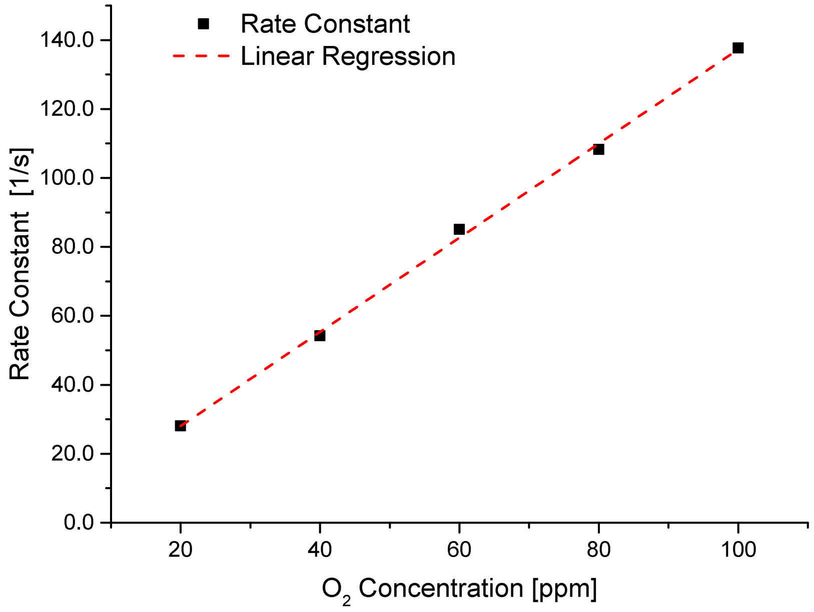

Figure 4.4: *Rate constant k_1 for the first reaction step as a function of the oxygen concentration within the helium buffer gas. The dashed redline represents a linear regression.*

For a simple association reaction as described in Equation 4.10 the decay of the initial bare cluster scales linearly with the oxygen concentration in the buffer gas. By variation of the concentration the proposed reaction mechanism can be verified. The implemented gas reservoir enables dilution of the commercial oxygen helium gas mixture. For this purpose, the reactive gas is filled into the installed gas reservoir. Then helium (6.0, Westfalen) is added into the gas reservoir. Oxygen concentrations of 20, 40, 60 and 80 ppm are prepared. Figure 4.4 illustrates the calculated order rate constants of the first reaction step k_1. The rate constant increases linearly with the oxygen concentration in the buffer gas. This observation is a clear indication that for each reaction step only one oxygen molecule is involved and, therefore, supports the proposed reaction mechanism.

4.3.2 Reaction at 50 K

Figure 4.5 a) illustrates mass spectra for a reaction time of 10 ms. Already after such a short reaction time, the bare Ta_{20}^+ cluster is not the dominant species anymore. Instead the most abundant species is $Ta_{20}O_2^+$. Only peaks with an even number of oxygen atoms are caused by the reaction with molecular oxygen. All other peaks result from side reactions with the background gas. Additionally detected reaction products are $Ta_{20}O_4^+$, $Ta_{20}O_6^+$ and $Ta_{20}O_8^+$. After a reaction time of 50 ms c) again a broad distribution of reaction products from $Ta_{20}O_4^+$ to $Ta_{20}O_{22}^+$ is detected with $Ta_{20}O_{16}^+$ being the most prominent species. In contrast to the reaction at 300 K, $Ta_{20}O_{26}^+$ is not the final reaction product. After a reaction time of 100 ms, the largest detected oxide species is $Ta_{20}O_{32}^+$. From the studies of Duncan and co-

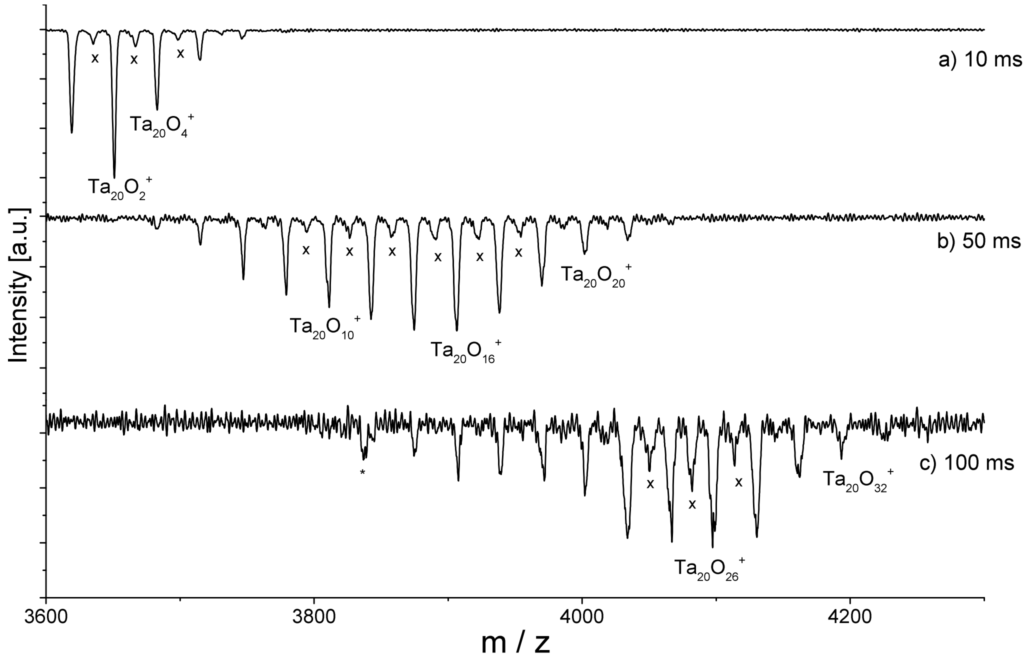

Figure 4.5: *Mass spectra for the reaction of Ta_{20}^+ with molecular oxygen recorded at reaction times of a) 10 ms, b) 50 ms, c) 100 ms. Peaks marked with + are due to a side reaction with water background, * mark peaks due to a side reaction that results in the fragmentation of the tantalum cluster. Both reaction channels are not discussed due to their low intensities.*

workers it is known that tantalum clusters can become over saturated with oxygen atoms [127]. As those species only appear at temperatures below 75 K, there is a strong indication that the surplus oxygen molecules are only loosely bound to the cluster, as for example by van-der-Waals interaction. Similar effects have been found for silver dimers [65] or palladium clusters [142].

The calculated rate constants are shown as a function of the reaction step in Figure 4.6. In general, the determined pseudo-first order rate constants at 50 K are lower than those obtained at 300 K. An exception is the rate constant of the last two reaction step which is significantly higher at 50 K. Similar to the reaction at 300 K, two reaction regimes are observed. In each regime the pseudo-first order rate constant decreases linearly. The transition between the two regimes takes place at the seventh reaction step.

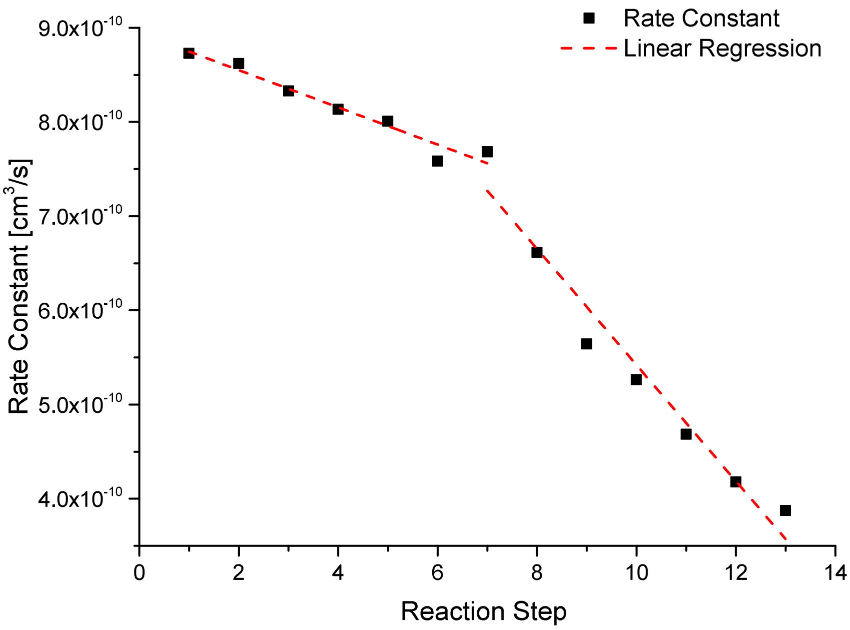

Figure 4.6: *Pseudo first order rate constants for all of reaction steps at 50 K. The dashed lines represent a linear regression for reaction steps 1-7 and 7-13 respectively.*

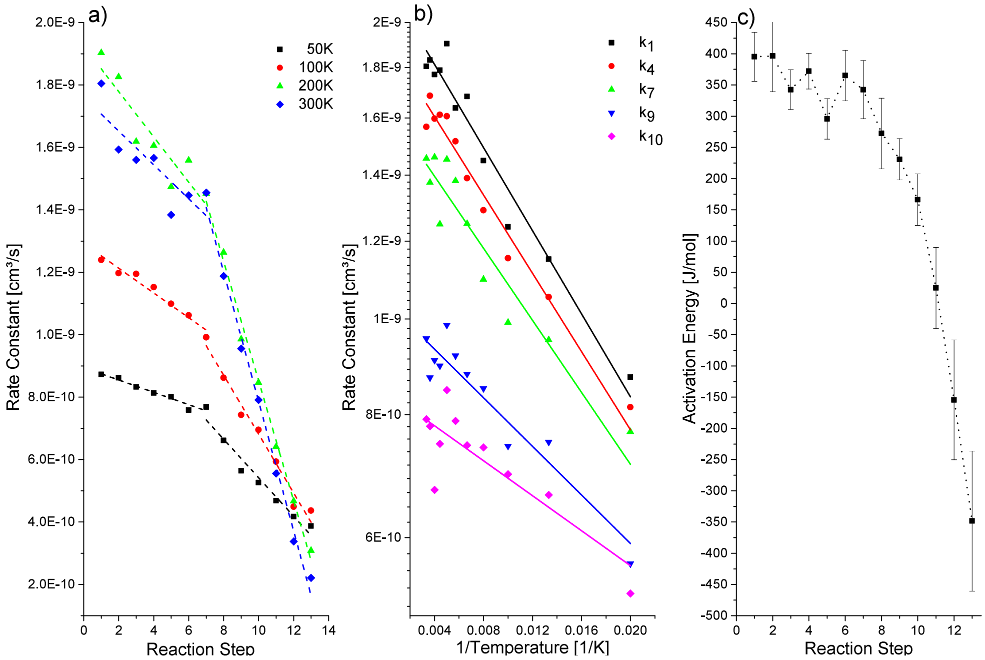

Figure 4.7: *a) Rate Constants as a function of the reaction step for 50 K, 100 K, 200 K and 300 K. b) Arrhenius plots for reaction steps 1, 4, 7, 9 and 10 and c) corresponding activation energy for all reaction steps.*

4.3.3 Arrhenius plot and activation Energies

Figure 4.7 a) illustrates rate constants determined for temperatures of 50 K, 100 K, 200 K and 300 K for each reaction step. For all temperatures two regimes can be seen. Within each regime the rate constant depends linearly on the reaction step, with the transition taking place at the seventh reaction step ($\mathrm{Ta}_{20}\mathrm{O}_{12}^{+} \xrightarrow{k7} \mathrm{Ta}_{20}\mathrm{O}_{14}^{+}$). The dashed lines in the Figure represent a linear regression. In general, the fitted slopes of the linear regressions increase with temperature. Although the variation for the first regime is minor, the effect on the second regime is much more pronounced. In fact, for the last two reaction steps, higher pseudo-first order rate constants are determined for lower temperatures. For unimolecular reactions, the rate constants should satisfy the Arrhenius Equation [1]:

$$k = A \cdot e^{-\frac{E_A}{R \cdot T}}, \tag{4.11}$$

where A is the prefactor that includes in this case the so called steric factor, the activation energy E_A and R the gas constant.

Figure 4.7 b) depicts an Arrhenius plot for reaction steps 1, 4, 7, 9 and 10. The solid lines represent a linear regression of the rate constant versus the inverse temperature. While reaction steps 1 to 11 fulfill Equation 4.11, this is not the case for the last two reaction steps 12 and 13. For both steps the corresponding rate constant increases with decreasing temperature. From the slope of the linear regression, however, the activation energy can be obtained. The calculated activation energy for all reaction steps is shown in Figure 4.7 c). The first reaction step has a very low activation energy of roughly 400 J/mol, for all of the consecutive reaction steps the activation energy is even lower. The error bars shown in Figure 4.7 c) only represent the error of the Arrhenius fit, the absolute error is expected to be much larger. The activation energy determined for the first reaction step is roughly one order of magnitude lower compared to the activation energy found for the reaction of $Ag_2^+ \xrightarrow{+O_2} Ag_2O_2^+$ [65]. For the first seven reaction steps the activation energy decreases only slightly. Surprisingly, after the seventh reaction step, the activation energy decreases much faster. The simultaneous decrease of rate constants and activation energies in the second reaction regime strongly indicates a change in the reaction mechanism, which will be discussed further on.

4.3.4 Discussion

For the reaction of molecular oxygen with Ta_{20}^+ four major effects have been observed:

1. Tantalum clusters stay intact upon oxidation.
2. Two different reaction regimes (reaction steps 1-7 and 8-13, respectively) have been found.
3. The reaction rate decreases with each additional oxygen molecule adsorbed.
4. The activation energy stays constant within the first regime and drops quickly within the second one.

For the first regime (1-7), the reaction rate decreases only slightly with each reaction step. The calculated pseudo-first order rate constants increase with increasing reaction temperature. The obtained activation energies, thus, are very small but different from zero. Although a slight trend towards smaller activation energies is found for each further reaction step, the activation energy remains almost constant within the first reaction regime. To explain these finding a modified Lindemann model is proposed:

$$Ta_{20}O_m^+ \xrightarrow{k_a} Ta_{20}O_mO_2^{+*} \xrightarrow{k_d} Ta_{20}O_m(O,O)^{+*} \xrightarrow{k_s} Ta_{20}O_m(O,O)^+ \tag{4.12}$$

Analogous to the Lindemann model, tantalum cluster(oxides) $\mathrm{Ta_{20}O_m^+}$ collide with oxygen molecules and an activated complex $Ta_{20}O_mO_2^{+*}$ is formed. The newly attached oxygen molecule quickly dissociates, rendering any backward reaction to the educts highly improbable. As k_b is suppressed, a small but finite activation energy is observed. It is known for smaller tantalum clusters ($\mathrm{Ta_6^+}$-$\mathrm{Ta_8^+}$) that at least the first two oxygen molecules do not bind as intact molecules to the clusters, but instead dissociate [127], with each oxygen atom forms bonds to two tantalum atoms [138]. Similar observations were made in the case of small palladium clusters [142]. The stabilization step k_s can either be caused by collisions with helium atoms or by internal redistribution of the excess energy. The latter may be important due to the high number of degrees of freedom of the $\mathrm{Ta_{20}^+}$ cluster (and its oxides). Hence life-time of the activated complex may be high enough to be stabilized by collisions with buffer gas atoms in almost any case.

For the second reaction regime (reaction steps 8-13) lower reaction rates and lower activation energies are found. One would intuitively expect the opposite: the reaction rate should increase with decreasing activation energies. This finding indicates that a different oxidation process takes place in the second regime. Additionally, compared to the first regime, a much faster decrease of reaction rates and activation energies was determined. These observations can be explained by an intact adsorption of oxygen molecules onto the cluster. Therefore, a 'classic' Lindemann model is assumed:

$$Ta_{20}O_m^+ \xrightarrow{k_a} Ta_{20}O_mO_2^{+*} \tag{4.13}$$

$$a) \quad Ta_{20}O_mO_2^{+*} \xrightarrow{k_b} Ta_{20}O_m^+ + O_2 \tag{4.14}$$

$$b) \quad Ta_{20}O_mO_2^{+*} \xrightarrow{k_s} Ta_{20}O_{m+2}^+ \tag{4.15}$$

Oxygen acts as an electron acceptor [29] when reacting with gold clusters. Assuming a similar mechanism for the tantalum clusters, each attached oxygen atom would further deplete the electron density of the tantalum cluster. After the uptake of several oxygen molecules the electron density may be too low to effectively enable the dissociation of a further oxygen molecule. The dissociation may be either completely suppressed or is at least comparably slow. Thus, the back reaction k_b has a significant influence for the second reaction regime. Two competing reaction pathways are accessible, either stabilization k_s to form $Ta_{20}O^+_{m+2}$ or the back reaction to $Ta_{20}O^+_m$ and O_2. The apparent overall rate constant k_{app} for the reaction $Ta_{20}O^+_m \rightarrow Ta_{20}O^+_{m+2}$ decreases. Assuming that k_a and k_s do not strongly depend on the temperature [63], the apparent rate constant k_{app} of the overall reaction increases with decreasing temperature. Indeed, such a behavior is found for the last two reaction steps ($Ta_{20}O^+_{22} \rightarrow Ta_{20}O^+_{24} \rightarrow Ta_{20}O^+_{26}$). Formally an increase of the rate constant for lower temperatures implies a negative activation energy. For reaction steps 8 to 11, however, positive activation energies are found, only the last two reaction steps feature negative activation energies. In summary, the observed effects can be explained by the existence of the two competing reaction pathways. The dissociation of the oxygen atoms, expressed by the rate constant k_d, dominates within the first reaction regime, resulting in positive, almost constant activation energies. For the second reaction regime the back reaction becomes more and more important, the apparent activation energies rapidly decrease with each reaction step.

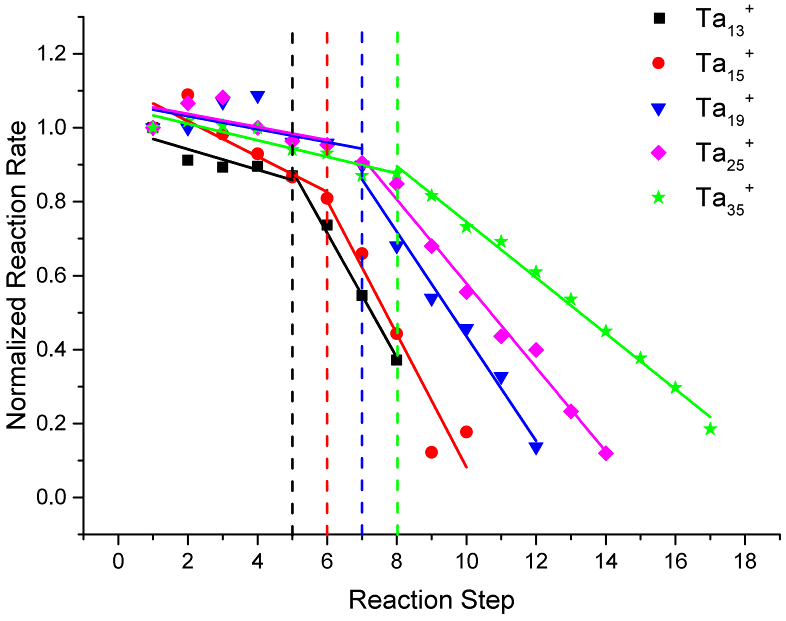

Figure 4.8: *Rate constants for the oxidation of Ta_{13}^+, Ta_{15}^+, Ta_{25}^+ and Ta_{35}^+. All of the rate constants are normalized to the first reaction step. For all cluster sizes two reaction regimes are found and the transition reaction step increases with cluster size. Dashed lines represent a linear regression of the rate constants for both reaction regimes.*

Besides Ta_{20}^{+}, further larger clusters with 15 to 40 tantalum atoms have been investigated. The calculated rate constants are depicted in Figure 4.8. For each cluster size, the rate constant is normalized to the first reaction step. For all investigated cluster sizes again the two regimes are found. The transition between the two regimes takes place at step 5 for Ta_{13}^{+}, 6 for Ta_{15}^{+}, 7 for Ta_{25}^{+} and 8 for Ta_{35}^{+}.

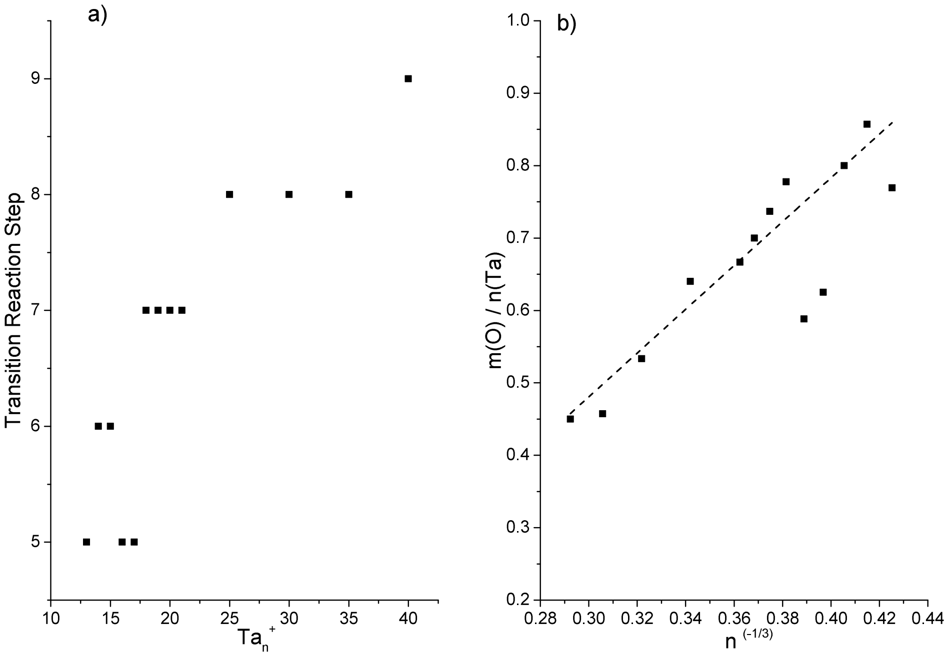

Figure 4.9: *a) Transition reaction step as a function of the cluster size. b) Ratio of adsorbed oxygen atoms (m) and the number of tantalum atoms (n) within the cluster at the transition reaction step as a function of* $n^{-\frac{1}{3}}$*, which approximates the surface to volume ratio. The linear trend indicates a surface adsorption of oxygen in the first reaction regime.*

Figure 4.9 a) illustrates the transition reaction step for all investigated cluster sizes as a function of cluster size. Except Ta_{16}^{+} and Ta_{17}^{+}, the transition between the two regimes takes place at later reaction steps with increasing cluster size. In general, more oxygen atoms can be bound on larger clusters. The amount of oxygen reacted in the first regime could also be related to the cluster surface. Expanding on this idea, the ratio of surface and volume is proportional to $n^{-\frac{1}{3}}$. As shown in Figure 4.9 b), the ratio between oxygen atoms m (corresponding to the transition intermediate) and the number of tantalum atoms n scales linearly with $n^{-\frac{1}{3}}$. These findings indicate that the oxygen molecules adsorbed in the first reaction regime are bound to the surface of the cluster. The moderate decrease of the reaction rate during the first regime can be simply explained by a successive blocking of adsorption sites. Consequently, the steric factor changes, resulting in a slower reaction.

4.4 Degradation of smaller tantalum clusters ($Ta^+_{4\text{-}8}$)

The reaction of molecular oxygen with free cationic tantalum clusters composed of 8 atoms or fewer is discussed in this chapter. These smaller clusters demonstrate a drastically different reaction behavior. In contrast to larger clusters, smaller clusters fragment upon reaction with oxygen. In the following, reaction pathways are shown and related properties of the clusters are discussed.

While for larger clusters the relative difference in mass is rather small, strong fragmentation of smaller clusters (i.e. the loss of several tantalum atoms) results in the formation of products over a vast mass range (in the case of Ta_8^+ from almost 1'500 u to less then 500 u). This is an additional challenge as it is necessary to record mass spectra at different delays between ion extraction from the ring electrode ion trap and pulsing of the acceleration stage of the reflectron time-of-flight mass-spectrometer.

4.4.1 Influence of the delay between ion extraction and mass analysis

A mass spectrum of the reaction of Ta_8^+ cluster with molecular oxygen measured after a reaction time of 50 ms and reaction temperature of 300 K is illustrated in Figure 4.10 a). The delay between ion extraction and pulsing of the acceleration stage of the reflectron time-of-flight mass spectrometer is set to 420 µs. Next to Ta_8^+ two other peaks that can be assigned to Ta_7O^+ and $Ta_6O_2^+$ appear in the spectrum. In fact, the latter ones are the most prominent peaks. A detailed account of the reaction channels is given in the next chapter. The distribution of the reaction products, however, depend on the delay t_D. At a delay of 380 µs, $Ta_6O_2^+$ is the dominant species. At a delay of 330 µs further fragmentation products: $Ta_4O_4^+$, $Ta_3O_5^+$ and $Ta_2O_6^+$ appear.

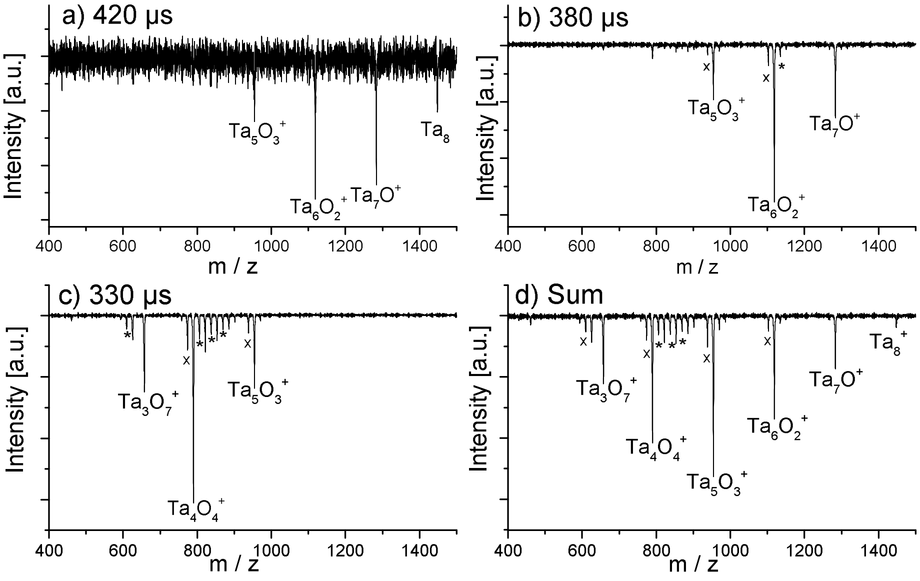

Figure 4.10: *Mass spectra for the reaction of* Ta_8^+ *with molecular oxygen at 300 K and a reaction time of 50 ms. Detected reaction products depend on the delay* t_D *between ion extraction out of the trap and pulsing of the acceleration plates of the reflectron time-of-flight mass spectrometer. Low intensity peaks marked with a cross are the result of the ejection of a tantalum atom from the cluster upon reaction with oxygen. Peaks marked with an asterisk are resultant from a side reaction with water. d) Sum of the mass spectra recorded after delays of 300, 330, 350, 380, 410, 420, 430 and 450 µs.*

This phenomenon is caused by the ejection of ions out the ring electrode ion trap as this process resembles the acceleration in a single-stage time-of-flight mass spectrometer. Thus, lighter ions arrive earlier at the acceleration stage of the reflectron time-of-flight mass spectrometer. During ion extraction, all ions are accelerated to the same kinetic energy. Lighter ions are significantly faster and arrive earlier at the acceleration stage of the mass spectrometer. Consequently, these ions can be detected at smaller delays. Due to the comparably high mass ratio of the formed reaction products ($m(Ta_8^+)/m(Ta_2O_6^+) \approx 3$ [1]), the distribution of the detected reaction products becomes a function of t_D. This effect can be mitigated by choosing a different extraction fields, at the expense of losing overall sensitivity. A better method with higher sensitivity is to measure at several different delays t_D and sum over the obtained mass spectra. Species with different masses which appear at different delays t_D are evenly detected with highest sensitivity. For kinetic measurements only the relative change of the reactants and products is of importance and not their

---

[1] compare to $(m(Ta_{20}O_{26}^+)/m(Ta_{20}^+)) \approx 1.1$ for the oxidation of Ta_{20}^+

absolute abundance. In order to achieve an equal detection of all species, delays of 300, 330, 350, 380, 420, 430 and 450 µs are chosen. Figure 4.10 d) represents the sum of the mass spectra obtained for these delays which demonstrates that a mass range of less than 600 u to almost 1'500 u can be covered by the use of seven different delays.

4.4.2 Reaction of Ta_8^+ with oxygen

In this experiment, Ta_8^+ is mass-selected and reacted with oxygen while being stored in the ring electrode ion trap at a temperature of 300 K.

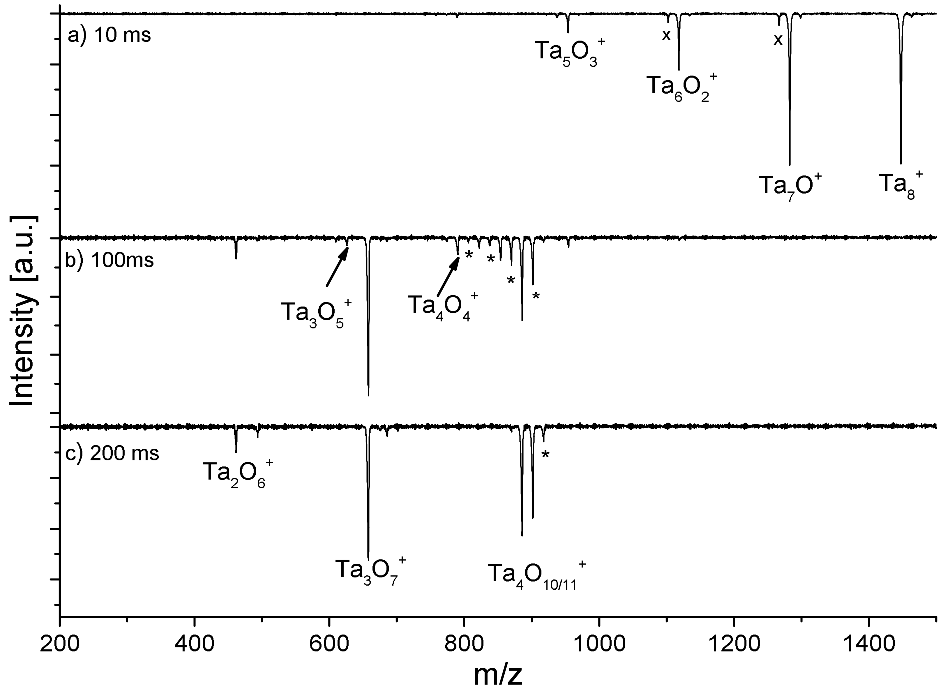

Figure 4.11: *Sum of the mass spectra of the reaction of Ta_8^+ with oxygen at delays of 300, 330, 350, 380, 420, 430 and 450 µs for reaction times of a) 10 ms, b) 100 ms, and c) 200 ms. The reaction progresses in consecutive oxidative degradation steps: The tantalum oxide clusters take up O_2 and ejects TaO. Low intensity peaks marked with a cross correspond to the ejection of a tantalum atom from the cluster. Peaks marked with an asterisk are the result of a side reaction with water.*

Figure 4.11 a) illustrates the sum of the measured mass spectra for a reaction time of 10 ms. Almost equal amounts of Ta_8^+ and Ta_7O^+ are detected. Further reaction products are $Ta_6O_2^+$ and $Ta_5O_3^+$. For longer reaction times of b) 100 ms and c) 200 ms additional $Ta_4O_4^+$, $Ta_3O_5^+$ and $Ta_2O_6^+$ are found. These findings can be modeled by consecutive reaction steps. Molecular oxygen attaches on Ta_8^+ and an activated complex $Ta_8O_2^{+*}$ is formed. Analogous to the reaction pathway found for Ta_{20}^+, the oxygen molecule dissociates quickly. In contrast to Ta_{20}^+, smaller clusters like Ta_8^+ cannot be stabilized fast enough due to their lower heat capacity. The formed complex instead relaxes most likely by the ejection of a neutral TaO fragment, rather than by the loss of individual tantalum and oxygen atoms. Similar effects have been found for the reaction of cationic vanadium clusters with oxygen [149], cobalt with methanol [150] or anionic aluminum clusters with ammonia [151]. A Scheme of the reaction of Ta_8^+ with molecular oxygen can be written as:

$$Ta_8^+ \xrightarrow{k_{F8}} Ta_7O^+ \xrightarrow{k_{F7}} Ta_6O_2^+ \xrightarrow{k_{F6}} Ta_5O_3^+ \xrightarrow{k_{F5}} Ta_4O_4^+. \tag{4.16}$$

None of the intermediate species formed is able to take up additional oxygen molecules and remain intact. At $Ta_4O_4^+$ the reaction pathway divides into two parallel reaction pathways. Remarkably, half of the clusters stay intact and successively take up oxygen. This behavior is analog to the reaction pathway found for Ta_{20}^+. The final species is $Ta_4O_{10}^+$.

$$Ta_4O_4^+ \xrightarrow{k_{F4}} Ta_3O_5^+ \tag{4.17a}$$

$$Ta_4O_4^+ \xrightarrow{k_{A4-1}} Ta_4O_6^+ \xrightarrow{k_{A4-2}} Ta_4O_8^+ \xrightarrow{k_{A4-3}} Ta_4O_{10}^+ \tag{4.17b}$$

The remainder of $Ta_4O_4^+$ undergoes further degradation and forms $Ta_3O_5^+$. Again two parallel reactions are possible. While a small fraction degrades further to $Ta_2O_6^+$, the main reaction pathway is the formation of $Ta_3O_7^+$.

$$Ta_3O_5^+ \xrightarrow{k_{F3}} Ta_2O_6^+ \tag{4.18a}$$

$$Ta_3O_5^+ \xrightarrow{k_{A3-1}} Ta_3O_7^+ \tag{4.18b}$$

The final species of the reaction of Ta_8^+ with molecular oxygen are therefore: $Ta_4O_{10}^+$, $Ta_3O_7^+$ and $Ta_2O_6^+$.

Additionally minor peaks in the spectrum are caused by two side reactions. Species that are the result of the ejection of a Ta or TaO_2 fragment are marked by a cross in Figure 4.11. The corresponding reaction Scheme may be written as:

$$Ta_nO_m \rightarrow Ta_{n-1}O_m + Ta + O_2 \tag{4.19a}$$

$$Ta_nO_m \rightarrow Ta_{n-1}O_m + TaO_2. \tag{4.19b}$$

The second side reaction occurs with residual water molecules and the associated species are marked with an asterisk. Since these side reactions do not significantly interfere with the main reaction Scheme, they will be excluded from further discussion. The surprisingly high intensity of $Ta_4O_{11}^+$, however, cannot be explained by a side reaction with water. Most likely, it is the result of a reaction of $Ta_4O_{10}^+$ with molecular oxygen.

The reaction of Ta_8^+ with molecular oxygen can now be fitted according to these schemes. The results of the fit are shown in Figure 4.12 as solid lines. Again a very good agreement between the experimental data and the result of the kinetic fit is obtained.

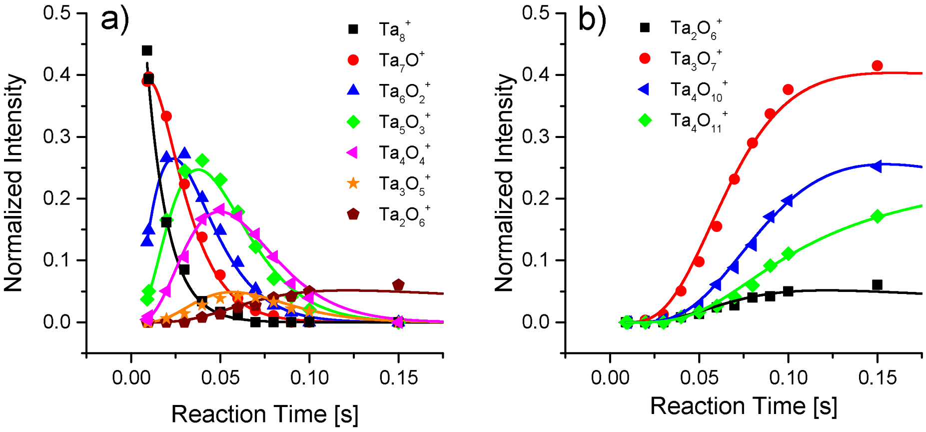

Figure 4.12: *Selected reactants intensities as a function of the reaction time. The result of the kinetic fit is depicted as solid lines. Products of the initial degradation pathway 4.16, 4.17a and 4.18a are shown in a), whereas b) depicts the formation of the final species according to Schemes4.17b and 4.18b.*

Figure 4.13 a) shows the calculated pseudo-first order rate constants for the fragmentation reaction steps described by Schemes 4.16, 4.17a and 4.18a. k_{F8} to k_{F5}, which correspond to the first four degradation steps, are similar to the rate constants found for the oxidation of Ta_{20}^{+}. A strong decrease of the rate constants for the last two degradation steps $Ta_4O_4^+ \rightarrow Ta_3O_5^+$ and $Ta_3O_5^+ \rightarrow Ta_2O_6^+$ is found. Simultaneously, a second reaction channel opens up, as $Ta_4O_4^+$ and $Ta_3O_5^+$ can remain intact upon oxidation. Strikingly, the over all reactivity almost remains constant. From

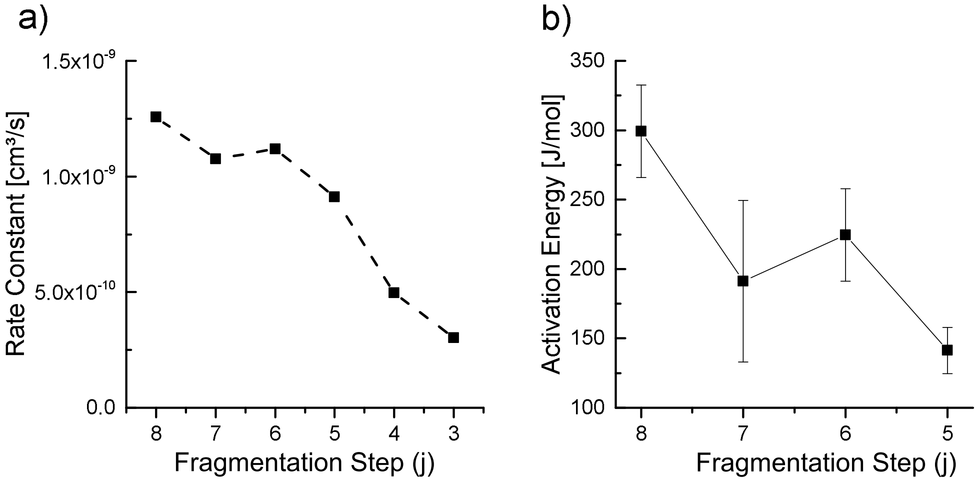

Figure 4.13: *Pseudo-first order rate constants k_{Fj} a) and b) corresponding activation energies for the fragmentation pathway of the reaction of Ta_8^+ with oxygen.*

the determined rate constants the branching ratios for $Ta_4O_4^+$ ($\frac{k_{A4-1}}{k_{F3}+k_{A4-1}} \approx 0.45$) and $Ta_3O_5^+$ ($\frac{k_{A3-1}}{k_{F3}+k_{A3-1}} \approx 0.90$) can be calculated. The activation energies for the first four fragmentation steps are depicted in Figure 4.13 b). For the remaining fragmentation steps no activation could be determined. The activation energy for k_{F8} is again very small but significantly higher compared to the other fragmentation steps. This observation may indicate an activation of the these species by the reaction with oxygen.

4.4.3 Reaction of Ta_6^+ and Ta_7^+ with oxygen

The same experiment was repeated for Ta_6^+ and Ta_7^+. Mass spectra for the oxidation of Ta_7^+ for a reaction time of 10 ms are depicted in Figure 4.14 a). Ta_7^+ is the most

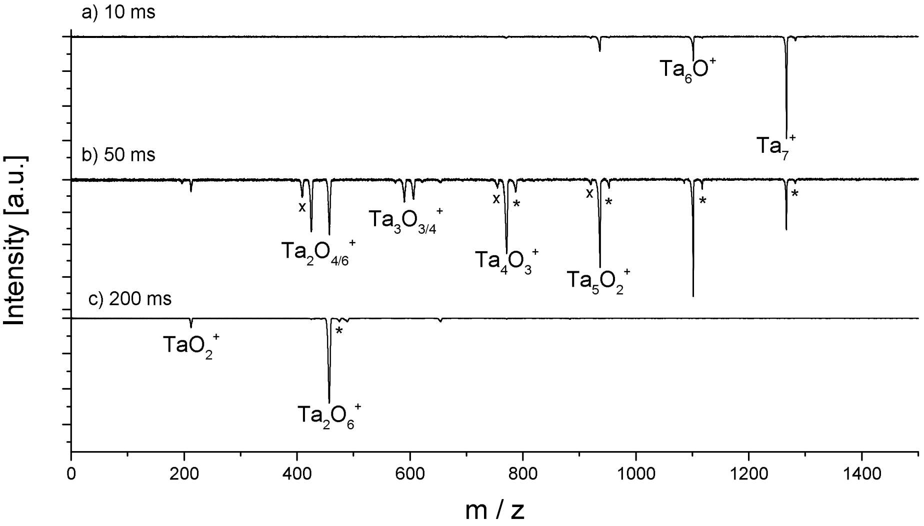

Figure 4.14: *Sum of the mass spectra for the oxidation Ta_7^+ at delays of 220, 280, 330 and 380 μs for reaction times of a) 10 ms, b) 50 ms, and c) 200 ms. The clusters undergo oxidative degradation by consecuitvely reacting with O_2 and ejecting (Ta,O). Byproducts are caused by the ejection of a tantalum atom and the reaction with residual water and are markend by a cross and an asterisk, respectively. Both reaction channels can be neglected due to their low abundance.*

abundant species, although a significant amount of Ta_6O^+ is detected. Similar to Ta_8^+, the degradation of the tantalum cluster progresses rapidly. For a reaction time of 50 ms (b)), the most prominent peak in the spectrum can be correlated to $Ta_5O_2^+$. Additional intermediates of the fragmentation pathway such as $Ta_4O_3^+$ appear in the spectrum. The reaction Scheme of Ta_7^+ demonstrates some notable differences compared to the one of Ta_8^+. In contrast to $Ta_4O_4^+$, which is formed by the oxidative degradation of Ta_8^+, $Ta_4O_3^+$ is seemingly unable to remain intact upon reaction with oxygen. Instead it undergoes further fragmentation resulting in the formation of $Ta_3O_3^+$ and $Ta_3O_4^+$, thus deviating from the reaction scheme. Further reactions products include $Ta_2O_4^+$ and $Ta_2O_6^+$. A small fraction of the formed $Ta_3O_x^+$ species remain intact and form $Ta_3O_7^+$. For reaction times longer than 200 ms, $Ta_2O_4^+$ can no longer be detected. The main sink of the reaction is $Ta_2O_6^+$. Furthermore, a low intensity peak corresponding to TaO_2^+ appears. It should be noted that for

Ta_3^+- and Ta_2^+ species the fragmentation does not strictly follow the Scheme 4.16. $Ta_3O_3^+$ seems to be the preferential structure compared to $Ta_3O_4^+$. Moreover, TaO_2^+ is a common structure found for the reaction of tantalum atoms with oxygen [152]. Species like TaO_4^+ only form under specialized conditions [153]. The reaction of Ta_6^+ with oxygen was also studied and proceeds in similar manner. The main sinks of the reaction are again $Ta_2O_6^+$ and TaO_2^+.

4.4.4 Reaction of Ta_4^+ and Ta_5^+ with oxygen

Due to the inherent cluster size distribution generated by the cluster source, Ta_4^+ is the smallest nascent cluster that is guided into the ion trap at a sufficient intensity. The study of Ta_4^+ is therefore of particular interest. Figure 4.15 a) depicts the mass spectrum measured for the reaction of Ta_4^+ with molecular oxygen after a reaction time of 10 ms. Equal amounts of Ta_4^+, Ta_3O^+ and $Ta_2O_2^+$ are detected. These findings imply that the reaction of Ta_4^+ with oxygen follows the same Scheme as Ta_7^+. A side reaction with water results in the formation of $Ta_2O_3^+$, which is marked

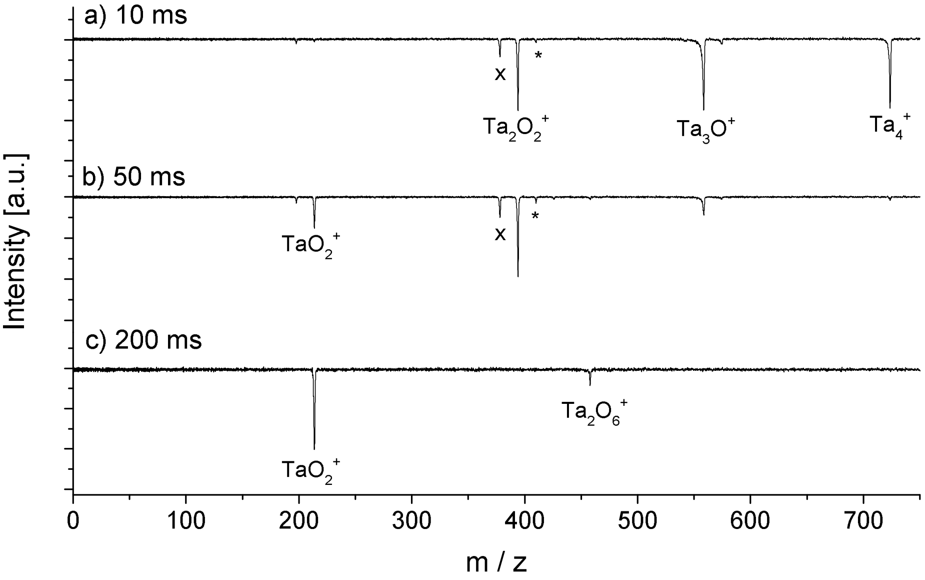

Figure 4.15: *Mass Spectra for the oxidation Ta_4^+ for reaction times of a) 10 ms, b) 50 ms, and c) 200 ms. The clusters undergo oxidative degradation by consecuitvely reacting with O_2 and ejecting (Ta,O). Byproducts are caused by the ejection of a tantalum atom and the reaction with residual water and are markend by a cross and an asterisk, respectively. Both reaction channels can be neglected due to their low abundance.*

with an asterisk. The second side reaction is again the straightforward degradation of Ta_3O^+ to Ta_2O^+. For reaction times longer than 50 ms, Ta_4^+ can no longer be detected. At the same time an additional reaction product, TaO_2^+, appears. In contrast to $Ta_2O_4^+$, which was formed as an intermediate during the the reaction of Ta_7^+ with oxygen, only a minor fraction of $Ta_2O_2^+$ is stabilized and eventually forms $Ta_2O_6^+$. The major fraction undergoes further fragmentation and forms TaO_2^+. A similar reaction scheme is found for the reaction of Ta_5^+ with oxygen.

4.4.5 Discussion

The major effects observed in the reaction of small cationic tantalum clusters with eight atoms or fewer may be summarized as follows:

1. Small tantalum clusters degrade upon reacting with molecular oxygen by the ejection of a TaO fragment.
2. There are two reaction channels for certain intermediates such as $Ta_4O_4^+$, namely further oxidative degradation or oxidation of the intact cluster. The subsequent adsorption of oxygen on the intact cluster stops at a specific oxide.
3. The initial cluster size determines the final species.
4. Rate constants for the degradation pathway are similar to the oxidation of Ta_{20}^+.

In order to analyze these effects, a closer look at the size-dependent reaction pathways is taken. An overview of the identified pathways in the reaction of Ta_8^+, Ta_7^+ and Ta_4^+ with oxygen is provided in Figure 4.16. The first reaction steps of Ta_8^+ and Ta_7^+ involve degradation of the tantalum clusters. In fact, both reactions proceed identically until the intermediate species $Ta_4O_4^+$ or $Ta_4O_3^+$ are formed. In the case of $Ta_4O_4^+$ about 45% remain intact and eventually form $Ta_4O_{10}^+$, 55% fragment to $Ta_3O_5^+$. Again two parallel reactions are possible. 90% of $Ta_3O_5^+$ form $Ta_3O_7^+$, whereas 10% undergo a further fragmentation step to $Ta_2O_6^+$. In the case of $Ta_4O_3^+$, only fragmentation is observed. For $Ta_4O_5^+$, which is formed as an intermediate species during the reaction of Ta_9^+ with oxygen, only oxidation of the intact cluster occurs. A similar effect was found for the reaction of vanadium (-oxide) clusters with oxygen [149]. The complete reaction Scheme of Ta_9^+ with oxygen is more complex

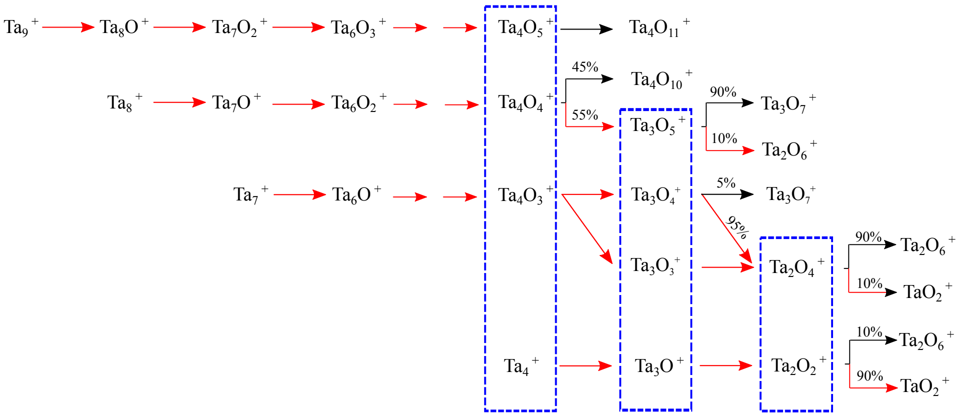

Figure 4.16: *Reaction Scheme for the reaction of molecular oxygen with Ta_9^+, Ta_8^+, Ta_7^+ and Ta_4^+. Degradation reaction steps are shown as red arrows, oxidation of the intact cluster as black arrows. The reaction Scheme of Ta_6^+ is similar to Ta_7^+ and that of Ta_5^+ to Ta_4^+. Branching ratios are calculated from the determined rate constants. The more complex reaction Scheme of Ta_9^+ will be discussed in the next chapter in detail.*

than the simplified scheme shown in Figure 4.16. It will be discussed in the next chapter in more detail. Similar changes of the branching ratios are not only found for $Ta_4O_m^+$ but also for $Ta_3O_m^+$ and $Ta_2O_m^+$ species. Approximately 90% of $Ta_3O_5^+$ form $Ta_3O_7^+$, whereas for $Ta_3O_4^+$ only the degradation pathway is open. Furthermore, only 10% of $Ta_2O_4^+$ fragment, yet 90% of $Ta_2O_2^+$ react to TaO_2^+.

There are, in principle, three interrelated properties that may account for the different pathways observed for the reaction of $Ta_4O_3^+$, $Ta_4O_4^+$ and $Ta_4O_5^+$ with molecular oxygen. The first possibility is a change of the heat capacity of the cluster. The increased number of atoms in $Ta_4O_5^+$ compared to $Ta_4O_3^+$ translates to more degrees of freedom. Thus $Ta_4O_5^+$ has a higher heat capacity. Analogous to Ta_{20}^+, oxygen dissociates upon reacting with $Ta_4O_m^+$ and an activated complex is formed.

$$Ta_4O_m + O_2 \rightarrow Ta_4O_m(OO)^{+*} \tag{4.20}$$

The excess heat from this process is then released into the cluster, resulting in a hot cluster. Due to the higher heat capacity, $Ta_4O_5^+$ can be efficiently stabilized by collisions with the helium buffer gas, while $Ta_4O_3^+$ relaxes by the ejection of TaO fragment. For $Ta_4O_4^+$ stabilization is only successful in 45% of all cases. $Ta_4O_4^+$ is formed by a consecutive oxidative degradation of Ta_8^+. Since TaO fragment is ejected for each reaction step, the total number of atoms composed in the cluster remains constant. For Ta_7O^+ and $Ta_6O_2^+$ each oxygen atom is likely bound to two tantalum atoms [138]. In a simple model, the heat capacity of the cluster of the cluster also stay approximately constant. For a more detailed discussion the exact structures of $Ta_5O_3^+$, $Ta_4O_4^+$ and $Ta_3O_5^+$ have to be determined.

Another possibility to explain the different reaction behavior of the clusters can be explained by an adsorption if intact oxygen molecules for species like $Ta_4O_5^+$. For Ta_{20}^+ it was found that only the first seven oxygen molecules are bound dissociatevly. Oxygen molecules attached in later reaction remain intact. This phenomenon was attributed to the reduced electron density on the surface on the cluster. Similarly the electron density of $Ta_4O_5^+$ can be insufficient for an efficient dissociation of oxygen molecules. As a consequence, the energy released into the cluster would be drastically reduced, and the cluster may remain intact.

To elucidate the structure of $Ta_4O_{10}^+$, infrared multiple photon dissociation spectroscopy has been applied [154]. It has been found that the recorded spectra are similar to those obtained for $Nb_4O_{10}^+$ [155], indicating similar structures.

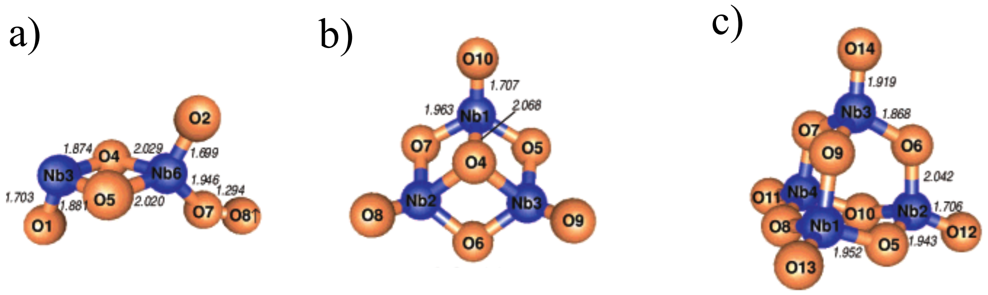

Figure 4.17: *Lowest energy isomers of a) $Nb_2O_6^+$, b) $Nb_3O_7^+$ and c) $Nb_4O_{10}^+$. Binding lengths are given in Å. Adapted with permission from [155]. Copyright 2003 American Chemical Society.*

Figure 4.17 illustrates the lowest energy isomers of $Nb_2O_6^+$, $Nb_3O_7^+$ and $Nb_4O_{10}^+$. For the latter cluster, each niobium atom is bound to three oxygen atoms in bridging positions, and an additional oxygen atom in a terminal position. However, no indications of an intact oxygen molecule have been found [155]. Analogous structures have been reported for $Ta_3O_6^+$ [156] and $Ta_3O_8^+$ and Ta_2O_6 [154][157]. Thus it seems likely that oxygen binds dissociatevly to $Ta_4O_3^+$ as well as to $Ta_4O_5^+$. The first species that contains an intact oxygen molecule is $Ta_4O_{11}^+$ [154]. This species has been detected for the reaction of Ta_8^+ with molecular oxygen in surprisingly high amounts. In fact, its high abundance renders the formation due to a side reaction with water very unlikely. It seems more reasonable that an oxygen atom bound in a terminal position is replaced by an oxygen molecule. At temperatures lower than 250 K, this process is promoted further and $Ta_4O_{12}^+$ is formed eventually.

The third possibility to explain the different reaction pathways found for $Ta_4O_3^+$, $Ta_4O_4^+$ and $Ta_4O_5^+$ is the stabilization of the cluster by the incorporation of oxygen into the cluster structure. Du found an average binding energy of about 4.2 eV per atom for Ta_4^+ [140], whereas Ta-O bonds feature significant higher binding strengths [158]. For small cationic tantalum clusters, it has been found that oxygen is bound in bridging position to two tantalum atoms [138]. Assuming a similar binding mechanism for additional attached oxygen atom each tantalum atom can be bound to upto three oxygen atoms. In the case of Ta_4^+ a total of six oxygen atoms can be incorporated into the cluster by this mechanism. It should be noted that at this point formally no Ta-Ta bond exists anymore. In fact, a stabilized Ta-O 'core' is formed. The same effect was found for the neutral dimer [157] and the cationic [154] and anionic trimer [139]. Each additionally attached oxygen atom is bound in terminal position.

While to the best knowledge of the author no structure of $Ta_4O_3^+$, $Ta_4O_4^+$ or $Ta_4O_5^+$ can be found in literature, it seems reasonable to assume that the oxygen atoms are bound in the bridging position for these clusters. After the reaction of $Ta_4O_5^+$ with oxygen seven oxygen atoms are adsorbed on the cluster. Hence, the described 'Ta-O core' can be formed, resulting in a stabilized cluster. In the case $Ta_4O_3^+$ this is not possible, for $Ta_4O_4^+$ the formation of the stabilized core may only be possible in 45 % of the cases. Two isomers may exist, one is stabilized and therefore remains intact upon reacting with oxygen, the other one degrades. Nonetheless, this simple explanation fails for $Ta_3O_m^+$ species as only for oxygen atoms are bound in bridging position. But $Ta_3O_3^+$ and $Ta_3O_4^+$ fragmentation is the only observed pathway upon reaction with oxygen. Nevertheless, cationic tantalum clusters are clearly stabilized by the incorporation of oxygen atoms.

In summary, the different reactivities of tantalum oxides towards molecular oxygen may be explained either by a change in the reaction mechanism, an increased heat capacity due to more degrees of freedom or the stabilization by the formation of Ta-O bonds. None of these possibilities can be completely excluded. A change of the reaction mechanism, however, seems to be unlikely due to the assumed structures of tantalum oxides. Formation of Ta-O, as well as more degrees of freedom ultimately result in an increased heat capacity of the cluster. Both effects may contribute to the stability of the cluster and, therefore, to the deviation in the reaction pathway. Observed branching ratio may simply reflect the probability that a cluster is stabilized before it degrades.

4.5 Reaction of medium sized tantalum clusters with oxygen

A successive oxidation of the intact cluster is found for the reaction of molecular oxygen with cationic tantalum clusters composed of more than 13 atoms. On the other hand, degradation takes place for clusters with 8 atoms or fewer. The intermediate regime (n=9-12) is of special interest as both reaction pathways are simultaneously accessible. This behavior of cluster in this regime is discussed in the following chapter, on the example for Ta_9^+.

4.5.1 Reaction at 300 K

Ta_9^+ reacts with molecular oxygen by undergoing an oxidative degradation or an intact oxidation. Mass spectra of the reaction at a temperature of 300 K, and recorded at various reaction times are shown in Figure 4.18. After a short reaction time of 10 ms (a) Ta_9^+ is the most abundant species, but a significant amount of species that are the result of oxidative degradation (Ta_8O^+, $Ta_7O_2^+$ and $Ta_6O_3^+$) are observed. The presence, albeit less pronounced, of $Ta_9O_2^+$ indicates the accessibility of the intact oxidation pathway. For longer reaction times (b) several points should be noted. Firstly, the Ta_9^+ (oxide) species reacts to form species with a solely even number of oxygen atoms. The same phenomenon is observed for fragmentation products such as Ta_8O^+, resulting in the formation of $Ta_8O_3^+$, $Ta_8O_5^+$ and so on. Furthermore, the cluster degradation process has progressed as demonstrated by a shift of the mass spectrum towards smaller cluster sizes. More importantly, high intensities of many Ta_4^+ species ($Ta_4O_{5,7,9,11}^+$) are present. As the reaction continues (4.18 c), d)) most of the larger clusters have been degraded to $Ta_4O_5^+$, which in turn undergoes an intact oxidation towards $Ta_4O_{11}^+$ and latter eventually becomes the dominant species. Small amounts of the intermediately formed cluster sizes also undergo an intact oxidation to form a final cluster oxide species, i.e., $Ta_5O_{12}^+$,

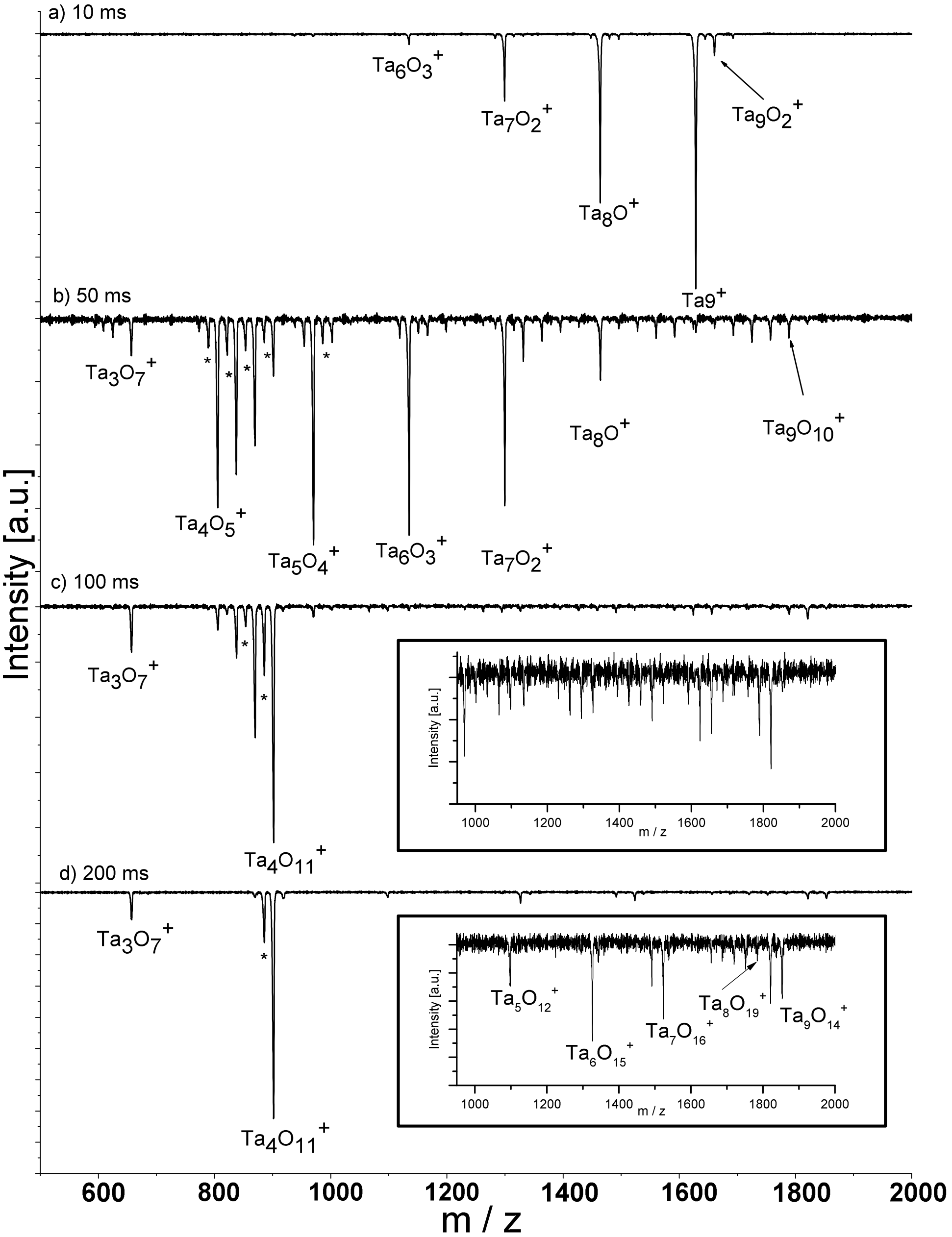

Figure 4.18: *Sum of the mass spectra at delays t_D of 300, 330, 350, 380, 420, 430 and 450 µs of the oxidation of Ta_9^+ for reaction times of a) 10 ms, b) 50 ms, c) 100 ms and d) 200 ms. The main reaction channel is the consecutive oxidative degradation towards $Ta_4O_5^+$ and its subsequent intact oxidation to $Ta_4O_{11}^+$. Additionally, small amounts of intermediately formed cluster sizes are intactly oxidized as well. Low intensity peaks marked with a cross are the result of the ejection of a tantalum atom from the cluster. Peaks marked with an asterisk are due to a side reaction with water.*

$Ta_6O_{15}^+$, $Ta_7O_{16}^+$ and $Ta_8O_{16}^+$. These species, as well as, the product of the intact oxidation of Ta_9^+ are depicted in the inset of Figure 4.18 d).

For the reaction of molecular oxygen with Ta_9^+ two major reaction pathways are found. Similar to Ta_{20}^+, a successive oxidation of the intact cluster is observed:

$$Ta_9^+ \xrightarrow{k_{A9-1}} Ta_9O_2^+ \xrightarrow{k_{A9-2}} Ta_9O_{m+4}^+ \xrightarrow{k_{3A}} \ldots . \tag{4.21}$$

This reaction ends after a certain amount of oxygen is adsorbed on the tantalum clusters. In the case of Ta_9^+, 14 oxygen atoms can be adsorbed on the clusters. A second pathway is the dissociation of the oxygen molecule and fragmentation of the tantalum cluster, similar to the reaction pathway found for Ta_8^+:

$$Ta_9O^+ \xrightarrow{k_{F9}} Ta_8O^+ \xrightarrow{k_{F8}} Ta_7O_2^+ \xrightarrow{k_{F7}} \ldots . \tag{4.22}$$

Both reaction pathways are possible for Ta_9^+ and for each of the formed intermediate species like Ta_8O^+ or $Ta_9O_2^+$. In total 39 different species are involved in the reaction of Ta_9^+ with oxygen. The complete reaction network is summarized in Figure 4.19. As depicted in Figure 4.18, a small fraction of $Ta_4O_5^+$ fragments to $Ta_3O_5^+$, which reacts further to $Ta_3O_7^+$. Note that the fragmentation mechanism deviates from the pattern observed for larger cluster sizes. Since the following discussion focuses on larger clusters the fragmentation pathway for $Ta_4O_5^+$ is neglected.

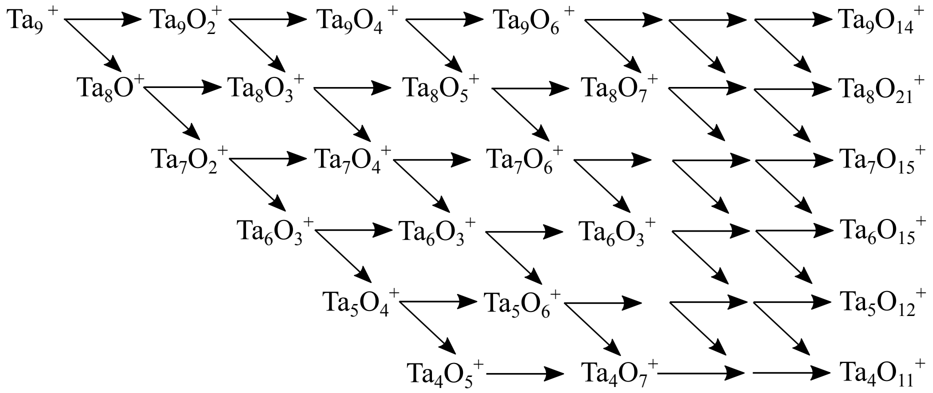

Figure 4.19: *Reaction network for the reaction of Ta_9^+ with molecular oxygen. Two reaction mechanisms can be identified: Firstly the adsorption of oxygen on the intact cluster (horizontal), secondly degradation of the tantalum cluster (diagonal). Note the variation in the oxygen content of the final species.*

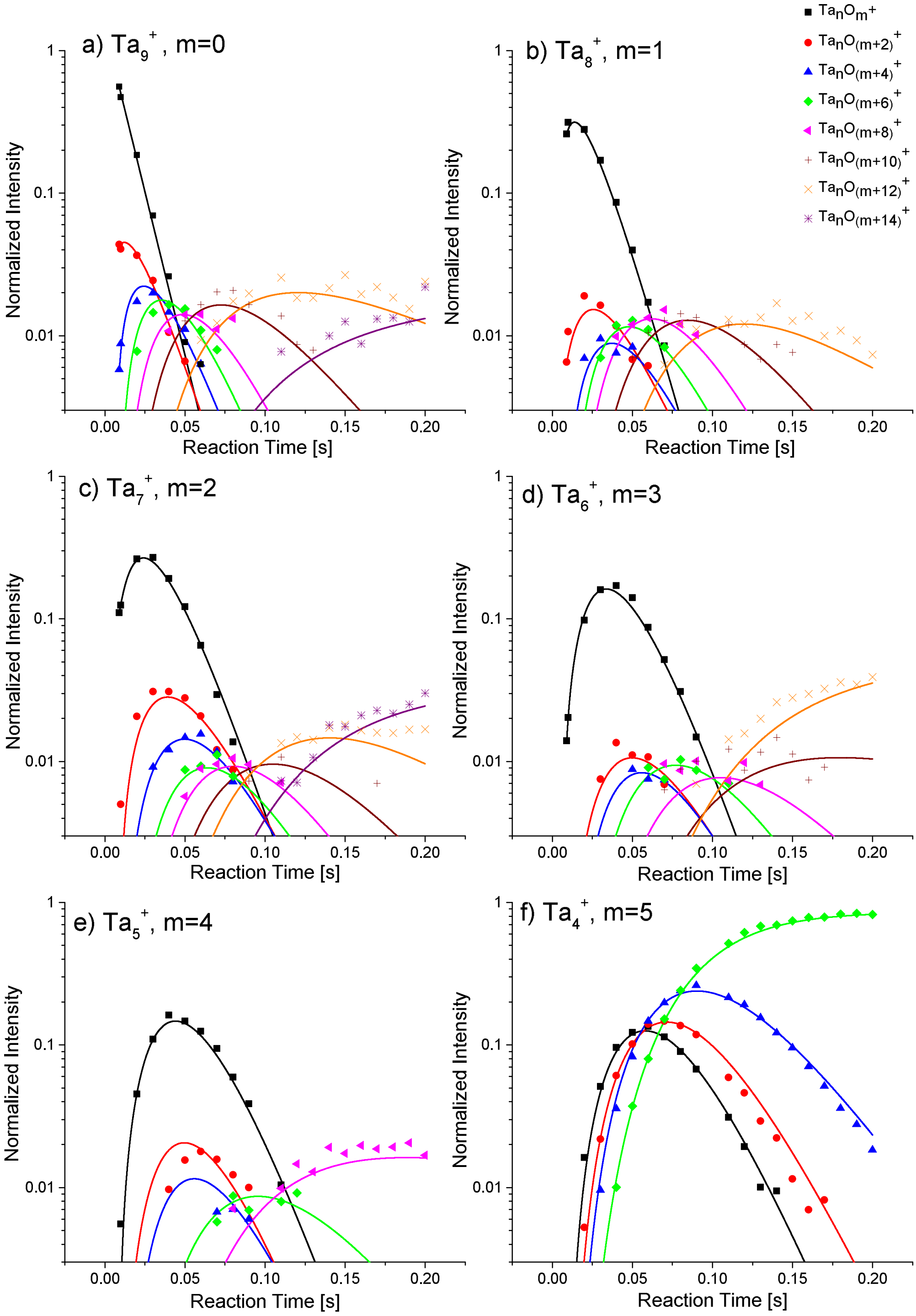

Figure 4.20: *a) - f) Normalized intensities for the reaction of Ta_9^+ with oxygen as a function of the reaction time. The results of the kinetic fit are depicted as solid lines.*

Figures 4.20 a) - f) illustrate the normalized intensities of the detected reaction products. Besides Ta_4^+ (f)), for each cluster size the initial fragmentation product (b) Ta_8O^+ ,c) $Ta_7O_2^+$, d) $Ta_6O_3^+$ and e) $Ta_5O_4^+$, respectively, is the most abundant species within the first tens of ms. These species are depleted by either the fragmentation pathway or the addition of further oxygen onto the intact cluster. Consequently, they cannot be detected after 150 ms. In the case of Ta_4^+, addition of further oxygen is the only possible pathway. After 200 ms $Ta_4O_{11}^+$ is the dominant reaction product. Kinetic data can now be fitted according to the proposed reaction network. Results of the kinetic fit are shown as solid lines. Despite the elaborate reaction network a good agreement between fit and measurement is achieved.

The calculated rate constants for the monitored species $Ta_nO_m^+$ are depicted in Figure 4.21. Rate constants of the intact pathway are shown as black squares, rate constants k_F of the fragmentation pathway as red dots. Accordingly, the two data points in Figure 4.21 at a m value of 0 corresponds to the reaction of Ta_9^+ to $Ta_9O_2^+$ (black) and Ta_8O^+ (red), respectively. At m=2 the reaction rates for $Ta_9O_2^+$ to form $Ta_9O_4^+$ and $Ta_8O_3^+$ are depicted. The calculated rate constant for the fragmentation of Ta_9^+ to Ta_8O^+ is about $2 \cdot 10^{-9}$ cm^3/s. This value is close to the determined rate constant for the reaction of Ta_{20}^+ to $Ta_{20}O_2^+$. The rate constant for the oxidation of the intact cluster (Ta_9^+ to $Ta_9O_2^+$) is significantly lower. Fragmentation is the preferred channel for the reaction of Ta_9^+ with oxygen. Nevertheless, a comparably small amount of $Ta_9O_2^+$ is detected as well. For this species a significantly lower rate constant for the fragmentation pathway $Ta_9O_2^+ \rightarrow Ta_8O_3^+$ is calculated. Interestingly, the rate constant for intact oxidation pathway increases drastically for the subsequent reaction steps. For $Ta_9O_4^+$ a rate constant close to zero is observed for the fragmentation pathway. For all higher oxides, oxidation of the intact cluster is the preferred pathway. For the last reaction step ($Ta_9O_{12}^+ \rightarrow Ta_9O_{14}^+$) the rate constants for both pathways are relatively low.

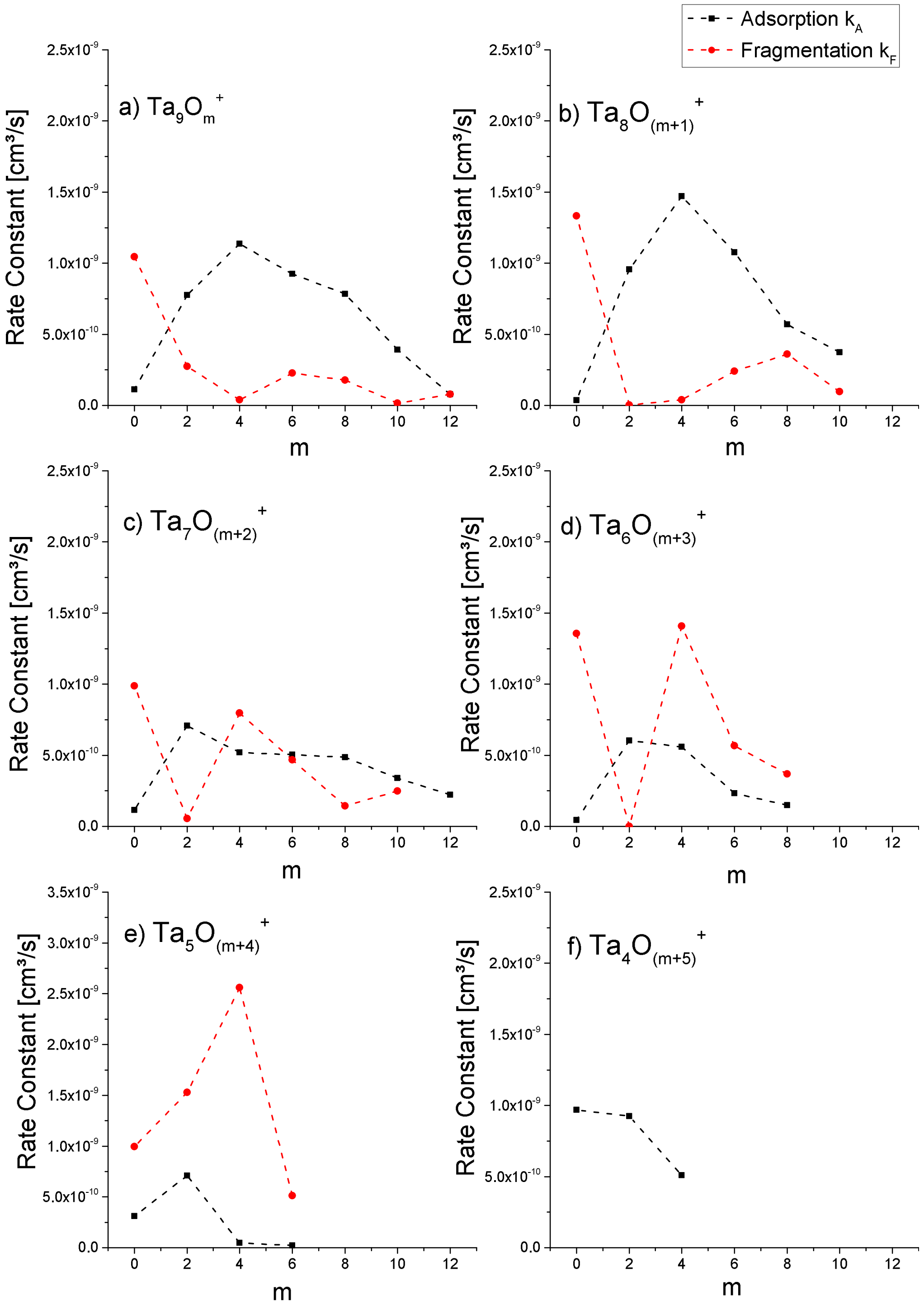

Figure 4.21: *a)-f) Pseudo-first order rate constants for oxidation of the intact cluster* k_A *and fragmentation of the tantalum cluster*k_F *for the reaction of* Ta_9^+ *with molecular oxygen. Dashed lines function as a guide to the eye.*

The reaction network will be investigated more closely in the following and rate constants serve as the basis for the examination. Rate constants, k_A, determined for the intact pathway first increase for the first three reaction steps. Consequently, the reaction from $Ta_9O_2^+$ to $Ta_9O_4^+$ is the fastest in this pathway. In particular larger oxides show the same trends as Ta_{20}^+ species upon the reaction with molecular oxygen. Up to $Ta_9O_8^+$ only a slight decrease of the rate constant is observed, for later reaction steps within the intact pathway a much steeper decrease takes place. On the one hand, for Ta_8O^+, a high rate constant for the fragmentation reaction is found. On the other hand for $Ta_8O_{2\text{-}6}^+$ the fragmentation pathway is strongly suppressed. For higher oxides like $Ta_8O_7^+$, $Ta_8O_9^+$ and $Ta_8O_{11}^+$ some fragmentation is observed again. In general trends for $Ta_8O_m^+$ species are very similar to those observed for $Ta_9O_m^+$ species.

For $Ta_7O_2^+$ (Figure 4.21 c)) the 'fragmentation' rate constant to $Ta_6O_3^+$ is much higher compared than the rate constant determined for the reaction to $Ta_7O_4^+$. In contrast to Ta_9^+ and Ta_8^+ species, significant rate constants for both pathways are found for all $Ta_7O_m^+$ species with the exception of $Ta_7O_2^+$. For Ta_6^+ species, fragmentation is always the preferred pathway except for $Ta_6O_5^+$. Rate constants observed for the intact pathway show the same trends as those observed for $Ta_9O_a^+$nd $Ta_8O_s^+$pecies. For Ta_5^+ species, the intact pathway is almost completely suppressed. Fragmentation of the tantalum cluster is the only relevant reaction pathway. Higher oxides (e.g. $Ta_5O_{12}^+$) are therefore almost exclusively formed by fragmentation of larger tantalum clusters. For Ta_4^+ species only minor fragmentation (to neglected Ta_3^+ species) takes place. Almost equal rate constants are found for the first two reaction steps for the intact pathway $Ta_4O_5^+$ to $Ta_4O_7^+$ and $Ta_4O_9^+$, respectively. The rate constant for the final step $Ta_4O_9^+$ to $Ta_4O_{11}^+$ is significantly lower.

4.5.2 Reaction at 100 K

The determination of activation energies requires the acquisition of kinetic data at different temperatures. The overall temperature effect will be discussed by comparing results from the previous chapter to data obtained at 100 K. To study the reaction of molecular oxygen with Ta_9^+ at 100 K mass spectra at delays t_d of 300, 330, 350, 380, 410, 420, 430 and 450 µs are recorded. The sum of these mass spectra is shown in Figure 4.22 for a reaction time of 10 ms. Equal amounts of Ta_9^+, Ta_8O^+ and $Ta_7O_2^+$ are detected. In general, the same reaction pathways as for 300 K are

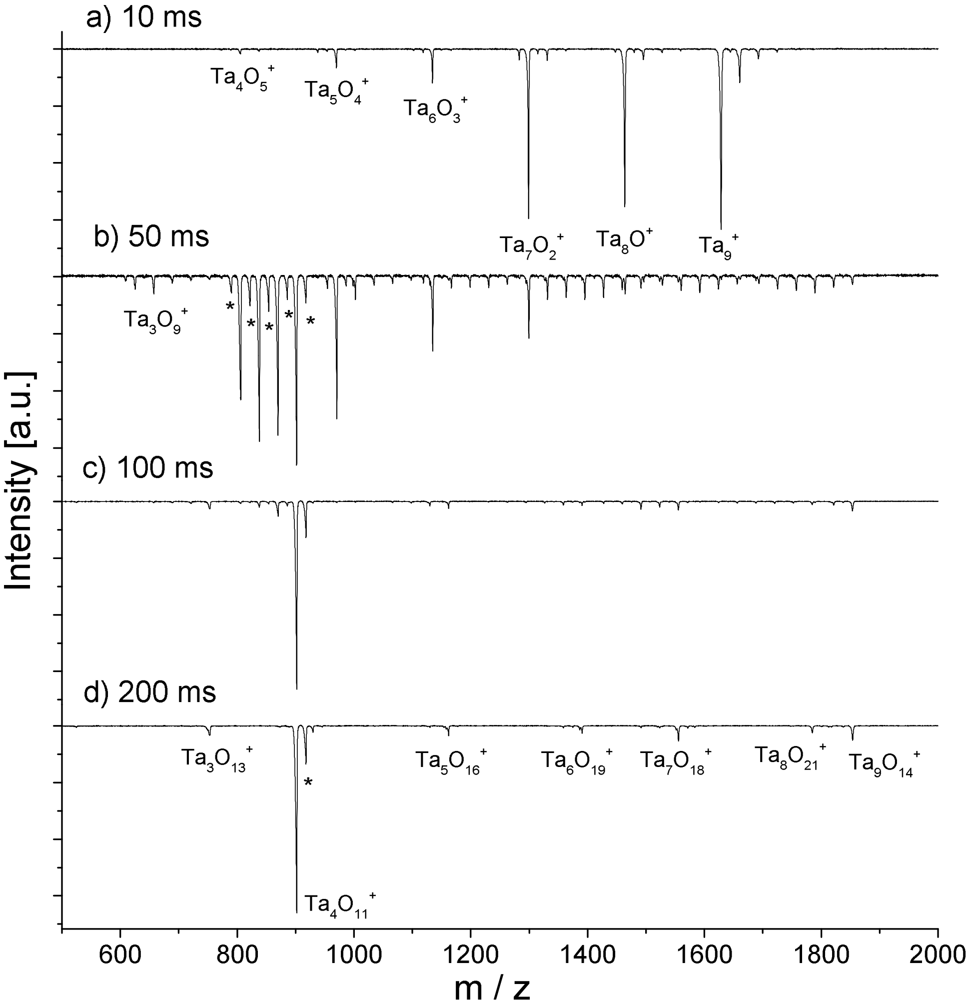

Figure 4.22: *Sum of the mass spectra at delays* t_D *of 300, 330, 350, 380, 420, 430 and 450 µs of the oxidation of* Ta_9^+ *for reaction times of a) 10 ms, b) 50 ms, c) 100 ms and d) 200 ms. The main reaction channel is the consecutive oxidative degradation towards* $Ta_4O_5^+$ *and its subsequent intact oxidation to* $Ta_4O_{11}^+$*. Additionally, small amounts of intermediately formed cluster sizes are intactly oxidized as well. Low intensity peaks marked with a cross are the result of the ejection of a tantalum atom from the cluster. Peaks marked with an asterisk are due to a side reaction with water.*

found. The major pathway is the successive fragmentation of the tantalum cluster from Ta_9^+ to $Ta_4O_5^+$. As depicted in c), the fragmentation pathway is completed after a reaction time of 100 ms. For longer reaction times d) an additional oxidation of (the intact) intermediate species is found. Stable side reaction products are $Ta_9O_{14}^+$, $Ta_8O_{21}^+$, $Ta_7O_{18}^+$, $Ta_6O_{18}^+$ and $Ta_5O_{16}^+$. The main reaction product of the reaction of oxygen with Ta_9^+ is again $Ta_4O_{11}^+$.

Figure 4.23 illustrates rate constants calculated for the fragmentation of the cluster as well as the oxidation of the intact cluster for each of the detected species. Compared to the reaction at 300 K, lower rate constants are found for 100 K. Rate constants determined for the intact pathway show the same behavior as for the reaction at 300 K with the exception of $Ta_6O_m^+$ species. An increase for the first reaction steps, is followed by a slight decrease and a further steeper decrease for the last reaction steps. As discussed for the reaction of Ta_{20}^+ with molecular oxygen the latter effect is less pronounced at lower temperatures. In contrast to 300 K, rate constants determined for the intact pathway for $Ta_6O_m^+$ species are close to zero. For $Ta_9O_{0,2,4,6,8}^+$ significant rate constants for the fragmentation pathway are observed, although the rate constant decreases with increasing number of oxygen atoms. For $Ta_9O_{10}^+$ and $Ta_9O_{12}^+$ no fragmentation is observed anymore. A similar trend is observed for Ta_8^+ species. Trends for the fragmentation pathway of $Ta_{5\text{-}7}O_m^+$ are similar to those identified for the reaction with molecular oxygen at 300 K.

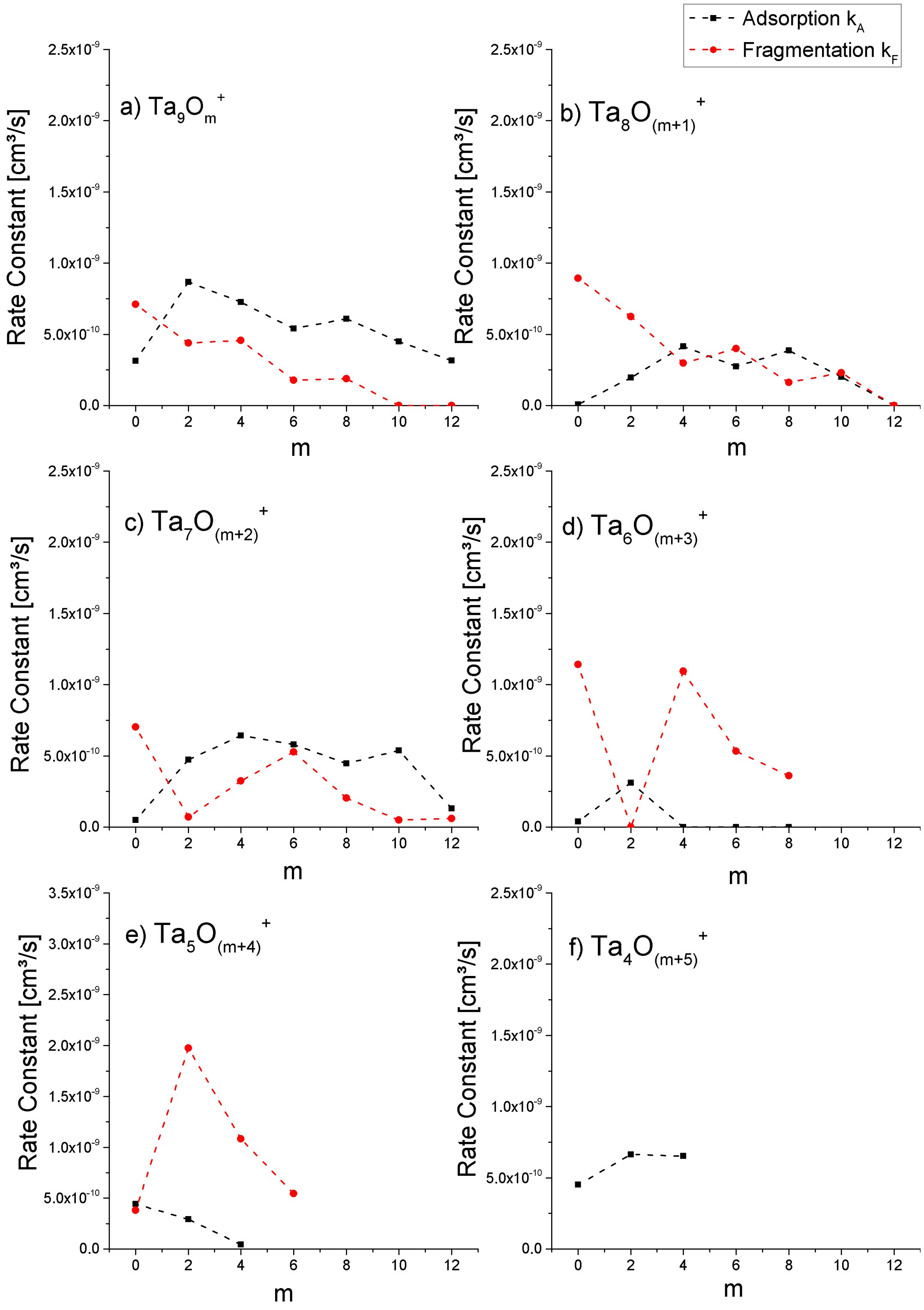

Figure 4.23: *a)-f) Pseudo-first order rate constants for oxidation of the intact clusters k_A and oxidative fragmentation k_F for the reaction of Ta_9^+ with molecular oxygen. Dashed lines function as a guide to the eye.*

4.5.3 Arrhenius plot and activation energies

The rate constants of the fragmentation pathway (see Scheme 4.23) are depicted in Figure 4.24 which is similar to the fragmentation pathway of Ta_8^+ and Ta_7^+. A slight variation of the rate constants with the number of tantalum atoms per cluster is observed. This effect is also illustrated in Figure 4.24. The rate constants for the fragmentation pathway of Ta_8^+ to Ta_7O^+ and Ta_8O^+ and $Ta_7O_2^+$ (k_{F8}), respectively, are higher compared to the 'adjacent' fragmentation steps. The same phenomenon is observed for k_{F6}. Consequently, the observed oscillation of the rate constant seems to be linked to the number of tantalum atoms and not to the number oxygen atoms, as those depend on the initial bare tantalum clusters and are therefore different for the three experiments depicted.

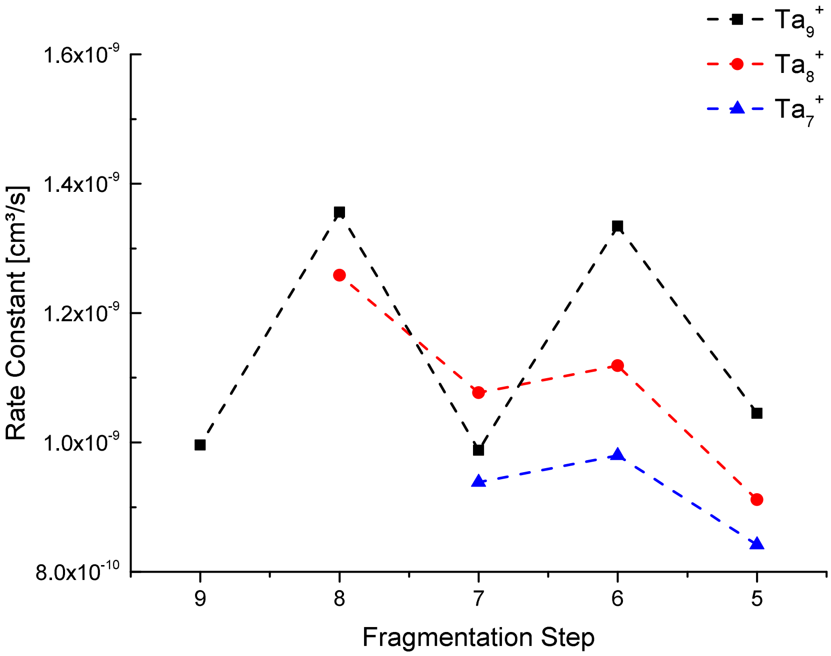

Figure 4.24: *Rate constants for the fragmentation pathway for the reaction of Ta_9^+, Ta_8^+ and Ta_7^+ with oxygen. Dashed lines function as a guide to the eye.*

The reaction of oxygen with Ta_9^+ has been studied at 100 K, 150 K, 200 K, 250 K and 300 K. Thereby the temperature dependence of the rate constants for the intact as well as for the fragmentation pathway can be studied. Figure 4.25 b) depicts the rate constants determined for each fragmentation step as a function of the inverse temperature in a logarithmic scale. For all reaction steps, a linear dependence is

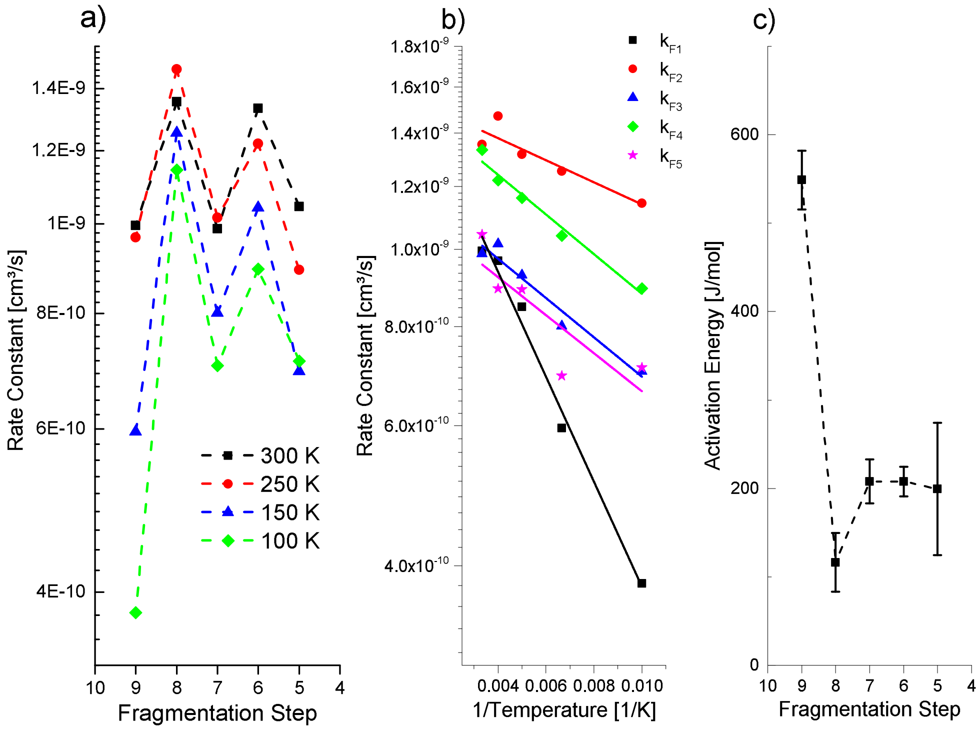

Figure 4.25: *a) Pseudo-first order rate constants for the main fragmentation pathway* $Ta_9^+ \rightarrow Ta_8O^+ \rightarrow Ta_7O_2^+$ *(as described by Scheme 4.23) of the reaction of molecular oxygen with* Ta_9^+ *at 100 K. b) Arrhenius plot for the fragmentation pathway. c) Determined activation energies. Dashed lines function as a guide to the eye.*

found. The resulting activation energies are illustrated in Figure 4.25 c). Activation energies for the fragmentation are in the same order of magnitude as for the intact path way. The first fragmentation step F9 (Ta_9^+ to Ta_8O^+) has the highest activation energy of more than 500 J/mole. For later fragmentation steps the activation energy decreases, with the minimum, about 100 J/mol for the fragmentation of Ta_8O^+ to $Ta_7O_2^+$. Later fragmentation steps have a slightly higher activation energy again. This trend is similar to the activation energies found for the reaction of Ta_8^+ with oxygen.

The kinetic evaluation of the intact oxidation pathway was performed as well. Figure 4.26 a) illustrates rate constants calculated for the intact oxidation of Ta_9^+ (described by Scheme 4.22) as a function of the reaction step for 100 K, 150 K, 250 K and 300 K. For all of these temperatures the rate rapidly increases until the third reaction step A3. In the first reaction step fragmentation is the dominant reaction pathway; only a small rate constant is observed for the intact oxidation. As soon as the first oxygen molecule is bound to cluster, the fragmentation pathway is sup-

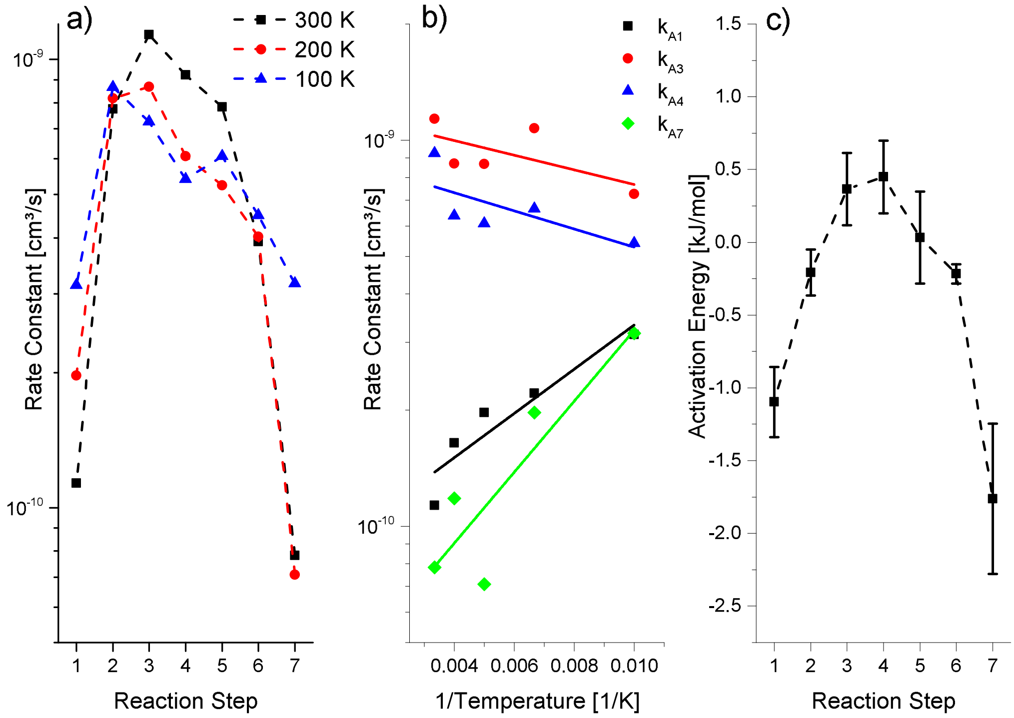

Figure 4.26: *a) Rate constants for the the intact pathway for* Ta_9^+ *as a function of the reaction step. b) Arrhenius plot for reaction steps* k_{A2}, k_{A4} *and* k_{A7} *c) Determined activation energies as a function of the reaction step.*

pressed. Analogous to the reaction of Ta_{20}^+ with oxygen, it can be assumed that the oxygen molecule dissociates and two separate oxygen atoms are attached to the cluster. Therefore, the rate constants for the intact pathway are larger. After the fifth reaction step, a steep decrease of the obtained rate constants is found for all temperatures. The latter effect is similar to the reaction of Ta_{20}^+ with molecular oxygen. By variation of the temperature, the temperature dependence for each reaction step is revealed. While the rate constant k_1 and k_2 of the first two reaction steps decrease with higher temperatures, the rate constants of reaction steps 3 and 4 and 5 increase. The last two reaction steps feature again a negative temperature dependence. Hence, the rate constant is higher for lower temperatures. Figure 4.26 b) depicts the logarithmic rate constants for reaction steps A1, A2, A4 and A7 as a function of the inverse temperature. For all four steps a linear dependence is found. From the slope of the linear regression the activation energy of the reaction can be calculated according to Equation 4.11. The obtained activation energies are shown in Figure 4.26 c). Evaluation of the temperature dependence of the rate constant reveals that reaction steps A1, A2, A6 and A7 feature negative activation energies.

Positive activation energies found for the other steps are in the same order as those found for the first reaction steps of the oxidation of Ta_{20}^{+}.

4.5.4 Discussion

The reaction of medium sized cationic tantalum clusters with 9 and 12 atoms have been studied for the example of Ta_9^+. Three major effects are observed:

1. The oxidation of the intact cluster as well as oxidative degradation are possible.
2. Fragmentation is the preferred pathway for Ta_9^+, Ta_8O^+ and $Ta_7O_2^+$. The observed behavior is similar to the reaction of Ta_8^+ with molecular oxygen.
3. Oxidation of the intact cluster is preferred for clusters with higher numbers of oxygen atoms. This behavior is analogous to the reaction of Ta_{20}^{+} with molecular oxygen.

The dynamic change between fragmentation upon reaction with oxygen and oxidation of the intact cluster for the monitored species is reflected by the branching ratio $\frac{k_F}{k_A+k_A}$.

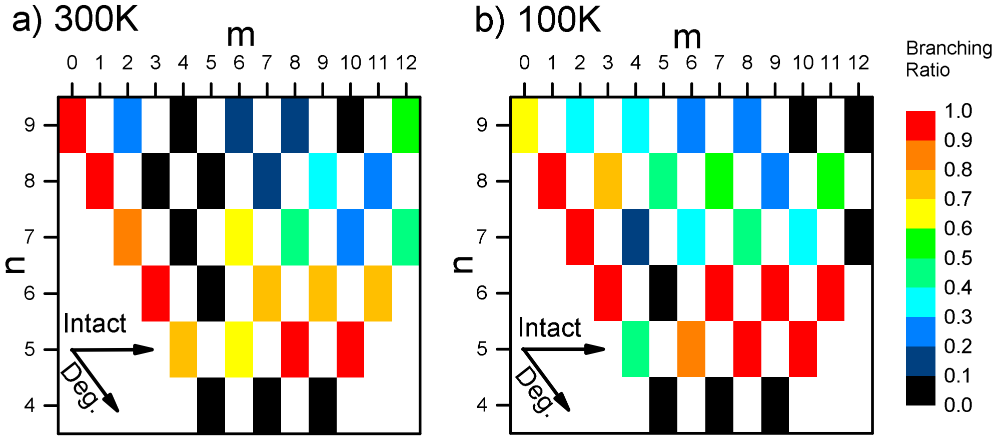

Figure 4.27: *a) Branching ratios $\frac{k_F}{k_A+k_A}$ for species $Ta_nO_m^+$ at 300 K. b) Branching ratios at 100 K. Rectangles colored black indicate the preference towards oxidative fragmentation, moving to higher m (from left to right). On the other hand, predominant fragmentation is indicated by rectangles in a red shade and the reaction progresses towards higher n and smaller m simulataneously (diagonally to the bottom right).*

Figure 4.27 a) depicts branching ratios at 300 K. While for Ta_9^+ a branching ratio close to 1 is found, the branching ratio for $\mathrm{Ta_9O_2^+}$ is approximately 0.25 and close to zero for $\mathrm{Ta_9O_4^+}$. Similar to the effects for the reaction of oxygen with smaller clusters, this finding is a strong indication that fragmentation is suppressed for larger oxides. For $\mathrm{Ta_8^+}$, $\mathrm{Ta_7^+}$ and to a lesser degree $\mathrm{Ta_6^+}$ an analogous behavior is found. For all $\mathrm{Ta_5O_m^+}$ species branching ratios higher than 0.5 are observed. Therefore, the determined branching ratios point out the main reaction pathway for the gas-phase reaction of molecular oxygen with $\mathrm{Ta_9^+}$ as:

$$Ta_9^+ \xrightarrow[93\%]{k_{f9}} Ta_8O^+ \xrightarrow[92\%]{k_{f8}} Ta_7O_2^+ \xrightarrow[87\%]{k_{f7}} Ta_6O_3^+ \xrightarrow[97\%]{k_{f6}} Ta_5O_4^+ \xrightarrow[88\%]{k_{f5}} Ta_4O_5^+ \rightarrow Ta_4O_{11}^+. \tag{4.23}$$

The branching ratios the reaction of $\mathrm{Ta_9^+}$ with molecular oxygen at 100 K are illustrated in Figure 4.27. Some significant changes in the branching ratios are found in comparison to the results at 300 K. For $\mathrm{Ta_9^+}$, the branching ratio is lower than 0.7 at 100 K and higher than 0.9 at 300 K. Hence, the probability for the oxidation of the intact cluster is more than three times higher at 100 K. The lower temperature of cluster and oxygen molecules allows for a more efficient stabilization of the activated cluster-oxygen complex $\mathrm{Ta_9O_2^{+*}}$. It is therefore more likely that the intact cluster is oxidized. Surprisingly, the opposite trend is found for $\mathrm{Ta_9O_2^+}$ and all higher oxides, where lower temperatures favor the fragmentation pathway. $\mathrm{Ta_9O_2^+}$ is stabilized by the association of oxygen. The stabilization involves restructuring of the cluster-oxygen-complex. This process may be hampered at lower temperatures, the complex could be frozen in a relatively unstable state. Consequently, it is more likely that fragmentation upon reaction with an oxygen molecule occurs. Similar effects are found also for $\mathrm{Ta_8O_m^+}$ and to some degree for $\mathrm{Ta_7^+m}$ species.

Activation energies as well as rate constants for the intact pathway of $\mathrm{Ta_9O_{m>2}^+}$ species are in general very similar to those determined for the reaction of $\mathrm{Ta_{20}^+}$ with molecular oxygen. It seems reasonable to propose the same reaction mechanism. Up to $\mathrm{Ta_9O_8^+}$, oxygen dissociates and is bound to the cluster as single atoms. Afterwards oxygen is attached as an intact molecule. For the first five adsorbed oxygen molecules the back reaction in the Lindemann model is blocked, for example by a quick dissociation of the oxygen molecule. For the last two reaction steps, lower rate constants as well as a negative activation energies are found. The back reaction has a significant influence on the observed reaction. As a result, lower rate constants and a negative activation energy are observed [63]. For $\mathrm{Ta_9^+}$ and to some degree also for $\mathrm{Ta_9O_2^+}$, it is unlikely that the formed activated complex can absorb the excess heat released by the dissociation of the oxygen molecule and then be stabilized by

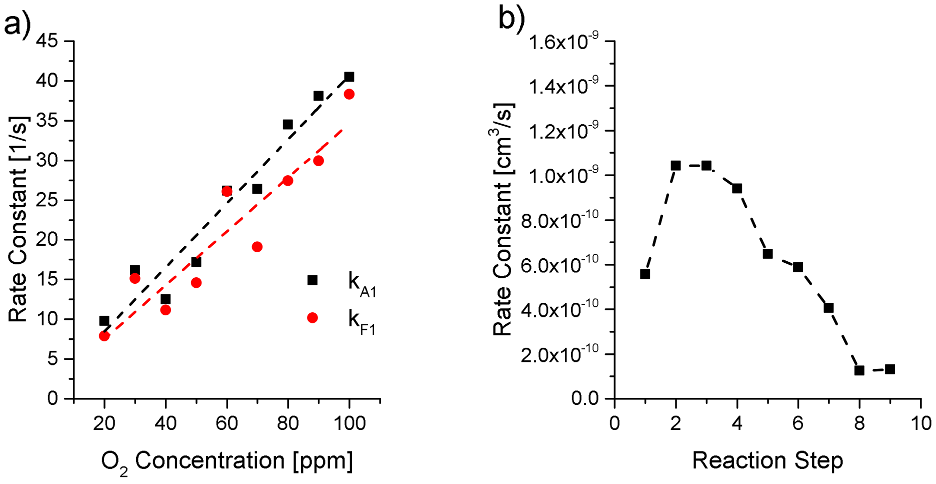

Figure 4.28: *a) Rate constants for the reaction of* Ta_{10}^{+} *with oxygen as a function of the oxygen concentration for the first fragmentation or intact pathway. b) Pseudo first-order rate constants for the intact pathway as a function of the reaction step. Dashed lines function as a guide to the eye*

collisions with a helium atom. Instead there is a high probability, reflected by the branching ratio, that the complex relaxes by the ejection of a TaO fragment. Lower rate constants for the oxidation of the intact cluster are observed. At lower temperatures the activated complex is more likely to be stabilized due to the lower amount of energy present in the system, resulting in higher rate constants for the oxidation of the intact cluster. Consequently, a formal negative activation energy is observed.

To further elucidate the fragmentation mechanism the reaction of Ta_{10}^{+} with molecular oxygen is studied for several oxygen concentrations within the buffer gas. The absolute pressure in trap was kept constant. Figure 4.28 a) illustrates the observed rate constants for the first reaction step, fragmentation oxidation of the intact cluster respectively. As the rate constants for both reaction pathways depend linearly on the oxygen concentration, it can be excluded that a second oxygen molecule is required for the fragmentation of a Ta_{10}^{+} cluster.

4.6 Summary

The reaction of cationic tantalum clusters Ta_n^{+} with molecular oxygen was studied in a wide size range (n=4-40) and at several temperatures. This extensive investigation revealed three size regimes, as small clusters (n=4-8), medium sized clusters (n=9-12) and large clusters (n>12) that behave differently. These are, in general, two reaction pathways were observed: the direct oxidation of the intact cluster ($\mathrm{Ta_nO_m^+} \xrightarrow{\mathrm{O_2}} \mathrm{Ta_nO_{m+2}^+}$) and the oxidative degradation of clusters ($\mathrm{Ta_nO_m^+} \xrightarrow{\mathrm{O_2}} \mathrm{Ta_{n\text{-}1}O_{m+1}^+} + \mathrm{TaO}$).

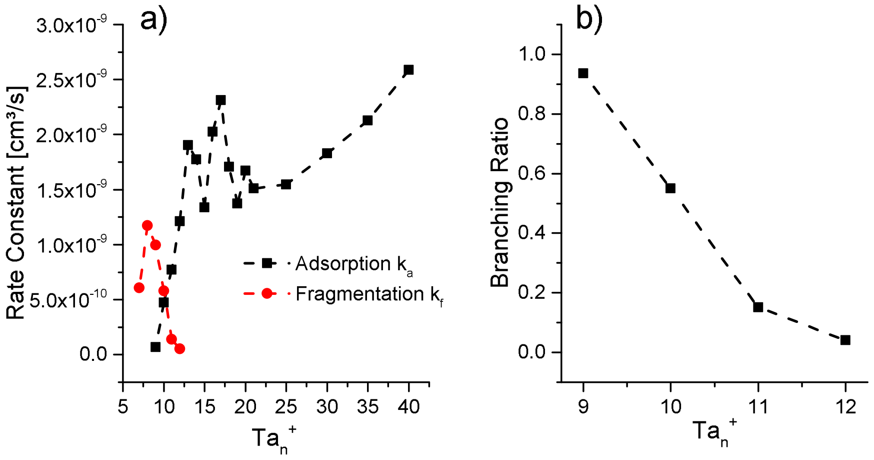

Figure 4.29: *a) Rate constants of the first reaction step for the fragmentation and intact pathway for tantalum clusters composed of 7 to 40 atoms as a function of cluster size n. b) Branching ratios for* Ta_9^+ *to* Ta_{12}^+*. A branching ratio of 1, indicates fragmentation being the only pathway, while a branching ration close to zero corresponds to intact oxidation.*

Figure 4.29 a) provides an overview of the calculated rate constants for the first reaction steps of both pathways. The rate constant for the fragmentation pathway increases from $\mathrm{Ta_7^+}$ to $\mathrm{Ta_8^+}$ and then quickly drops as the intact pathway becomes more important. For clusters composed of more than 13 atoms no rate constants for the fragmentation pathway can be obtained. The rate constants for the intact process increase with increasing cluster size. For $\mathrm{Ta_9^+}$ to $\mathrm{Ta_{12}^+}$ a steep increase is found, which for larger clusters is much slower. This increase may be explained by the higher collision rates for larger clusters. Compared to $\mathrm{Ta_{14}^+}$ and $\mathrm{Ta_{16}^+}$, a relatively low rate constant is determined for $\mathrm{Ta_{15}^+}$. This may be explained by the high stability of $\mathrm{Ta_{15}^+}$ [123]. From the rate constants the branching ratios $\frac{k_F}{k_F+k_A}$ for $\mathrm{Ta_9^+}$ to $\mathrm{Ta_{12}^+}$ are calculated. While for $\mathrm{Ta_9^+}$ degradation is the preferred pathway, both pathways have equal probabilities in the case of $\mathrm{Ta_{10}^+}$. For $\mathrm{Ta_{11}^+}$ and especially $\mathrm{Ta_{12}^+}$ branching ratios close to zero are calculated. The scalability of the branching ratio with cluster size indicates that heat capacity of the clusters has a crucial influence on the preferred

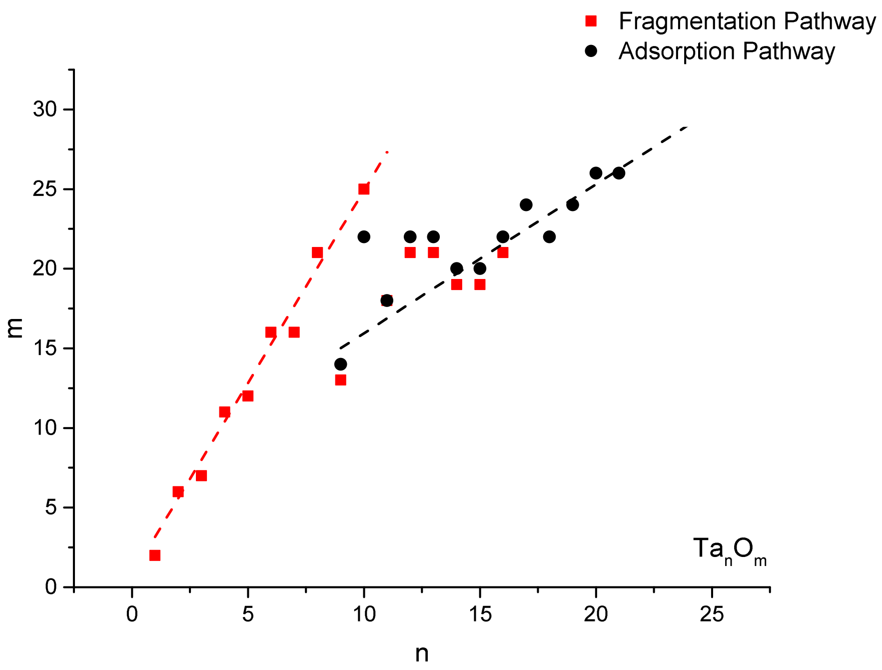

Figure 4.30: *Maximum of adsorbed oxygen atoms as a function of the cluster size at 300 K. The species formed via oxidation of the intact cluster are shown as black dots, species which are formed by at least on fragmentation step are shown as red squares.*

reaction pathway. Cluster with a lower heat capacity favor fragmentation upon oxidation, whereas cluster with a high heat capacity remain intact.

For all clusters sizes the adsorption of oxygen molecules stops at a certain quantity of oxygen atoms. Figure 4.30 illustrates the maximum amount of oxygen atoms adsorbed on each tantalum clusters at 300 K as function of cluster size. At temperatures lower than 100 K further oxygen atoms can be loosely bound to the tantalum clusters. The final species can be formed by two reaction pathways. The first is the direct adsorption of oxygen to the intact cluster. This pathway is possible for Ta_9^+ and all larger clusters. These species are shown as red squares. For the second pathway, shown as black dots, at least one degradation step is involved. As shown in Figure 4.30, the formation pathway does not influence the number of maximal adsorbed oxygen atoms. Note that in the case of pathways involving at least one fragmentation step the quantity of oxygen atoms can vary by one, depending on the number of degradation steps. Strikingly, the three size regimes found for the reaction of tantalum cluster with oxygen are by the final product species. Two regimes are found, in which the number of oxygen atoms scales linearly with the cluster size. Smaller clusters, with eight atoms or fewer, can take up on average 2.5 oxygen atoms per tantalum atom. This value reflects the oxidation states of tantalum (+5) and oxygen (-2). In fact those stochiometric tantalum-oxide species have also been observed by Fielicke [154] and Duncan [127]. This dominating electronic effect strongly indicates a structural rearrangement of the initial cluster.

For clusters larger than Ta_{13}^{+}, an average of only one oxygen atom per tantalum atom can be adsorbed. In between an intermediate regime is found where the final quantity of oxygen atoms cannot be predicted. These findings are another strong indication that for larger clusters the oxygen adsorbs on the surface of the clusters, where as for smaller clusters the oxygen is incorporated into the cluster. Hence, smaller cluster oxides that are the result of multiple degradation steps end up fully oxidized and have a higher oxygen content than larger clusters, which are oxidized at the surface. In a similar experiment cationic vanadium oxide clusters were produced in a laser vaporization cluster source and characterized by time-of-flight mass spectrometry [159]. For this purpose a small fraction of oxygen was mixed into the helium carrier gas. Main reaction products were vanadium oxides $Va_nO_m^+$ with an oxygen to vanadium ratio close to the stochiometric ratio of 2.5 independent of the cluster size n=1..22. For the present study these 'stochiometric species' are only observed for smaller tantalum clusters. The different behavior can be attributed to the different conditions during formation of the oxide species. When molecular oxygen is seeded into the carrier gas, oxygen is already present when the cluster is formed. Under such conditions electronic effects prevail. Hence, for all cluster sizes the stochiometric species are formed. For the present study, first the bare metal cluster is formed in the laser vaporization cluster source and afterwards oxidized in the ring electrode trap. For smaller cluster still electronic effects dominate the oxidation progresses until the cluster is completely oxidized. For bigger clusters this is no longer the case. Only the surface of the cluster is oxidized.

For clusters in the intermediate regime both effects may be possible. As illustrated in Figure 4.28 b), for the reaction of Ta_{10}^{+} a quick oxidation and formation of $Ta_{10}O_{14}^{+}$ is observed. This oxygen content would be predicted for a large tantalum cluster according to Figure 4.30. Afterwards, however, a slow oxidation to $Ta_{10}O_{26}^{+}$ takes place. This behavior may reflect a fast oxidation of the cluster surface, followed by a slower incorporation into the cluster structure. In summary, the detailed kinetic analysis revealed a complex size-dependent reactivity and the observed phenomena could be related to properties of the clusters.

5 Conclusion

Gas phase metal clusters are seen as model catalysts and, as a consequence, their properties are extensively investigated. While quite a few studies exist concerning the reactivity of small metal clusters composed of only a few atoms under multi-collision conditions e.g. [63] [67] [142], relatively little is known about the reactivity of larger clusters. The study of larger clusters and consequent investigation of their reaction kinetics have several requirements. Firstly, it is necessary to store clusters of a large mass range and expose them to a reactive gas for up to some seconds. Furthermore, a variable reaction temperature can provide further insight into the reaction mechanism or even open additional reaction pathways [68]. For highly reactive species it is necessary to achieve a good time resolution. The investigation of larger cluster additionally demands a product characterization method with high sensitivity and mass resolution. A major achievement of this work was the establishment of an experimental setup that fulfills all of these conditions in order to study the reactivity of free metal clusters. In this respect a setup to study the reactivity of free metal clusters has been designed, implemented and characterized during the first part of the present project. After a brief description of the experimental mode of operation and underlying requirements, the size-dependent oxidation of tantalum clusters is discussed as the first reaction studied with this setup.

In short, metal clusters, typically with one to more than hundred atoms, are produced by a laser vaporization cluster source [73] [124]. An electrostatic quadrupole bender is then utilized to separate cationic from anionic or neutral species. A newly installed quadrupole mass filter enables the selection of a specific cluster size. After size selection clusters are transferred into a ring electrode ion trap. The construction, characterization and optimization of the ring electrode trap has been a key part of the present work. It is shown that clusters in a mass range between 200 u and more than 16’000 u can be safely stored in the trap for more than 10 s. In fact, storage times of 5 minutes have been achieved.

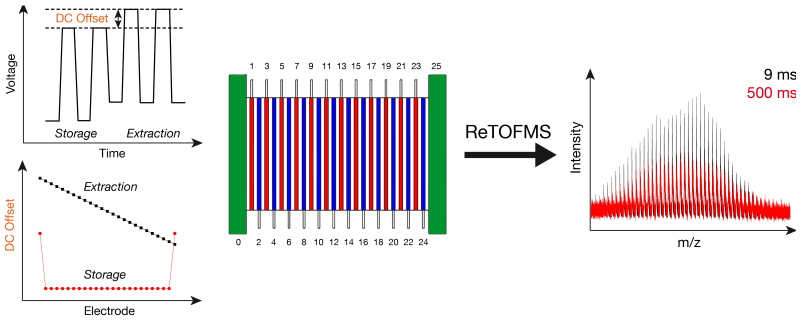

Figure 5.1: *Schematic of the ring electrode ion trap. Square wave potentials are exploited to store ions of a broad mass range. Superposition of a variable DC-Offset enables an efficient extraction of the ions into the time-of-flight mass spectrometer. Adapted with permission from [105]. Copyright 2015 Elsevier.*

As symbolized in Figure 5.1, the ring electrode ion trap is driven by a home-built electronics unit supplying square-wave potentials. This technique allows to supply RF-potentials with frequencies between 100 kHz and 750 kHz and peak-to-peak amplitudes up to 600 V to the electrodes of the trap. Clusters within the trap are thermalized by collisions with a buffer gas within a few ms [96]. The temperature of the trap can be varied between 15 K and 325 K. The formation of loosely bound van-der-Waals clusters at temperatures below 100 K indicates an efficient thermalization of the stored clusters. The implementation of an external gas reservoir enables mixing of reactive gases into the buffer gas. The flow of the gas into the ring electrode ion trap can be controlled either by a mass flow controller or a leak valve. The intense peak output of the pulsed laser vaporization cluster source allows the trap to be filled with clusters produced in a single laser pulse. The minimal reaction time is, therefore, given by the time necessary to thermalize clusters, which is in the order of some ms. Consequently, the setup enables the study of rapid reaction. The geometry of the ring electrode ion trap in combination with the DC-pulsing of the electrodes allows an efficient ejection of all stored clusters from the trap. To do so, the RF-potential applied to each electrode is shifted by a DC-offset. The potentials and their switching are performed by the newly developed electronics unit. With this device, the offset can be individually chosen for each electrode. This method enables the optimization of the ejection procedure for either a wide mass range or maximized sensitivity. Efficient ion ejection from the ring electrode ion trap allows the product characterization by time-of-flight mass spectrometry. For this purpose, a home-build reflectron time-of-flight mass spectrometer is employed, with which a mass resolution of 3’000 has been achieved.

Following the characterization of the system, the reactivity of cationic tantalum clusters, composed of four to forty atoms, towards oxygen is discussed. To achieve this, 100 ppm of oxygen is mixed into the buffer gas flowing into the ion trap. For all cluster sizes a rapid reaction with oxygen is observed. Three size regimes are identified, where the clusters exhibit significantly different reactivities under these conditions:

- Larger tantalum clusters, composed of thirteen atoms or more, stay intact upon reaction with oxygen.
- Smaller tantalum clusters, composed of eight atoms or fewer, fragment upon reaction with oxygen.
- For tantalum clusters composed of nine to twelve atoms both reaction mechanisms are present.

The oxidation of larger tantalum clusters is discussed on the example of Ta_{20}^{+}. A consecutive uptake of thirteen oxygen molecules is observed, with a final reaction product of $Ta_{20}O_{26}^{+}$. Time dependent concentrations can be fitted according to this simple model of consecutive oxidation steps. An excellent agreement between the fit and measured data is achieved and apparent rate constants are determined for each reaction step. The variation of the reaction temperature additionally enables activation energies to be determined for all processes. The activation energies are found to be very low and in the order of some hundred J/mol. Two reaction regimes are identified (see Figure 5.2). For the first seven reaction steps high rate constants

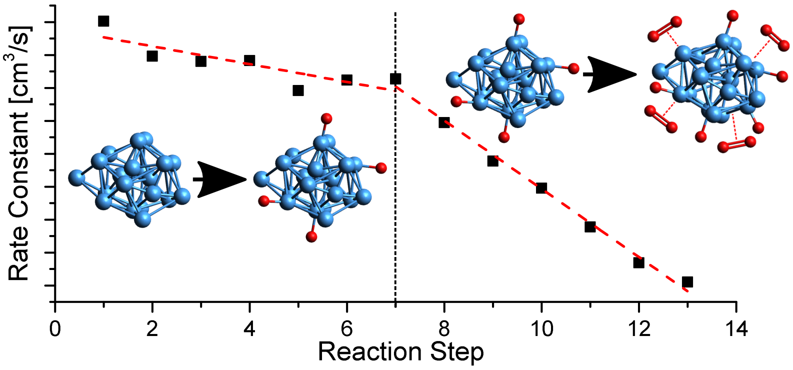

Figure 5.2: *Schematic mechanism of the oxidation of larger tantalum clusters. In the first regime (reaction steps 1-7) oxygen is dissociated on the cluster surface. Afterwards (reaction steps 8-13), the oxygen molecules may stay intact upon reaction.*

and comparable high activation energies have been observed. After the seventh step a simultaneous drop of the rate constant and activation energy is observed. This finding is attributed to two different reaction mechanisms. In a first reaction step molecular oxygen attaches to the cluster and an activated complex is formed. The oxygen molecule is quickly dissociated and is bound to the surface of the cluster as individual atoms. As the reaction progresses the cluster surface may become saturated or the electron density may become insufficient to dissociate the oxygen molecule. Additional oxygen molecules therefore stay intact upon oxidation. For the later reaction steps the oxygen molecule remains intact due to the decreased electron density at the surface of the cluster. Consequently, it is much more likely that the additionally attached oxygen molecule desorbs, resulting in a lower apparent rate constant and a lower activation energy at the same time.

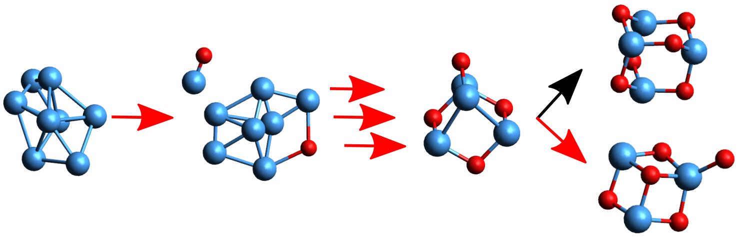

Figure 5.3: *Schematic mechanism of the reaction of smaller cationic tantalum clusters with oxygen. Clusters undergo oxidative degradation by the ejection of a TaO fragment. Intermediate oxides are stabilized and therefore may remain intact upon oxidation.*

As illustrated in Figure 5.3, smaller clusters exclusively fragmented upon reaction with oxygen by the ejection of a TaO-fragment. The newly formed $\mathrm{Ta_{n\text{-}1}O_{m+1}^+}$ even further fragments to $\mathrm{Ta_{n\text{-}2}O_{m+2}^+}$. The cluster stability increases with each further adsorbed oxygen atom until the metal oxide cluster remains intact upon reaction with oxygen. In the case of $\mathrm{Ta_4O_x^+}$ species:

- Oxides comprising three or less oxygen atoms mostly fragment.
- Oxides comprising five or more oxygen atoms remain intact upon reaction with oxygen.
- For $\mathrm{Ta_4O_4^+}$ both reaction pathways almost have almost the same probability.

A similar behavior is found for the reaction of $\mathrm{Ta_9^+}$ with oxygen. The bare cluster fragments with a probability of more than 90% when reacting with oxygen. Nevertheless, a small amount of $Ta_9O_2^+$ and subsequently $Ta_9O_4^+$ is formed. The reaction proceeds towards $Ta_9O_{14}^+$. Overall, the reaction is similar to the oxidation of Ta_{20}^+. Compared to the bare cluster, species like $Ta_9O_2^+$ and $Ta_9O_4^+$ have a significantly higher probability to remain intact upon oxidation. Again, the attachment of oxygen results in a stabilization of the clusters. By decreasing the temperature, the fragmentation of Ta_9^+ is suppressed and more $Ta_9O_2^+$ is formed. However, $Ta_9O_2^+$ is also more likely to fragment. At lower temperatures the cluster stabilization may be hampered as the required restructuring of the clusters may be hampered. Accordingly, fragmentation is more likely to occur.

These three different reaction regimes can be attributed to the increased heat capacity of bigger clusters. As shown in Figure 5.4, the regimes are reflected by the oxygen content of the final reaction product. For smaller clusters, a maximum of 2.5 oxygen atoms per tantalum atom is bound to the cluster. This reflects the ratio of the oxidation states of tantalum (+5) and oxygen (-2). On larger cluster on average approximately one oxygen atom per tantalum atom is found. This finding can be explained by a change in the binding mechanism. For smaller clusters, oxygen is incorporated into the cluster structure, where as for larger clusters oxygen is bound to the surface of the cluster and the metal core of the cluster remains mostly intact.

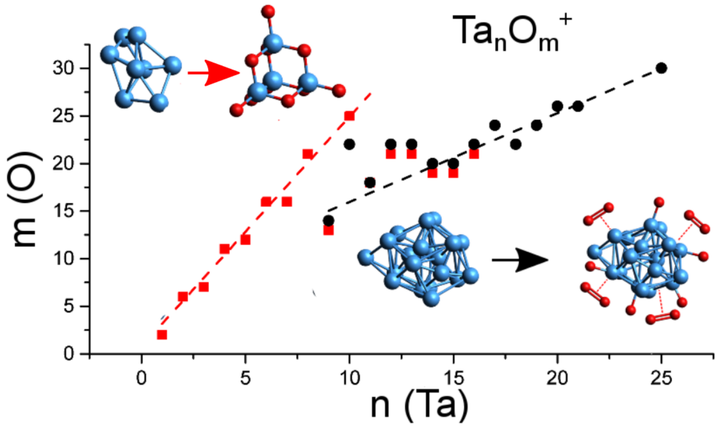

Figure 5.4: *For smaller tantalum clusters, oxygen is incorporated into the cluster and a stabilized tantalum-oxide core is formed. For larger clusters only the surface of the cluster is oxidized. Hence, smaller clusters can take up more oxygen per tantalum atom than larger clusters.*

6 Outlook

From an experimental point, it has been successfully shown that the setup allows the investigation of rapid and complex reactions with a high sensitivity. The mass range of the ring electrode ion trap in combination with the high resolution of the reflectron time-of-flight mass spectrometer enables the study of reactions, in particular, of large clusters. Up to now the, reaction between one reactive gas and cationic metal clusters has been studied, revealing the reactivity of tantalum clusters towards oxygen from which fundamental insights into the properties of the clusters can be obtained.

As a next step, reactions that are catalyzed by nanoparticles could be studied. Examples are the water-gas-shift-reaction [160], steam reforming reaction [161] or the activation of methane. Previous studies showed that already the tantalum cation can activate methane [61]. Activated methane is a prerequisite for the direct conversion of methane to methanol. Another possibility is the investigation of the reactivity of other metal clusters,like gold, iron, nickel or cobat clusters. Moreover, bimetallic clusters, which may have advantageous properties can be produced by the employed laser vaporization cluster source. Main goal of such studies is the identification of a full catalytic circle in the gas phase. Such processes have been studied previously [30] [66], but the vast majority of these studies is limited to rather small clusters composed of typically only a few atoms. Studies of supported clusters revealed that their catalytic activity varies dramatically with cluster size even for higher atoms counts. An example is the catalytic formation of CO_2 out of CO and O_2 on platinum clusters [23]. In fact, for Pt_8 and Pt_{20} different reaction pathways are found. These findings demonstrate that expanding catalytic gas phase experiments to larger clusters can reveal new reaction mechanisms and therefore contribute to the understanding of the catalytic activity of nanoparticles. Furthermore, a comparison between the catalytic activity of free and supported metal clusters can be drawn. The present setup is ideally suited for such studies as the laser vaporization produces clusters comprising more than a hundred atoms. The newly implemented ring electrode ion trap safely stores particles with a mass higher than 16’000 u. Moreover, the mass resolution of the reflectron time-of-flight mass spectrometer is good enough to conduct such studies.

Catalytic studies often require the introduction of two reactive gases into the ion trap. An inherent problem with such studies is that elucidation of the reaction pathway is not straightforward anymore [68] and can therefore be ambiguous. For oxidation reactions, specific metal-oxide-clusters are often of great interest as they mediate various reactions [71]. Therefore, a particular oxide has to be produced and transferred to the ion trap. While it is possible to seed oxygen into the cluster source, only limited control over the formed oxides is achieved by this method. One possibility to form a specific metal oxide and to disentangle reaction steps is by employing two separated reaction zones. For example a flow tube reactor can be added to the system. By injecting oxygen into the flow tube, metal clusters can be oxidized and afterwards size selected by the quadrupole mass filter. Moreover, other reaction intermediates of catalytic processes can be formed and transferred to the ring electrode ion trap. The benefits of a similar setup with two separated ion traps have already been discussed [16]. By the application of this methodology it is now possible to investigate further reactions, which are challenging and where insights on a fundamental level are still sparse.

An other and ambitious extension of the present experimental setup is the addition of a spectroscopic detection system. Controlled ion ejection of the ring electrode ion trap combined with the reflectron time-of-flight mass spectrometer would in principle allow the employment of spectroscopic methods like photo dissociation or even messenger tagging. Such studies can reveal for example binding sites of reaction intermediates and can therefore be applied to elucidate the underlying reaction mechanism in even more detail.

Bibliography

[1] P. Atkins, *Physikalische Chemie, 1987.* VCH, Weinheim, 1987.

[2] *IUPAC Compendium of Chemical Terminology*, Jun 2009.

[3] F. Ataya, M. A. Dubé, and M. Ternan, "Acid-catalyzed transesterification of canola oil to biodiesel under single-and two-phase reaction conditions," *Energy Fuels*, vol. 21, no. 4, pp. 2450–2459, 2007.

[4] R. Harding, A. Peters, and J. Nee, "New developments in fcc catalyst technology," *Appl. Phys. A*, vol. 221, no. 1, pp. 389–396, 2001.

[5] R. N. Carter, L. L. Smith, H. Karim, M. Castaldi, S. Etemad, G. Muench, R. S. Boorse, P. Menacherry, and W. C. Pfefferle, "Catalytic combustion technology development for gas turbine engine applications," *MRS Proceedings*, vol. 549, p. 93, Jan 1998.

[6] R. A. Van Santen and M. Neurock, *Molecular heterogeneous catalysis: a conceptual and computational approach.* John Wiley & Sons, 2009.

[7] J. C. Laube, M. J. Newland, C. Hogan, C. A. M. Brenninkmeijer, P. J. Fraser, P. Martinerie, D. E. Oram, C. E. Reeves, T. Röckmann, J. Schwander, E. Witrant, and W. Sturges, "Newly detected ozone-depleting substances in the atmosphere," *Nature Geosci.*, vol. 7, p. 266–269, Mar 2014.

[8] S. C. L. Kamerlin and A. Warshel, "At the dawn of the 21st century: Is dynamics the missing link for understanding enzyme catalysis?," *Proteins: Struct., Funct., Bioinf.*, vol. 78, no. 6, pp. 1339–1375, 2010.

[9] H. Davy, “Some new experiments and observations on the combustion of gaseous mixtures, with an account of a method of preserving a continued light in mixtures of inflammable gases and air without flame,” *Philosophical Transactions of the Royal Society of London*, vol. 107, pp. 77–85, 1817.

[10] M. Roberts, “Birth of the catalytic concept (1800-1900),” *Catal. Lett.*, vol. 67, no. 1, pp. 1–4, 2000.

[11] J. R. Ross, *Heterogeneous catalysis: fundamentals and applications.* Elsevier, 2011.

[12] S. M. Senkan, “High-throughput screening of solid-state catalyst libraries,” *Nature*, vol. 394, no. 6691, pp. 350–353, 1998.

[13] F. Haber and R. Le Rossignol, “Production of ammonia.,” Sept. 27 1910. US Patent 971,501.

[14] K. L. Manchester, “Man of destiny: the life and work of fritz haber,” *Endeavour*, vol. 26, no. 2, pp. 64–69, 2002.

[15] A. Mittasch, *Geschichte der Ammoniaksynthese.* Verlag Chemie, 1951.

[16] S. M. Lang and T. M. Bernhardt, “Gas phase metal cluster model systems for heterogeneous catalysis,” *Phys. Chem. Chem. Phys.*, vol. 14, no. 26, pp. 9255–9269, 2012.

[17] G. Ertl, “Reactions at surfaces: from atoms to complexity (nobel lecture),” *Angewandte Chemie International Edition*, vol. 47, no. 19, pp. 3524–3535, 2008.

[18] H. Schwarz, “Chemistry with methane: concepts rather than recipes,” *Angew. Chem. Int. Ed.*, vol. 50, no. 43, pp. 10096–10115, 2011.

[19] U. Heiz and E. Bullock, “Fundamental aspects of catalysis on supported metal clusters,” *J. Mater. Chem.*, vol. 14, no. 4, pp. 564–577, 2004.

[20] M. Haruta, T. Kobayashi, H. Sano, and N. Yamada, “Novel gold catalysts for the oxidation of carbon monoxide at a temperature far below 0°C.,” *Chem. Lett.*, vol. 16, no. 2, pp. 405–408, 1987.

[21] P. Collier, J. Iggo, and R. Whyman, "A review of modern transition metal nanoclusters," *J Mol Catal A*, vol. 145, pp. 44–55, 1999.

[22] M. Moreno-Manas and R. Pleixats, "Formation of carbon-carbon bonds under catalysis by transition-metal nanoparticles," *Acc. Chem. Res.*, vol. 36, no. 8, pp. 638–643, 2003.

[23] U. Heiz and U. Landman, *Nanocatalysis. Nanoscience and Technology.* Springer, 2007.

[24] A. Sanchez, S. Abbet, U. Heiz, W.-D. Schneider, H. Häkkinen, R. Barnett, and U. Landman, "When gold is not noble: nanoscale gold catalysts," *J. Phys. Chem. A*, vol. 103, no. 48, pp. 9573–9578, 1999.

[25] M. Haruta, "Catalysis: Gold rush," *Nature*, vol. 437, no. 7062, pp. 1098–1099, 2005.

[26] D. Astruc, F. Lu, and J. R. Aranzaes, "Nanoparticles as recyclable catalysts: The frontier between homogeneous and heterogeneous catalysis," *Angew. Chem. Int. Ed.*, vol. 44, no. 48, pp. 7852–7872, 2005.

[27] C. Harding, V. Habibpour, S. Kunz, A. N.-S. Farnbacher, U. Heiz, B. Yoon, and U. Landman, "Control and manipulation of gold nanocatalysis: effects of metal oxide support thickness and composition," *J. Am. Chem. Soc.*, vol. 131, no. 2, pp. 538–548, 2008.

[28] D. K. Böhme and H. Schwarz, "Gas-phase catalysis by atomic and cluster metal ions: The ultimate single-site catalysts," *Angew. Chem. Int. Ed.*, vol. 44, no. 16, pp. 2336–2354, 2005.

[29] B. Salisbury, W. Wallace, and R. Whetten, "Low-temperature activation of molecular oxygen by gold clusters: a stoichiometric process correlated to electron affinity," *Chem. Phys.*, vol. 262, no. 1, pp. 131–141, 2000.

[30] P. Schnabel, M. P. Irion, and K. G. Weil, "Evidence for low-pressure catalysis in the gas phase by a naked metal cluster: the growth of benzene precursors on iron (Fe_4^+)," *J. Phys. Chem.*, vol. 95, no. 24, pp. 9688–9694, 1991.

[31] M. F. Jarrold, J. E. Bower, and J. Kraus, "Collision induced dissociation of metal cluster ions: Bare aluminum clusters, Al_n^+ (n= 3–26)," *J. Chem. Phys.*, vol. 86, no. 7, pp. 3876–3885, 1987.

[32] K. Eller and H. Schwarz, "Organometallic chemistry in the gas phase," *Chem. Rev.*, vol. 91, no. 6, pp. 1121–1177, 1991.

[33] C. J. Howard, "Kinetic measurements using flow tubes," *J. Phys. Chem.*, vol. 83, no. 1, pp. 3–9, 1979.

[34] H. M. Smallwood, "The rate of recombination of atomic hydrogen," *J. Am. Chem. Soc.*, vol. 51, no. 7, pp. 1985–1999, 1929.

[35] D. W. Trainor, D. O. Ham, and F. Kaufman, "Gas phase recombination of hydrogen and deuterium," *J. Chem,. Phys*, vol. 58, p. 4599, 1973.

[36] A. Westenberg and N. De Haas, "Atom - molecule kinetics at high temperature using esr detection. technique and results for O + H_2, O + CH_4, and O + C_2H_6," *J. Chem. Phys.*, vol. 46, no. 2, pp. 490–501, 1967.

[37] T. G. Dietz, M. A. Duncan, D. E. Powers, and R. E. Smalley, "Laser production of supersonic metal cluster beams," *J. Chem. Phys.*, vol. 74, no. 11, pp. 6511–6512, 1981.

[38] M. Geusic, M. Morse, S. Obrien, and R. Smalley, "Surface reactions of metal clusters i: The fast flow cluster reactor," *Rev. Sci. Instrum.*, vol. 56, no. 11, pp. 2123–2130, 1985.

[39] D. Cox, R. Brickman, K. Creegan, and A. Kaldor, "Gold clusters: reactions and deuterium uptake," *Z. Phys. D: At., Mol. Clusters*, vol. 19, no. 4, pp. 353–355, 1991.

[40] T. H. Lee and K. M. Ervin, "Reactions of copper group cluster anions with oxygen and carbon monoxide," *J. Phys. Chem.*, vol. 98, no. 40, pp. 10023–10031, 1994.

[41] W. Vann, R. Bell, and A. Castleman, "Gas-phase reactions of nickel and nickel oxide clusters with nitrogen oxides. 3. reactions of cations with nitric oxide," *J. Phys. Chem. A*, vol. 103, no. 50, pp. 10846–10850, 1999.

[42] W. T. Wallace and R. L. Whetten, “Coadsorption of co and O_2 on selected gold clusters: Evidence for efficient room-temperature CO_2 generation,” *J. Am. Chem. Soc.*, vol. 124, no. 25, pp. 7499–7505, 2002.

[43] S. He, Y. Xie, F. Dong, and E. Bernstein, “Reaction of niobium and tantalum neutral clusters with low pressure, unsaturated hydrocarbons in a pickup cell: from dehydrogenation to met-car formation.,” *J. Chem. Phys.*, vol. 125, no. 16, pp. 164306–164306, 2006.

[44] M. Andersson, J. L. Persson, and A. Rosén, “Reactivity of Fe_n, Co_n, and Cu_n clusters with O_2 and D_2 studied at single-collision conditions,” *J. Chem. Phys.*, vol. 100, no. 30, pp. 12222–12234, 1996.

[45] D. Shin, Y. Matsuda, and E. Bernstein, “On the iron oxide neutral cluster distribution in the gas phase. i. detection through 193 nm multiphoton ionization,” *J. Chem. Phys.*, vol. 120, no. 9, pp. 4150–4156, 2004.

[46] R. St. Pierre and M. El Sayed, “Dependence of the reaction probability of benzene on the size of gaseous niobium clusters,” *J. Phys. Chem.*, vol. 91, no. 4, pp. 763–765, 1987.

[47] M. Zakin, D. Cox, and A. Kaldor, “Reaction of niobium clusters with benzene-H_6 and-D_6: Evidence for cluster-induced dehydrogenation,” *J. Phys. Chem.*, vol. 91, no. 20, pp. 5224–5228, 1987.

[48] M. Zakin, R. Brickman, D. Cox, and A. Kaldor, “Size-selective dehydrogenation of benzene by gas-phase niobium cluster ions (Nb_x^+),” *J. Chem. Phys.*, vol. 88, no. 9, pp. 5943–5947, 1988.

[49] S. Loh, D. A. Hales, L. Lian, and P. Armentrout, “Collision-induced dissociation of Fe_n^+ (n= 2–10) with Xe: Ionic and neutral iron binding energies,” *J. Chem. Phys.*, vol. 90, no. 10, pp. 5466–5485, 1989.

[50] D. Gerlich, “Inhomogeneous RF fields: A versatile tool for the study of processes with slow ions,” *Adv. Chem. Phys.*, pp. 1–176, Jan 1992.

[51] P. Armentrout, “Kinetic energy dependence of ion–molecule reactions: guided ion beams and threshold measurements,” *Int. J. Mass spectrom.*, vol. 200, no. 1, pp. 219–241, 2000.

[52] P. Armentrout, "Reactions and thermochemistry of small transition metal cluster ions," *Annu. Rev. Phys. Chem.*, vol. 52, no. 1, pp. 423–461, 2001.

[53] J. Conceicao, S. Loh, L. Lian, and P. Armentrout, "Guided ion beam studies of the reactions of Fe_n^+ (n= 2–15) with D_2: Cluster–deuteride bond energies as a chemical probe of cluster structures," *J. Chem. Phys.*, vol. 104, no. 11, pp. 3976–3988, 1996.

[54] P. Fayet, M. J. McGlinchey, and L. H. Wöste, "Bonding capabilities of nickel cluster ions: synthetic chemistry in a molecular beam," *J. Am. Chem. Soc.*, vol. 109, no. 6, pp. 1733–1738, 1987.

[55] J. B. Griffin and P. Armentrout, "Guided ion beam studies of the reactions of Fe_n^+ (n= 2–18) with $\mathrm{O_2}$: Iron cluster oxide and dioxide bond energies," *J. Chem. Phys.*, vol. 106, no. 11, pp. 4448–4462, 1997.

[56] C. Berg, T. Schindler, G. Niedner-Schatteburg, and V. E. Bondybey, "Reactions of simple hydrocarbons with Nb_n^+: Chemisorption and physisorption on ionized niobium clusters," *J. Chem. Phys.*, vol. 102, no. 12, pp. 4870–4884, 1995.

[57] M. B. Comisarow and A. G. Marshall, "Fourier transform ion cyclotron resonance spectroscopy," *Chem. Phys. Lett.*, vol. 25, no. 2, pp. 282–283, 1974.

[58] J. T. Watson and O. D. Sparkman, *Introduction to mass spectrometry: instrumentation, applications, and strategies for data interpretation.* John Wiley & Sons, 2007.

[59] J. Alford, P. Williams, D. Trevor, and R. Smalley, "Metal cluster ion cyclotron resonance. combining supersonic metal cluster beam technology with FT-ICR," *Int. J. Mass Spectrom. Ion Processes*, vol. 72, no. 1, pp. 33–51, 1986.

[60] J. Alford, F. Weiss, R. Laaksonen, and R. Smalley, "Dissociative chemisorption of molecular hydrogen on niobium cluster ions. a supersonic cluster beam FT-ICR experiment," *J. Phys. Chem.*, vol. 90, no. 19, pp. 4480–4482, 1986.

[61] R. Wesendrup and H. Schwarz, "Tantalum-mediated coupling of methane and carbon dioxide in the gas phase," *Angew. Chem. Int. Ed.*, vol. 34, no. 18, pp. 2033–2035, 1995.

[62] M. Neumaier, F. Weigend, O. Hampea, and M. M. Kappes, "Binding energies of CO on gold cluster cations Au," *J. Chem. Phys.*, vol. 122, p. 104702, 2005.

[63] T. M. Bernhardt, "Gas-phase kinetics and catalytic reactions of small silver and gold clusters," *Int. J. Mass Spectrom.*, vol. 243, no. 1, pp. 1–29, 2005.

[64] D. J. Goebbert, G. Meijer, and K. R. Asmis, "10K ring electrode trap-tandem mass spectrometer for infrared spectroscopy of mass selected ions," in *4th International Conference on Laser Probing LAP 2008*, pp. 22–29, American Institute of Physics, 2009.

[65] L. D. Socaciu, J. Hagen, U. Heiz, T. M. Bernhardt, T. Leisner, and L. Wöste, "Reaction mechanism for the oxidation of free silver dimers," *Chem. Phys. Lett.*, vol. 340, no. 3, pp. 282–288, 2001.

[66] S. M. Lang, T. M. Bernhardt, R. N. Barnett, and U. Landman, "Methane activation and catalytic ethylene formation on free Au_2^+," *Angew. Chem. Int. Ed.*, vol. 49, no. 5, pp. 980–983, 2010.

[67] S. M. Lang and T. M. Bernhardt, "Methane activation and partial oxidation on free gold and palladium clusters: Mechanistic insights into cooperative and highly selective cluster catalysis," *Faraday Discuss.*, vol. 152, pp. 337–351, 2011.

[68] S. M. Lang, T. M. Bernhardt, R. N. Barnett, and U. Landman, "Temperature-tunable selective methane catalysis on Au_2^+: From cryogenic partial oxidation yielding formaldehyde to cold ethylene production," *J. Phys. Chem. C*, vol. 115, no. 14, pp. 6788–6795, 2011.

[69] F. Cardarelli, P. Taxil, A. Savall, C. Comninellis, G. Manoli, and O. Leclerc, "Preparation of oxygen evolving electrodes with long service life under extreme conditions," *J. Appl. Electrochem.*, vol. 28, no. 3, pp. 245–250, 1998.

[70] S. Taylor, J. Hargreaves, G. Hutchings, and R. Joyner, "An initial strategy for the design of improved catalysts for methane partial oxidation," *Appl. Catal., A*, vol. 126, no. 2, pp. 287–296, 1995.

[71] K. Zemski, R. Bell, and A. Castleman, "Reactions of tantalum oxide cluster cations with 1-butene, 1, 3-butadiene, and benzene," *J. Phys. Chem. A*, vol. 104, no. 24, pp. 5732–5741, 2000.

[72] P. Milani and W. A. deHeer, "Improved pulsed laser vaporization source for production of intense beams of neutral and ionized clusters," *Rev. Sci. Instrum.*, vol. 61, no. 7, pp. 1835–1838, 1990.

[73] U. Heiz, F. Vanolli, L. Trento, and W.-D. Schneider, "Chemical reactivity of size-selected supported clusters: An experimental setup," *Rev. Sci. Instrum.*, vol. 68, no. 5, pp. 1986–1994, 1997.

[74] K. Lange, *Development of an experiment for the investigation of intrinsically chiral metal clusters in the gas phase.* PhD thesis, Universitätsbibliothek der TU München, 2014.

[75] M. A. Duncan, "Invited review article: Laser vaporization cluster sources," *Rev. Sci. Instrum.*, vol. 83, no. 4, p. 041101, 2012.

[76] R. F. Haglund, J. C. Miller, T. Lucatorto, and M. De Graef, *Laser Ablation and Desorption*, vol. 30. Academic Press, 1997.

[77] J. Liu, "Magnetism of nanophase composite films," *Handbook of Thin Films, Five-Volume Set*, vol. 5, p. 337, 2001.

[78] P. Milani and W. A. deHeer, "Relative thermometer for neutral clusters produced in laser-vaporization sources," *Phys. Rev. B: Condens. Matter*, vol. 44, no. 15, p. 8346, 1991.

[79] W. A. De Heer, "The physics of simple metal clusters: experimental aspects and simple models," *Reviews of Modern Physics*, vol. 65, no. 3, p. 611, 1993.

[80] P. E. Miller and M. B. Denton, "The transmission properties of an rf-only quadrupole mass filter," *International journal of mass spectrometry and ion processes*, vol. 72, no. 3, pp. 223–238, 1986.

[81] C. Trajber, M. Simon, S. Bohatka, and I. Futo, "A mass independent prefilter arrangement for quadrupole mass spectrometer," *Vacuum*, vol. 44, no. 5, pp. 653–656, 1993.

[82] W. Paul and H. Steinwedel, "A new mass spectrometer without a magnetic field," *Z. Naturforsch.*, vol. 8A, pp. 448 – 450, 1953.

[83] W. Paul and M. Raether, “Das elektrische massenfilter,” *Zeitschrift für Physik*, vol. 140, no. 3, pp. 262–273, 1955.

[84] J. Campana, “Elementary theory of the quadrupole mass filter,” *International Journal of Mass Spectrometry and Ion Physics*, vol. 33, no. 2, pp. 101–117, 1980.

[85] P. E. Miller and M. B. Denton, “The quadrupole mass filter: basic operating concepts,” *Journal of chemical education*, vol. 63, no. 7, p. 617, 1986.

[86] G. Bracco, “Comparison of quadrupole mass filters equipped with rods of different convexity: An analysis by finite element methods and trajectory simulations,” *Int. J. Mass Spectrom.*, vol. 278, no. 1, pp. 75–88, 2008.

[87] P. Dawson, “Quadrupole mass analyzers: performance, design and some recent applications,” *Mass Spectrom. Rev.*, vol. 5, no. 1, pp. 1–37, 1986.

[88] D. Bate, K. Dholakia, R. Thompson, and D. Wilson, “Ion oscillation frequencies in a combined trap,” *J. Mod. Opt.*, vol. 39, no. 2, pp. 305–316, 1992.

[89] D. Wineland, W. M. Itano, and R. Van Dyck Jr, “High-resolution spectroscopy of stored ions,” *Adv. At. Mol. Phys*, vol. 19, no. 1, pp. 135–187, 1983.

[90] E. Teloy and D. Gerlich, “Integral cross sections for ion-molecule reactions. I. The guided beam technique,” *Chem. Phys.*, vol. 4, no. 3, pp. 417–427, 1974.

[91] A. Sorgenfrei, *Ion-Molekül-Reaktionen kleiner Kohlenwasserstoffe in einem gekühlten Ionen-Speicher.* PhD thesis, Albert-Ludwigs-Universität Freiburg, 1994.

[92] D. Gerlich and S. Horning, “Experimental investigation of radiative association processes as related to interstellar chemistry,” *Chem. Rev.*, vol. 92, no. 7, pp. 1509–1539, 1992.

[93] S. Berge, P. Gartland, and B. Slagsvold, “Photoelectric work function of a molybdenum single crystal for the (100),(110),(111),(112),(114), and (332) faces,” *Surf. Sci.*, vol. 43, no. 1, pp. 275–292, 1974.

[94] B. Schulz *et al.*, “Thermophysical properties of sapphire, aln and mgal 2 o 4 down to 70 k,” *Journal of nuclear materials*, vol. 212, pp. 1065–1068, 1994.

[95] G. Kaefer, *Stosskomplexe in der Umgebung der Dissoziationsgrenze: experimentelle Untersuchungen in einem temperaturvariablen Hf-Ionenspeicher.* PhD thesis, Albert-Ludwigs-Universitäet Freiburg, 1989.

[96] J. Westergren, H. Grönbeck, S.-G. Kim, and D. Tománek, "Noble gas temperature control of metal clusters: A molecular dynamics study," *The Journal of chemical physics*, vol. 107, no. 8, pp. 3071–3079, 1997.

[97] G. Loriot and T. Moran, "Reliability of a capacitance manometer in the range $2{\cdot}10^{-4-5} \cdot 10^{-6}$ torr," *Rev. Sci. Instrum.*, vol. 46, no. 2, pp. 140–143, 1975.

[98] R. M. Jones, D. Gerlich, and S. L. Anderson, "Simple radio-frequency power source for ion guides and ion traps," *Rev. Sci. Instrum.*, vol. 68, no. 9, pp. 3357–3362, 1997.

[99] J. Richards, R. Huey, and J. Hiller, "A new operating mode for the quadrupole mass filter," *Int. J. Mass Spectrom. Ion Phys.*, vol. 12, no. 4, pp. 317–339, 1973.

[100] L. Ding, M. Sudakov, and S. Kumashiro, "A simulation study of the digital ion trap mass spectrometer," *Int. J. Mass Spectrom.*, vol. 221, no. 2, pp. 117–138, 2002.

[101] G. F. Brabeck and P. T. Reilly, "Mapping ion stability in digitally driven ion traps and guides," *Int. J. Mass Spectrom.*, vol. 364, pp. 1–8, 2014.

[102] S. Bandelow, G. Marx, and L. Schweikhard, "The stability diagram of the digital ion trap," *Int. J. Mass Spectrom.*, vol. 336, pp. 47–52, 2013.

[103] S. Bandelow, G. Marx, and L. Schweikhard, "The 3-state digital ion trap," *Int. J. Mass Spectrom.*, vol. 353, pp. 49–53, 2013.

[104] N. Deb, L. L. Pollum, A. D. Smith, M. Keller, C. J. Rennick, B. R. Heazlewood, and T. P. Softley, "Coulomb crystal mass spectrometry in a digital ion trap," *Phys. Rev. A: At. Mol. Opt. Phys.*, vol. 91, no. 3, p. 033408, 2015.

[105] D. Neuwirth, J. F. Eckhard, K. Lange, B. Visser, M. Wiedemann, R. Schröter, M. Tschurl, and U. Heiz, "Using controlled ion extraction to combine a ring electrode trap with a reflectron time-of-flight mass spectrometer," *Int. J. Mass Spectrom.*, vol. 387, no. 15, pp. 8 – 15, 2015.

[106] B. B. Dangi, N. A. Sassin, and K. M. Ervin, “Pulsed ion extraction diagnostics in a quadrupole ion trap linear time-of-flight mass spectrometer,” *Rev. Sci. Instrum.*, vol. 81, no. 6, p. 063302, 2010.

[107] S. J. Schowalter, K. Chen, W. G. Rellergert, S. T. Sullivan, and E. R. Hudson, “An integrated ion trap and time-of-flight mass spectrometer for chemical and photo-reaction dynamics studies,” *Rev. Sci. Instrum.*, vol. 83, no. 4, p. 043103, 2012.

[108] S. M. Michael, M. Chien, and D. M. Lubman, “An ion trap storage/time-of-flight mass spectrometer,” *Rev. Sci. Instrum.*, vol. 63, no. 10, pp. 4277–4284, 1992.

[109] U. J. Lorenz and T. R. Rizzo, “Planar multipole ion trap/time-of-flight mass spectrometer,” *Anal. Chem.*, vol. 83, no. 20, pp. 7895–7901, 2011.

[110] A. Luca, S. Schlemmer, I. Čermák, and D. Gerlich, “On the combination of a linear field free trap with a time-of-flight mass spectrometer,” *Review of Scientific Instruments*, vol. 72, no. 7, pp. 2900–2908, 2001.

[111] N. Heine and K. R. Asmis, “Cryogenic ion trap vibrational spectroscopy of hydrogen-bonded clusters relevant to atmospheric chemistry,” *International Reviews in Physical Chemistry*, vol. 34, no. 1, pp. 1–34, 2015.

[112] Q. Turchette, B. King, D. Leibfried, D. Meekhof, C. Myatt, M. Rowe, C. Sackett, C. Wood, W. Itano, C. Monroe, *et al.*, “Heating of trapped ions from the quantum ground state,” *Phys. Rev. A: At. Mol. Opt. Phys.*, vol. 61, no. 6, p. 063418, 2000.

[113] U. Boesl, R. Weinkauf, and E. Schlag, “Reflectron time-of-flight mass spectrometry and laser excitation for the analysis of neutrals, ionized molecules and secondary fragments,” *Int. J. Mass Spectrom. Ion Processes*, vol. 112, no. 2, pp. 121–166, 1992.

[114] W. Wiley and I. H. McLaren, “Time-of-flight mass spectrometer with improved resolution,” *Rev. Sci. Instrum.*, vol. 26, no. 12, pp. 1150–1157, 1955.

[115] R. Weinkauf, K. Walter, C. Weickhardt, U. Boesl, and E. Schlag, “Laser tandem mass spectrometry in a time of flight instrument,” *Z. Naturforsch., A: Phys. Sci.*, vol. 44, no. 12, pp. 1219–1225, 1989.

[116] B. Mamyrin, V. Karataev, D. Shmikk, and V. Zagulin, “The massreflectron, a new non-magnetic time-of-flight mass spectrometer with high resolution,” *Zh. Eksp. Teor. Fiz*, vol. 64, pp. 82–89, 1973.

[117] V. M. Doroshenko and R. J. Cotter, “Ideal velocity focusing in a reflectron time-of-flight mass spectrometer,” *J. Am. Soc. Mass Spectrom.*, vol. 10, no. 10, pp. 992–999, 1999.

[118] R. P. Schmid and C. Weickhardt, “Designing reflectron time-of-flight mass spectrometers with and without grids: a direct comparison,” *Int. J. Mass Spectrom.*, vol. 206, no. 3, pp. 181–190, 2001.

[119] A. Savitzky and M. J. Golay, “Smoothing and differentiation of data by simplified least squares procedures.,” *Anal. Chem.*, vol. 36, no. 8, pp. 1627–1639, 1964.

[120] J. I. Steinfeld, J. S. Francisco, and W. L. Hase, *Chemical kinetics and dynamics*. Prentice Hall, 1999.

[121] A. C. Hindmarsh, “Lsode and lsodi, two new initial value ordinary differential equation solvers,” *ACM Signum Newsletter*, vol. 15, no. 4, pp. 10–11, 1980.

[122] D. W. Marquardt, “An algorithm for least-squares estimation of nonlinear parameters,” *SIAM J Appl Math*, vol. 11, no. 2, pp. 431–441, 1963.

[123] M. Sakurai, K. Watanabe, K. Sumiyama, and K. Suzuki, “Magic numbers in transition metal (Fe, Ti, Zr, Nb, and Ta) clusters observed by time-of-flight mass spectrometry,” *J. Chem. Phys.*, vol. 111, no. 1, p. 235, 1999.

[124] K. Lange, B. Visser, D. Neuwirth, J. Eckhard, U. Boesl, M. Tschurl, K. Bowen, and U. Heiz, “Size-dependent gas phase reactivity of tantalum cluster cations with small alcohols,” *Int. J. Mass Spectrom.*, vol. 375, pp. 9–13, 2015.

[125] M. Zhou, J. Dong, L. Zhang, and Q. Qin, “Reactions of group V metal atoms with water molecules. matrix isolation FTIR and quantum chemical studies,” *J. Am. Chem. Soc.*, vol. 123, no. 1, pp. 135–141, 2001.

[126] P. Gruene, A. Fielicke, and G. Meijer, “Experimental vibrational spectra of gas-phase tantalum cluster cations,” *J. Chem. Phys.*, vol. 127, no. 23, p. 234307, 2007.

[127] K. Molek, T. Jaeger, and M. Duncan, "Photodissociation of vanadium, niobium, and tantalum oxide cluster cations.," *J. Chem. Phys.*, vol. 123, no. 14, pp. 144313–144313, 2005.

[128] Y. M. HANRICK and M. MORSE, "Comparative cluster reaction studies of the V, Nb, and Ta series," *J. Phys. Chem.*, vol. 93, no. 17, pp. 6494–6501, 1989.

[129] S. Cardonne, P. Kumar, C. Michaluk, and H. Schwartz, "Tantalum and its alloys," *Int. J. Refract. Met. Hard Mater.*, vol. 13, no. 4, pp. 187–194, 1995.

[130] G. L. Burke, "The corrosion of metals in tissues; and an introduction to tantalum," *Can. Med. Assoc. J.*, vol. 43, no. 2, p. 125, 1940.

[131] G. Harry, T. P. Bodiya, and R. DeSalvo, *Optical coatings and thermal noise in precision measurement.* Cambridge University Press, 2012.

[132] C. Christensen, R. de Reus, and S. Bouwstra, "Tantalum oxide thin films as protective coatings for sensors," *J. Micromech. Microeng.*, vol. 9, no. 2, p. 113, 1999.

[133] S. B. Basame and H. S. White, "Chemically-selective and spatially-localized redox activity at Ta/Ta_2O_5 electrodes," *Langmuir*, vol. 15, no. 3, pp. 819–825, 1999.

[134] Y. Takahara, J. N. Kondo, T. Takata, D. Lu, and K. Domen, "Mesoporous tantalum oxide. 1. Characterization and photocatalytic activity for the overall water decomposition," *Chem. Mater.*, vol. 13, no. 4, pp. 1194–1199, 2001.

[135] S. Heinbuch, F. Dong, J. Rocca, and E. Bernstein, "Experimental and theoretical studies of reactions of neutral vanadium and tantalum oxide clusters with no and nh3," *J. Chem. Phys.*, vol. 133, no. 17, p. 174314, 2010.

[136] K. Zemski, D. Justes, and A. Castleman, "Reactions of group v transition metal oxide cluster ions with ethane and ethylene," *J. Phys. Chem. A*, vol. 105, no. 45, pp. 10237–10245, 2001.

[137] H. Wang, R. Craig, H. Haouari, J.-G. Dong, Z. Hu, A. Vivoni, J. R. Lombardi, and D. Lindsay, "Absorption and raman spectroscopy of mass-selected tantalum tetramers in argon matrices," *J. Chem,. Phys*, vol. 103, no. 9, pp. 3289–3292, 1995.

[138] A. Fielicke, P. Gruene, M. Haertelt, D. J. Harding, and G. Meijer, "Infrared spectroscopy and binding geometries of oxygen atoms bound to cationic tantalum clusters," *J. Phys. Chem. A*, vol. 114, no. 36, pp. 9755–9761, 2010.

[139] H.-J. Zhai, B. Wang, X. Huang, and L.-S. Wang, "Structural evolution, sequential oxidation, and chemical bonding in tritantalum oxide clusters: $Ta_3O_n^-$ and Ta_3O_n (n = 1-8)," *J. Phys. Chem. A*, vol. 113, p. 9804–9813, Sep 2009.

[140] J. Du, X. Sun, and G. Jiang, "A theoretical study on Ta_n^+ cluster cations: Structural assignments, stability, and electronic properties," *J. Chem. Phys.*, vol. 136, no. 9, p. 094311, 2012.

[141] E. Parks and S. Riley, "Nickel cluster structure determined from the adsorption of molecular nitrogen: Ni_{49}-Ni_{71}," *Z. Phys. D: At., Mol. Clusters*, vol. 33, no. 1, pp. 59–70, 1995.

[142] S. M. Lang, I. Fleischer, T. M. Bernhardt, R. N. Barnett, and U. Landman, "Size-dependent self-limiting oxidation of free palladium clusters," *J. Phys. Chem. A*, vol. 118, p. 8572–8582, Sep 2014.

[143] F. Lindemann, S. Arrhenius, I. Langmuir, N. Dhar, J. Perrin, and W. M. Lewis, "Discussion on the radiation theory of chemical action," *Trans. Faraday Soc.*, vol. 17, pp. 598–606, 1922.

[144] A. Castleman Jr, K. Weil, S. Sigsworth, R. Leuchtner, and R. Keesee, "Considerations of the rates and lifetimes of intermediate complexes for the association of various ligands to metal ions: Ag^+ and Cu^+," *J. Chem. Phys.*, vol. 86, no. 7, pp. 3829–3835, 1987.

[145] G. Gioumousis and D. Stevenson, "Reactions of gaseous molecule ions with gaseous molecules. v. theory," *J. Chem. Phys.*, vol. 29, no. 2, pp. 294–299, 1958.

[146] P. Langevin, "A fundamental formula of kinetic theory," *Ann. Chim. Phys*, vol. 5, pp. 245–288, 1905.

[147] G. D. Billing and K. V. Mikkelsen, *Introduction to Molecular Dynamics and Chemical Kenetics.* Wiley, 1996.

[148] S. M. Lang, *Reactions of cationic gold clusters in a radio frequency ion trap under multi-collision conditions: coadsorption phenomena and activation of molecular oxygen and methane.* PhD thesis, Universität Ulm, 2009.

[149] M. Engeser, T. Weiske, D. Schröder, and H. Schwarz, "Oxidative degradation of small cationic vanadium clusters by molecular oxygen: On the way from V_n^+ (n= 2-5) to VO_m^+(m= 1, 2)," *J. Phys. Chem. A*, vol. 107, no. 16, pp. 2855–2859, 2003.

[150] Å. M. L. Øiestad and E. Uggerud, "Gas phase reactivity of small cationic cobalt clusters towards methanol," *Chem. Phys.*, vol. 262, no. 1, pp. 169–177, 2000.

[151] R. Burgert, S. T. Stokes, K. H. Bowen, and H. Schnöckel, "Primary reaction steps of Al_{13}-clusters in an HCl atmosphere: Snapshots of the dissolution of a base metal," *J. Am. Chem. Soc.*, vol. 128, no. 24, pp. 7904–7908, 2006.

[152] M. Zhou and L. Andrews, "Reactions of laser-ablated niobium and tantalum atoms with oxygen molecules: Infrared spectra of niobium and tantalum oxide molecules, anions, and cations," *J. Phys. Chem. A*, vol. 102, no. 43, pp. 8251–8260, 1998.

[153] X. Wang, Z. Gu, and Q. Qin, "A mass spectrometric study on the formation of ionic Ta-containing oxides from laser ablation of Ta and Ta_2O_5 in O_2 ambient," *Int. J. Mass Spectrom.*, vol. 188, no. 3, pp. 205–212, 1999.

[154] A. Fielicke, G. Meijer, and G. Von Helden, "Infrared multiple photon dissociation spectroscopy of transition metal oxide cluster cations," *EPJ D*, vol. 24, no. 1, pp. 69–72, 2003.

[155] A. Fielicke, G. Meijer, and G. von Helden, "Infrared spectroscopy of niobium oxide cluster cations in a molecular beam: Identifying the cluster structures," *J. Am. Chem. Soc.*, vol. 125, no. 12, pp. 3659–3667, 2003.

[156] Y.-X. Zhao, X.-L. Ding, Y.-P. Ma, Z.-C. Wang, and S.-G. He, "Transition metal oxide clusters with character of oxygen-centered radical: a DFT study," *Theor. Chem. Acc.*, vol. 127, no. 5-6, pp. 449–465, 2010.

[157] H.-J. Zhai, X.-H. Zhang, W.-J. Chen, X. Huang, and L.-S. Wang, “Stoichiometric and oxygen-rich $M2O_n^-$ and $M2O_n$ (M= Nb, Ta; n= 5- 7) clusters: Molecular models for oxygen radicals, diradicals, and superoxides,” *J. Am. Chem. Soc.*, vol. 133, no. 9, pp. 3085–3094, 2011.

[158] B. Darwent, “Bond dissociation energies in simple molecules,” *NSRDS-NBS, U.S. DEPT. COMMERCE, WASHINGTON, D.C.*, vol. 31, pp. 1 – 48, 1970.

[159] A. Fielicke and K. Rademann, “Stability and reactivity patterns of medium-sized vanadium oxide cluster cations $V_xO_y^+$ ($4 \leqslant$ x $\geqslant 14$),” *Phys. Chem. Chem. Phys.*, vol. 4, no. 12, pp. 2621–2628, 2002.

[160] P. Liu and J. A. Rodriguez, “Water-gas-shift reaction on metal nanoparticles and surfaces,” *J. Chem. Phys.*, vol. 126, no. 16, p. 164705, 2007.

[161] A. M. Molenbroek, J. K. Nørskov, and B. S. Clausen, “Structure and reactivity of ni-au nanoparticle catalysts,” *J. Phys. Chem. B*, vol. 105, no. 23, pp. 5450–5458, 2001.

Acknowledgments

Many people contributed significantly to this project. In particular, I have to thank:

Prof. Dr. Heiz for giving me the opportunity to work at his group. Furthermore, I want to express my gratitude for his support and his confidence in me and my work during the last years.
Dr. Martin Tschurl for sharing his meandering expertise from the basic design of the experiment to data analysis. I further deeply respect his delight for the (scientific) discussion and his ability to ask the right question at the right time. Moreover, I am very grateful his introduction to the 'Austrian way of life'.
Dr. Kathrin Lange and Dr. Bradley Visser for laying the foundation of my project, for supervising my early steps in cluster production, for the great atmosphere in the lab despite all the problems we had to overcome. Most important I have to thank for your honest friendship during all the years.
Jan Eckhard, for his support and endless hours in the lab improving the experimental setup. Without his help none of the measurements would have been possible.
Dr. Nadja Heine and Prof. Dr. Knut Asmis for sharing their knowledge about ion traps with me. Also I have to thank Dr. Richard Knochenmuss for the help with the time-of-flight mass spectrometer.
Max Wiedemann, Richard Schröter, Stefan Müller and the electronics workshop for all the work and passion they put into the electronics control unit of the ring electrode ion trap. I am also grateful for the assistance of the mechanical workshop during the construction of the experimental setup.
Finally, I deeply acknowledge the backing by my parents Anneliese and Franz, my brother Tobias, my aunt Maria and my uncle Fritz. Your help, trust and encouragement enabled so much.